frontiers | Research Topics

Radiomics in gastric cancer,
2nd Edition

Edited by
Bo Zhang and Damiano Caruso

Published in
Frontiers in Oncology

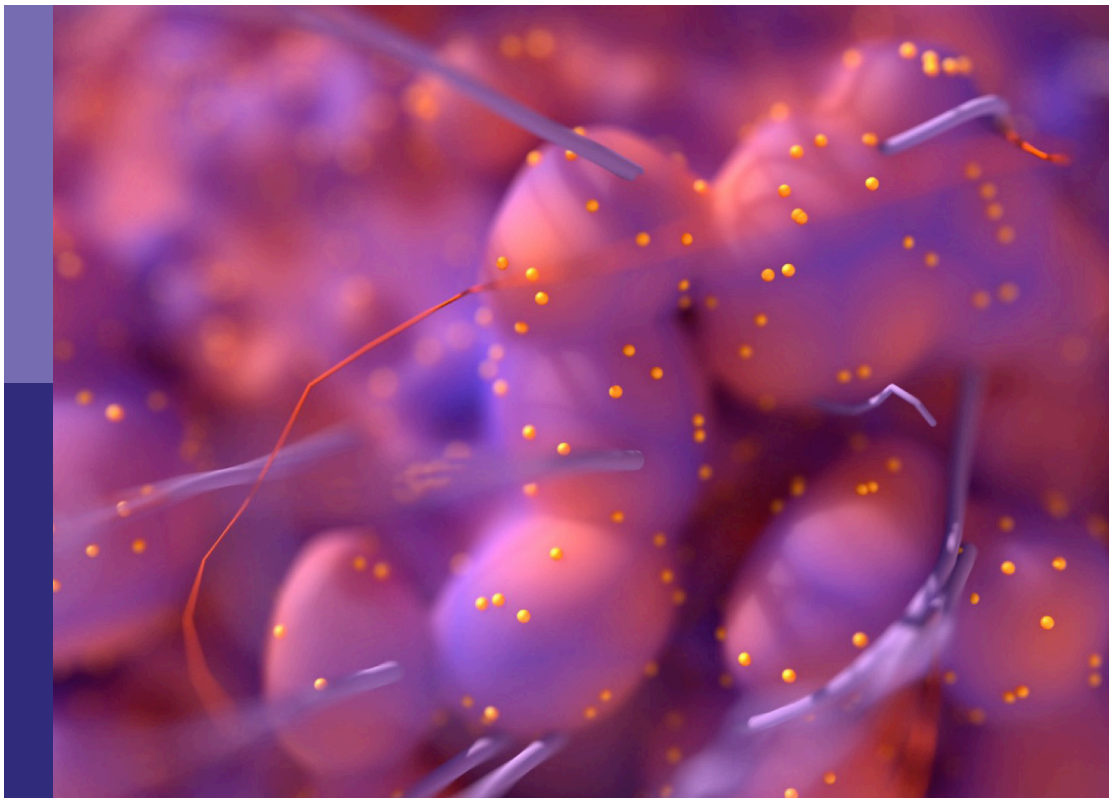

ISSN 1664-8714
ISBN 978-2-8325-4253-8
DOI 10.3389/978-2-8325-4253-8

About Frontiers

Frontiers is more than just an open access publisher of scholarly articles: it is a pioneering approach to the world of academia, radically improving the way scholarly research is managed. The grand vision of Frontiers is a world where all people have an equal opportunity to seek, share and generate knowledge. Frontiers provides immediate and permanent online open access to all its publications, but this alone is not enough to realize our grand goals.

Frontiers journal series

The Frontiers journal series is a multi-tier and interdisciplinary set of open-access, online journals, promising a paradigm shift from the current review, selection and dissemination processes in academic publishing. All Frontiers journals are driven by researchers for researchers; therefore, they constitute a service to the scholarly community. At the same time, the *Frontiers journal series* operates on a revolutionary invention, the tiered publishing system, initially addressing specific communities of scholars, and gradually climbing up to broader public understanding, thus serving the interests of the lay society, too.

Dedication to quality

Each Frontiers article is a landmark of the highest quality, thanks to genuinely collaborative interactions between authors and review editors, who include some of the world's best academicians. Research must be certified by peers before entering a stream of knowledge that may eventually reach the public - and shape society; therefore, Frontiers only applies the most rigorous and unbiased reviews. Frontiers revolutionizes research publishing by freely delivering the most outstanding research, evaluated with no bias from both the academic and social point of view. By applying the most advanced information technologies, Frontiers is catapulting scholarly publishing into a new generation.

What are Frontiers Research Topics?

Frontiers Research Topics are very popular trademarks of the *Frontiers journals series*: they are collections of at least ten articles, all centered on a particular subject. With their unique mix of varied contributions from Original Research to Review Articles, Frontiers Research Topics unify the most influential researchers, the latest key findings and historical advances in a hot research area.

Find out more on how to host your own Frontiers Research Topic or contribute to one as an author by contacting the Frontiers editorial office: frontiersin.org/about/contact

Radiomics in gastric cancer, 2nd Edition

Topic editors
Bo Zhang — Sichuan University, China
Damiano Caruso — Sapienza University of Rome, Italy

Citation
Zhang, B., Caruso, D., eds. (2023). *Radiomics in gastric cancer, 2nd Edition*. Lausanne: Frontiers Media SA. doi: 10.3389/978-2-8325-4253-8

Publisher's note: This is a 2nd edition due to several articles removed from this Research Topic.

Table of contents

frontiers in Oncology

ORIGINAL RESEARCH
published: 15 September 2021
doi: 10.3389/fonc.2021.740732

Predicting Response to Systemic Chemotherapy for Advanced Gastric Cancer Using Pre-Treatment Dual-Energy CT Radiomics: A Pilot Study

Yi-yang Liu[1,2†], Huan Zhang[3†], Lan Wang[3†], Shu-shen Lin[4], Hao Lu[1,2], He-jun Liang[5], Pan Liang[1,2], Jun Li[1], Pei-jie Lv[1] and Jian-bo Gao[1,2]*

[1] Department of Radiology, The First Affiliated Hospital of Zhengzhou University, Zhengzhou, China, [2] Henan Key Laboratory of Imaging Diagnosis and Treatment for Digestive System Tumor, Zhengzhou, China, [3] Department of Radiology, Ruijin Hospital, Shanghai Jiao Tong University School of Medicine, Shanghai, China, [4] Department of DI CT Collaboration, Siemens Healthineers Ltd, Shanghai, China, [5] Department of Oncology, The First Affiliated Hospital of Zhengzhou University, Zhengzhou, China

OPEN ACCESS

Edited by:
Hironaga Satake,
Kansai Medical University Hospital, Japan

Reviewed by:
Tatsuki Ikoma,
Osaka Red Cross Hospital, Japan
Shogen Boku,
Kansai Medical University Hospital, Japan
Toshihiko Matsumoto,
Kobe City Medical Center General Hospital, Japan
Yumiko Kono,
Kansai Medical University, Japan

***Correspondence:**
Jian-bo Gao
fccyisunshine@gs.zzu.edu.cn

[†]These authors have contributed equally to this work

Specialty section:
This article was submitted to Gastrointestinal Cancers: Gastric & Esophageal Cancers, a section of the journal Frontiers in Oncology

Received: 13 July 2021
Accepted: 24 August 2021
Published: 15 September 2021

Citation:
Liu Y-y, Zhang H, Wang L, Lin S-s, Lu H, Liang H-j, Liang P, Li J, Lv P-j and Gao J-b (2021) Predicting Response to Systemic Chemotherapy for Advanced Gastric Cancer Using Pre-Treatment Dual-Energy CT Radiomics: A Pilot Study. Front. Oncol. 11:740732. doi: 10.3389/fonc.2021.740732

Objective: To build and assess a pre-treatment dual-energy CT-based clinical-radiomics nomogram for the individualized prediction of clinical response to systemic chemotherapy in advanced gastric cancer (AGC).

Methods: A total of 69 pathologically confirmed AGC patients who underwent dual-energy CT before systemic chemotherapy were enrolled from two centers in this retrospective study. Treatment response was determined with follow-up CT according to the RECIST standard. Quantitative radiomics metrics of the primary lesion were extracted from three sets of monochromatic images (40, 70, and 100 keV) at venous phase. Univariate analysis and least absolute shrinkage and selection operator (LASSO) were used to select the most relevant radiomics features. Multivariable logistic regression was performed to establish a clinical model, three monochromatic radiomics models, and a combined multi-energy model. ROC analysis and DeLong test were used to evaluate and compare the predictive performance among models. A clinical-radiomics nomogram was developed; moreover, its discrimination, calibration, and clinical usefulness were assessed.

Result: Among the included patients, 24 responded to the systemic chemotherapy. Clinical stage and the iodine concentration (IC) of the tumor were significant clinical predictors of chemotherapy response (all $p < 0.05$). The multi-energy radiomics model showed a higher predictive capability (AUC = 0.914) than two monochromatic radiomics models and the clinical model (AUC: 40 keV = 0.747, 70 keV = 0.793, clinical = 0.775); however, the predictive accuracy of the 100-keV model (AUC: 0.881) was not statistically different ($p = 0.221$). The clinical-radiomics nomogram integrating the multi-energy radiomics signature with IC value and clinical stage showed good calibration and discrimination with an AUC of 0.934. Decision curve analysis proved the clinical usefulness of the nomogram and multi-energy radiomics model.

Conclusion: The pre-treatment DECT-based clinical-radiomics nomogram showed good performance in predicting clinical response to systemic chemotherapy in AGC, which may contribute to clinical decision-making and improving patient survival.

Keywords: dual-energy CT, radiomics, response prediction, systemic chemotherapy, gastric cancer

INTRODUCTION

Gastric cancer (GC) remains one of the most common malignant tumors in the world, and its morbidity and mortality rank fifth and third, respectively. There were more than a million new cases and an approximated 784,000 deaths worldwide in 2018 (1); moreover, most GC cases are diagnosed at an advanced stage (2). It is therefore essential to select an effective treatment regimen for advanced gastric cancer (AGC) to maximize the overall therapeutic benefits. Chemotherapy can improve survival and quality of life for patients present with unresectable, locally advanced, or metastatic GC (3). Furthermore, the overall survival of AGC patients who are treated with systemic chemotherapy was 8 months longer than with optimal supportive care alone (4–8). However, tumor response rate of most treatment regimens is less than 40% and chemotherapy drugs can cause serious side effects in some patients (9, 10). Hence, pre-treatment prediction of tumor response to systemic chemotherapy may translate into more precise patient selection and individualized medicine, which are of great clinical significance.

Dual-energy CT (DECT) is a milestone imaging tool that generates a rich amount of DECT quantitative information. The virtual monochromatic images (VMI) derived from DECT have been used in the diagnosis and prediction of tumors, including classification of parotid neoplasms, the evaluation and characterization of cervical lymphadenopathy, prediction of lymph node metastasis in GC, and classification of clear cell renal cell carcinoma (11–15). In terms of predicting the treatment efficacy, Tang et al. demonstrated that iodine concentration (IC) on DECT could evaluate efficacy response of GC to neoadjuvant chemotherapy (16). However, to our knowledge, the application and potential advantages of multi-energy virtual monochromatic image datasets in predicting therapeutic response of GC have not been explored. Theoretically, there is a rich amount of quantitative information in the variation of energy-dependent attenuation in different tissues. Given the dynamic and heterogeneous nature of tumor (17, 18), performing radiomics analysis on monochromatic images may improve the predictive capabilities (11).

Radiomics can noninvasively analyze tumor biology, distinguish the subtle differences that human eyes cannot discern, quantify tumor heterogeneity, and monitor tumor development and response to treatment (19–23). Through extensive extraction of quantitative features, radiomics can delineate tumor heterogeneity metrics, which may reflect pathophysiological characteristics associated with treatment response (23–25). In fact, pre-treatment radiomics with other CT techniques has been proven to non-invasively predict treatment responses of GC (26–29).

Therefore, we aimed to establish and assess a clinical-radiomics nomogram from pre-treatment DECT scans to predict clinical response to systemic chemotherapy in patients with AGC, and to verify whether radiomics performed on multi-energy VMI datasets is more helpful in predicting response.

MATERIALS AND METHODS

Patients

This multi-center, retrospective study was approved by the institutional review board, and the requirement for informed consent was waived due to the retrospective study design. A total of 69 consecutive patients from two independent institutions (49 from the Zhengzhou University First Affiliated Hospital between March 2014 and November 2019 and 20 from Shanghai Jiao Tong University Ruijin Hospital between November 2017 and February 2019) were collected. The inclusion criteria were as follows: (1) histologically confirmed primary gastric adenocarcinoma; (2) no prior history of radiotherapy, chemotherapy, or other treatments that might affect the blood supply to the tumor; (3) no serious heart and renal insufficiency and other important viscera lesions; (4) received baseline contrast-enhanced DECT examinations within 1 week before chemotherapy; (5) treated with systemic chemotherapy due to metastatic, unresectable, and recurrent GC or tumors surrounding major vessels on CT examination (cT4a~bNxM0~1); (6) ECOG PS 0–2. The exclusion criteria were as follows: (1) patients with co-malignancy; (2) incomplete clinical data at baseline; (3) motion artifacts on CT; (4) lesions with cystic changes or cavitation; and (5) intolerance to chemotherapy. Baseline clinicopathological data, including age, sex, and clinical stage, were obtained from retrospective electronic records.

Systemic Chemotherapy Regimen and Treatment Response Evaluation

In our study, enrolled patients were mainly treated with capecitabine plus oxaliplatin (XELOX) regimen or S-1 plus oxaliplatin (SOX) regimen.

In detail, patients were given capecitabine at a dose of 1,000 mg/m^2 (or S-1: 60 mg/m^2) orally twice daily from day 1 to day 14. Furthermore, oxaliplatin (130 mg/m^2) was given intravenously for 2 h on day 1. Cycles were repeated every 21 days, and the toxicity of chemotherapy was evaluated after each cycle. At least six cycles of treatment were given unless there was disease exacerbation, unacceptable toxicity, or death occurred.

Evaluation of Treatment Response

Post-treatment CT images were obtained within 3 weeks after completion of chemotherapy. The treatment response was assessed by the change of the sum of the maximum diameters

for all target lesions in the pre- and post-chemotherapy CT images.

The short-term therapeutic response was evaluated with the standard of Response Evaluation Criteria in Solid Tumors (RECIST v. 1.1) (30). Based on current study purpose, we classified patients with complete response (CR, complete disappearance of all target lesions and no new lesions) or partial response (PR, a reduction ≥30% in the sum of the diameters of target lesions) as responders, while others with stable disease (SD, neither partial response nor progressive disease) or progressive disease (PD, a ≥20% size increase or new disease) were classified as non-responders (**Figures 1** and **2**).

CT Image Acquisition

All patients fasted for 8 to 12 h before examination and took 800–1000 ml of warm water before the CT scan, where the patients were placed in a supine position with head first and breath-hold.

CT scans were performed using multi-vendor Dual-Energy CT (Discovery CT750 HD scanner, GE Healthcare, Milwaukee, WI, USA; SOMATOM Force scanner, Siemens Healthineers, Forchheim, Germany). The patients underwent contrast-enhanced DECT scans, including the arterial phase (AP) and venous phase (VP). After unenhanced CT was performed, the main contrast agent (Ultravist 370, Bayer Schering Pharma, Thüringen. Germany) was infused intravenously through the antecubital vein at a rate of 3.0 ml/s (1.5 ml/kg) using a pump injector. AP and VP contrast-enhanced CT images were achieved after a post-injection delay of 30 and 70 s, respectively. The scanning parameters were summarized as follows (1) Discovery CT750 HD: using fast tube voltage switching between 80 and 140 kVp, tube current: 375 mA, pitch: 1.375:1, rotation time: 0.6 s, detector width: 40 mm, collimation: 128*0.6 mm, FOV: 400 × 400 mm; reconstruction algorithm: STAND; reconstructed section thickness:1.25 mm slice thickness: 5 mm. (2) SOMATOM Force: tube voltage: 100/Sn150 kVp; effective tube current-time product: 200/125 mAs; FOV: 374 × 374 mm; rotation time: 0.5 s; pitch: 0.6; reconstructed section thickness: 1.25 mm slice thickness: 5 mm; kernel: Qr40; collimation: 128*0.6 mm.

Image Analysis

The CT images were transferred to dedicated workstations with dual-energy software (Syngo.via, Version VB10, Siemens Healthineers, Forchheim, Germany; ADW 4.7, GE Healthcare, Milwaukee, WI, USA).

A 15-year experienced gastrointestinal radiologist interpreted the dual-energy images with the knowledge that all patients had GC confirmed by endoscopic biopsy. Clinical lymph node staging (cN) and distant metastasis staging (cM) were evaluated according to the 8th edition of AJCC guidelines (31), and the distant metastatic sites were recorded. The maximal thickness (the largest short diameter perpendicular to the longest axis on the maximal cross-section) of the primary tumor was

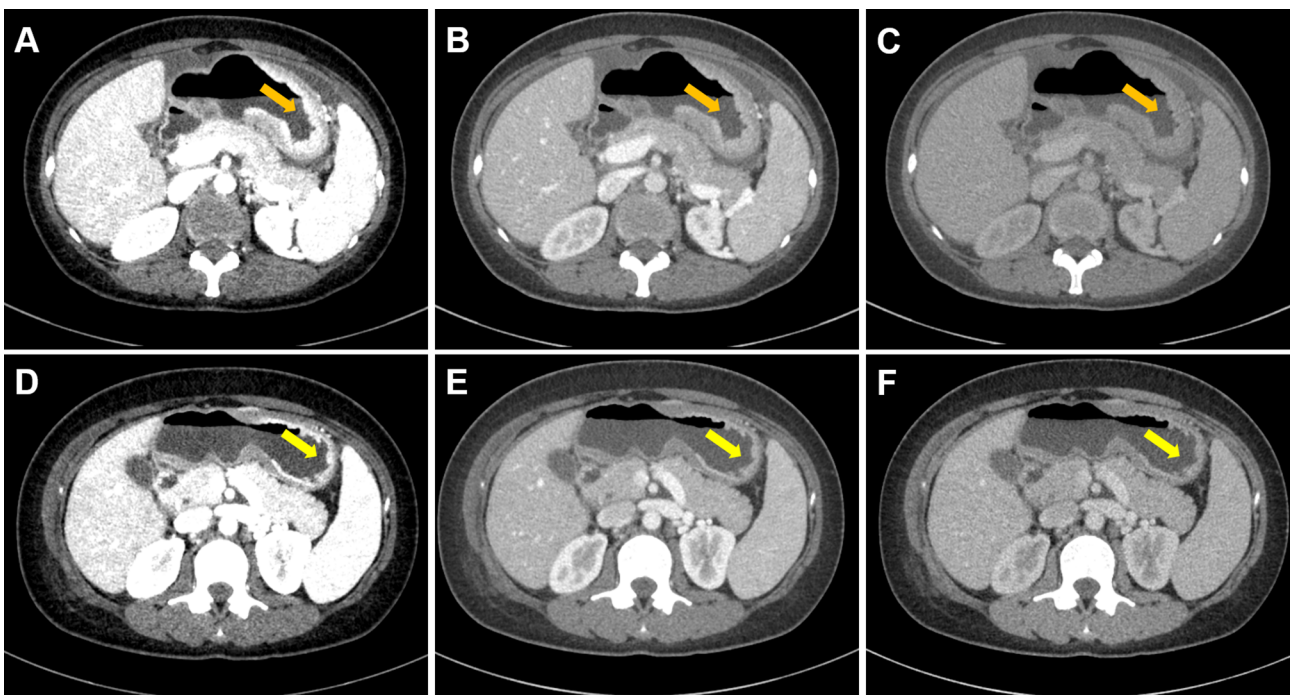

FIGURE 1 | Case 1. Portal phase DECT images of a 34-year-old female with GC patient who responded to chemotherapy. **(A–C)** Diffuse thickened gastric wall was seen at the gastric body (arrow). **(D–F)** Slightly thickened gastric wall was seen at the gastric body, and the lesion was significantly regressed (arrow). **(A–C)** were monochromatic images of 40, 70, and 100 keV before chemotherapy, respectively. **(D–F)** were monochromatic images of 40, 70, and 100 keV after chemotherapy, respectively.

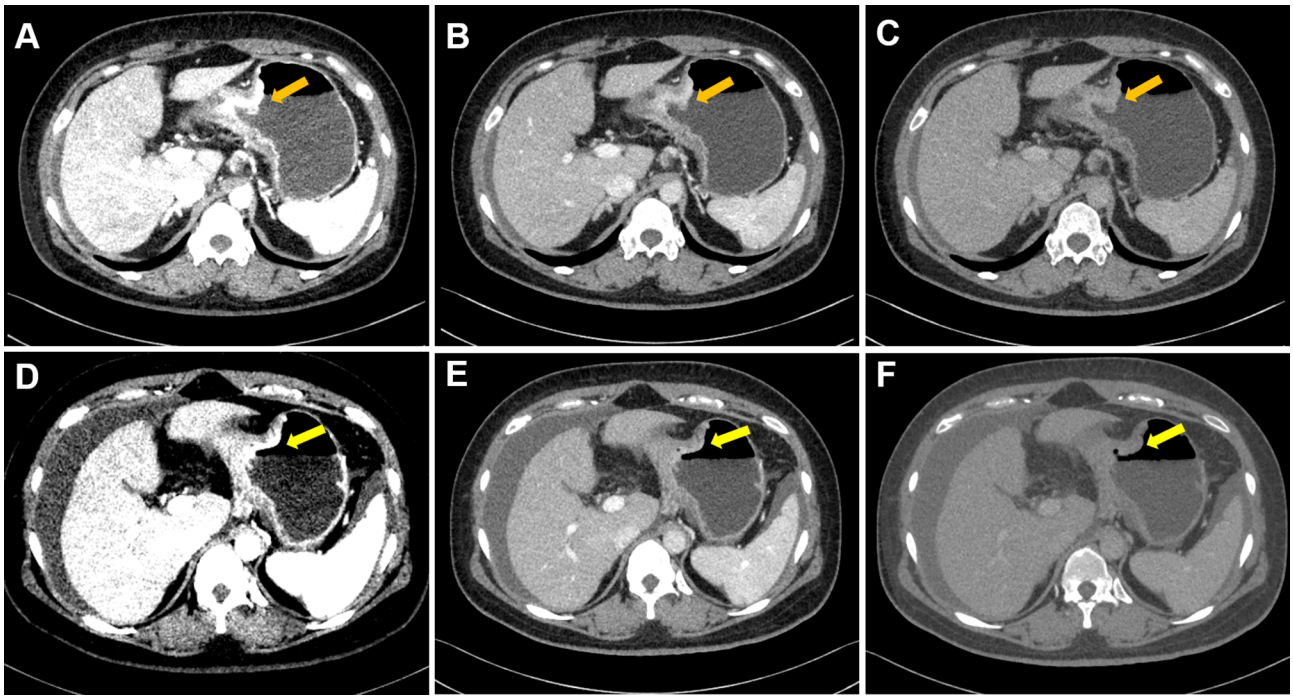

FIGURE 2 | Case 2. Portal phase DECT images of a 40-year-old female patient with GC who did not respond to chemotherapy. **(A–C)** An irregular wall-thickening lesion at the gastric body was present (arrow). **(D–F)** There was no obvious change (slightly regression) in the lesions of gastric body (arrow). **(A–C)** were monochromatic images of 40, 70, and 100 keV before chemotherapy, respectively; **(D–F)** were monochromatic images of 40, 70, and 100 keV after chemotherapy, respectively. Note: After completion of chemotherapy, the patient was diagnosed with aggravated peritoneal metastasis.

measured. The Borrmann classification of the tumor was also assessed (32). A free-hand, VP-based individualized region of interest (ROI) was manually delineated on iodine-based material decomposition images in the largest cross-sectional area by the reader, and then the ICs (mean value, units of 100 μg/ml) of the lesion in the ROI was recorded. Meanwhile, circular ROIs were carefully placed at the same slice to avoid calcified plaques and subsequently obtain the aortic ICs. Finally, the iodine ratio of the lesion to aorta was taken as normalized iodine concentration (NIC = IC lesion/IC aorta).

Tumor Segmentation and Feature Extraction

We conducted lesion segmentation and radiomics feature extraction with a prototypical software (Syngo Frontier, Radiomics 1.0.9a, Siemens Healthineers, Germany). Venous phase images were previously reported as the best phase for GC visualization (14, 27, 33) and therefore were used for tumor segmentation. In order to seize the energy-dependent changes in tissue attenuation, we selected monochromatic images of 40, 70, and 100 keV as typical dual-energy datasets for feature extraction. The volumes of interest (VOI), referred to whole tumor regions in three dimensions on venous phase contrast-enhanced DECT images, was delineated by a radiologist with 7 years of experience and reviewed by a radiologist with 10 years of experience to minimize possible bias (**Supplemental Appendix 1; Figure S1**). The software provides a variety of options to customize image pre-processing before radiomic feature extraction, including wavelet filtering, Laplacian of Gaussian filtering, and non-linear intensity transforms including logarithm, exponential, square, and square root operations. The extracted features were reproducible and matched the benchmarks of image biomarker standardization initiative (IBSI) (34).

Finally, 1691 radiomics features were extracted from each patient in each single-energy image set, including 17 shape features, 324 first-order features, and 1,350 texture features **Supplemental Appendix 2; Table A1**.

Feature Selection and Radiomics Model Establishment

To prevent overfitting or selection bias in our radiomics model, univariate logistic regression analysis ($p < 0.05$) and LASSO regression were used to screen out the most relevant informative radiomic features of chemotherapy response. Tenfold cross-validation was performed to determine the optimal value of regularization parameter λ at minimum MSE. Based on the selected features, the radiomics model was established by multivariate logistic regression algorithm. Three single-energy (40-keV, 70-keV, and 100-keV) radiomics models and a multi-energy (combined three single-energy features) radiomics model were established. The process of LASSO is shown in **Supplemental Appendix 3; Figure S2**.

Clinical Model and Nomogram Establishment

Univariate and multivariate logistic regression analysis were used to determine the independent clinical predictors related to chemotherapy response.

The candidate factors of univariate logistic regression analysis included age, gender, clinical stage, cN stage, cM stage, distant metastatic sites, location, Borrmann classification, thickness, and IC and NIC value. Odds ratio and 95% confidence interval (CI) were calculated. The significant variables (p-value < 0.05) in the univariable analysis were considered in the multivariate logistic regression analysis. Then, the independent clinical predictive factors were determined and the clinical model was established. In addition, a combination model (ComModel) was established by combining the selected clinical predictor with multi-energy radiomics model to explore the added value of the additional dual-energy information. Meanwhile, the ComModel was visualized as a nomogram to predict individualized probability of response.

Evaluation and Comparison of Model Performance

Evaluation of the model contained discrimination, calibration, and clinical usefulness. The receiver operating characteristic (ROC) curve analysis was used to evaluate the discrimination performance of each model, while the DeLong test was used to compare the differences in area under the curve (AUC) among different models. Calibration curves were carried out to describe calibration performance according to agreement between predicted and actual probability of response. Decision curve analysis (DCA) was employed to estimate the clinical usefulness of the model based on the net benefit at different threshold probabilities. The radiomics flowchart of our study is shown in **Figure 3**.

Statistical Analysis

Feature selection, model construction, and performance evaluation were performed on R software package (version 3.6.3). Other statistical analyses were conducted with SPSS25.0 software (IBM, USA). A two-tailed p-value<0.05 was considered statistically significant.

Normality of distribution of continuous variables was tested using a Kolmogorov–Smirnov test. The differences in continuous variables were assessed by using analysis of variance (ANOVA), and categoric variables were compared using the χ^2 test.

RESULTS

Clinical Characteristics

The general demographic characteristics, clinicopathological characteristics, and dual-energy parameters of the patients are shown in **Supplemental Appendix 4; Table A2**. A total of 69 (median age 56 years, range 23–84 years) patients with AGC were analyzed in this study. The number of AGC patients with stage IV disease was 47 (68.1%). There were 10 patients (14.5%) presented with diffuse lesions (lesion location ≥2). Fifty-eight patients (84.1%) demonstrated evidence of lymph node involvement. Distant metastases were found in 40 patients (58.0) and 14 of them (20.3%) presented with liver metastasis.

According to the results of response assessment, patients were divided into responder (n = 24) and non-responder (n = 45) groups. Baseline characteristics of the two groups are summarized in **Table 1**. Clinical Stage, Borrmann classification, and IC were found to be significantly different between groups. Furthermore, univariate and multivariate logistic regression analyses demonstrated that clinical stage and IC value were independent clinical predictors of response to chemotherapy for AGC (**Table 2**).

Radiomics Feature Selection

Based on LASSO regression, we obtained 8, 4, 6, and 11 most significant radiomics features with non-zero coefficients as the predictive radiomics features from the 40-keV, 70-keV, 100-keV, and multi-energy groups, respectively. The distribution of the selected radiomics features of the corresponding model

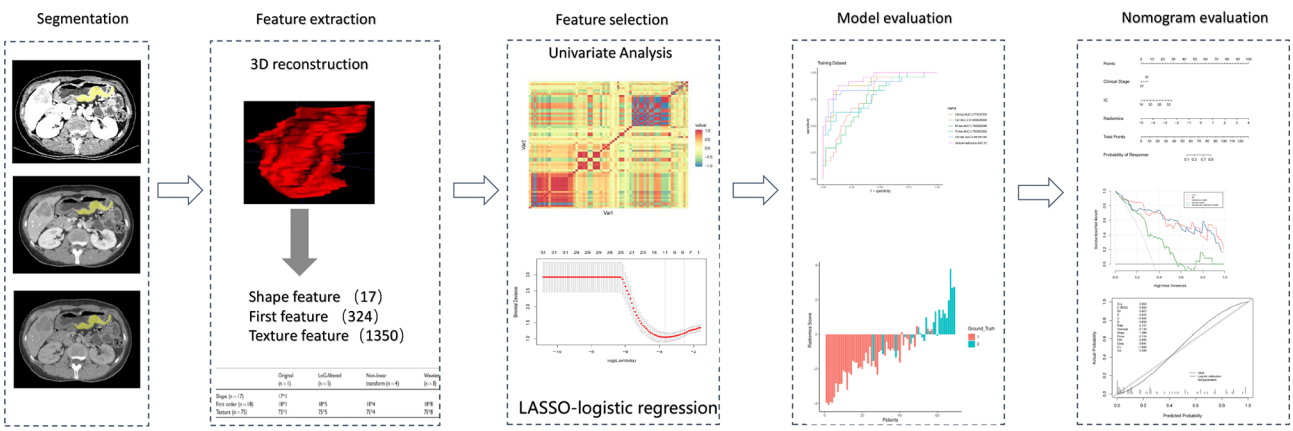

FIGURE 3 | Radiomics workflow of the present study. The radiomics procedure consists mainly of five steps: volume of interest segmentation, feature extraction, feature selection, model evaluation, and nomogram evaluation.

TABLE 1 | Baseline characteristics of responder and non-responder groups.

Characteristics	Responder (*n* = 24)	Non-responder (*n* = 45)	*p*
Age (years)	57.25 ± 12.44	53.22 ± 14.10	0.250
Sex			0.352
Female	9	12	
Male	15	33	
ECOG			0.136
PS 0	11	29	
PS 1–2	13	16	
Clinical Stage			0.018*
III	12	10	
IV	12	35	
cN stage			0.768
N0	5	6	
N1	10	17	
N2	5	11	
N3	4	11	
Metastatic sites			0.597
Absent	12	17	
Liver	4	10	
Lung	0	2	
Other[a]	8	16	
Location			0.879
Upper	11	19	
Middle	3	9	
Lower	6	11	
Diffuse	4	6	
Borrmann type			<0.001*
I–II	2	8	
III	20	15	
IV	2	22	
Thickness (cm)	2.165 ± 0.723	2.520 ± 0.855	0.093
IC (100 μg/ml)	24.857 ± 3.153	21.780 ± 3.379	0.001*
NIC	0.078 ± 0.044	0.127 ± 0.067	0.257

**p-value < 0.05. Data (%) are the proportion of sample size or mean value ± SD.*
[a]peritoneum, distant lymph node, adrenal gland, ovary; N, lymph node; IC, iodine concentration; NIC, normalized iodine concentration.

coefficients is shown in **Supplemental Appendix 5**, **Tables A3** and **A4**.

Evaluation and Comparison of Model Performance

Radiomics model: The 100 keV radiomics model had the better predictive value among the three monochromatic radiomics models, with an AUC of 0.881 (95% CI 0.791–0.971). The AUC was 0.747 (95% CI: 0.628–0.866) for the 40-keV radiomics model and 0.793 (95% CI 0.678–0.908) for the 70-keV radiomics model. The AUC of the multi-energy radiomics model was 0.914 (95% CI 0.846–0.982) (**Figure 4A**).

Clinical model: Clinical stage and IC were included in the model. The AUC of the clinical model was 0.774 (95% CI 0.628–0.866).

Combined model: A combined clinical-radiomics model (ComModel) was established incorporating multi-energy radiomics features, clinical stage, and IC value while presented as a nomogram (**Figure 4B**). The AUC of ComModel was 0.934 (0.877–0.991).

The AUC of the multi-energy radiomics model predicting response probability was superior to two monochromatic radiomics models and the clinical model. The ComModel achieved best discrimination among all models with an AUC of 0.934. Besides, there was no significant difference between ComModel, the 100-keV model, and the multi-energy model (p = 0.138 between the multi-energy model and ComModel, p = 0.073 between ComModel and the 100-keV model, p = 0.221 between the 100-keV model and the multi-energy model). ROC curves and detailed performances of the six models are illustrated in **Figure 4C** and **Table 3**. A comparison of discrimination of these models is demonstrated in **Table 4**.

Evaluation of Clinical-Radiomics Nomogram Performance

The calibration curves of the nomogram (**Figure 5A**) showed a good fit between predictive probability of response and actual response rate. Non-significant statistics of the accompanied Hosmer–Lemeshow test (p = 0.280) implied that the nomogram was adequately calibrated without departure from the ideal fit. The decision curve analysis (**Figure 5B**) demonstrated good performance of the multi-energy radiomics model and the nomogram in terms of clinical decision-making, which added more benefits than either a treat-all or treat-none scheme. In addition, the analysis showed that the nomogram and multi-energy radiomics model had a similar clinical application value, and their prediction performance was better than that of the clinical model.

TABLE 2 | Clinical predictors for response to chemotherapy in patients with AGC.

Characteristic	Univariable analysis	*p*-value	Multivariable analysis	*p*-value
	OR (95% CI)		OR (95% CI)	
Age (years)	1.023 (0.984–1.062)	0.249		
Sex		0.354		
Male	Reference			
Female	1.650 (0.573–4.753)			
ECOG		0.139		
PS 0	Reference			
PS 1–2	2.142 (0.781–5.873)			
Clinical stage		0.021*		0.029*
III	Reference		Reference	
IV	0.286 (0.098–0.829)		0.251 (0.072–0.869)	
cN stage				
N0	Reference	–		
N1	0.706 (0.170–2.923)	0.631		
N2	0.545 (0.111–2.673)	0.455		
N3	0.436 (0.084–2.269)	0.324		
cM stage		0.329		
M0	Reference			
M1	0.607 (0.223–1.653)			
Location				
Upper	Reference	–		
Middle	0.576 (0.128–2.588)	0.472		
Lower	0.942 (0.272–3.260)	0.925		
Diffuse	1.152 (0.266–4.993)	0.850		
Borrmann type				
I–II	Reference	–		
III	4.500 (0.806–25.122)	0.086		
IV	0.350 (0.041–2.977)	0.336		
Thickness (cm)	0.551 (0.272–1.119)	0.099		
IC (100 μg/ml)	1.334 (1.108–1.605)	0.002*	1.309 (1.067–1.605)	0.010*
NIC	6.950 (0.248–194.682)	0.254	4.373 (0.077–247.896)	0.474

**p-value < 0.05. CI, confidence interval; OR, odds ratio; N, lymph node; M, distant metastasis; IC, iodine concentration; NIC, normalized iodine concentration.*

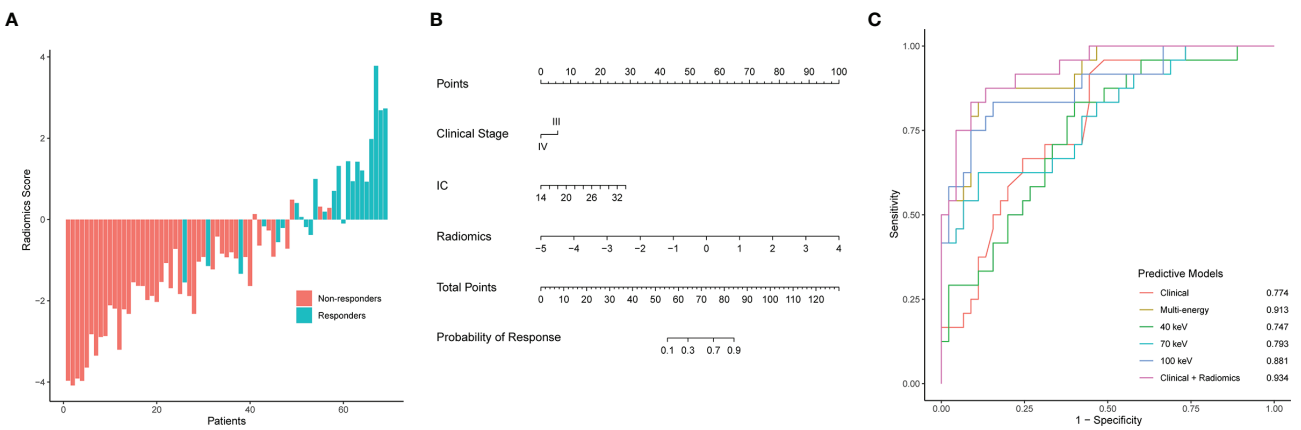

FIGURE 4 | Radiomics score, nomogram developed with the combined model, ROC curve analysis of all models. **(A)** Waterfall plot for distribution of radiomics scores for each patient. **(B)** The developed clinical-radiomics nomogram to predict response to chemotherapy in patients with gastric cancer. **(C)** ROC curves of all models for predicting response to chemotherapy. *AUC, area under the curve; Clinical-radiomics*, nomogram.

DISCUSSION

In this study, we built a DECT-based clinical-radiomics nomogram for systemic chemotherapy response prediction in AGC using datasets from two centers. The constructed nomogram, which combined clinical stages, IC, and DECT-derived radiomics features, demonstrated satisfactory discriminative ability, and can be used to stratify patients who

TABLE 3 | Radiomics, clinical-only, and clinical-radiomics model predictive performance.

Model	AUC (95% CI)	SPE (%)	SEN (%)	ACC (%)	PPV (%)	NPV (%)
40 keV	0.747 (0.628–0.866)	60.0	83.3	68.1	52.6	87.1
70 keV	0.793 (0.678–0.908)	88.9	62.5	79.7	75.0	81.6
100 keV	0.881 (0.791–0.971)	84.4	83.3	84.1	74.1	90.5
Full	0.914 (0.846–0.982)	86.6	87.5	86.9	77.7	92.8
Clinical	0.775 (0.665–0.884)	55.6	91.7	68.1	52.4	92.6
ComModel	0.934 (0.877–0.991)	91.1	83.3	88.4	83.3	91.1

AUC, area under the curve; SPE, specificity; SEN, sensitivity; ACC, accuracy; PPV, positive predictive value; NPV, negative predictive value; Full, multi-energy; ComModel, Clinical-Radiomics; CI, confidence interval.

TABLE 4 | Comparison of discrimination of all models.

Model 5	0.17				
Model 4	<0.01*	0.02*			
Model 3	0.10	0.22	0.11		
Model 2	<0.01*	0.01*	0.81	0.17	
Model 1	<0.01*	<0.01*	0.74	0.02*	0.52
	Model 6	**Model 5**	**Model 4**	**Model 3**	**Model 2**

**p < 0.05. Model (1) corresponds to the model based on selected 40-keV radiomics features, model (2) corresponds to the model based on selected 70-keV radiomics features, model (3) corresponds to the model based on selected 100-keV radiomics features, model (4) corresponds to the clinical model, model (5) corresponds to the model based on selected multi-energy radiomics features, and model (6) corresponds to the model combining multi-energy radiomics features and clinical features.*

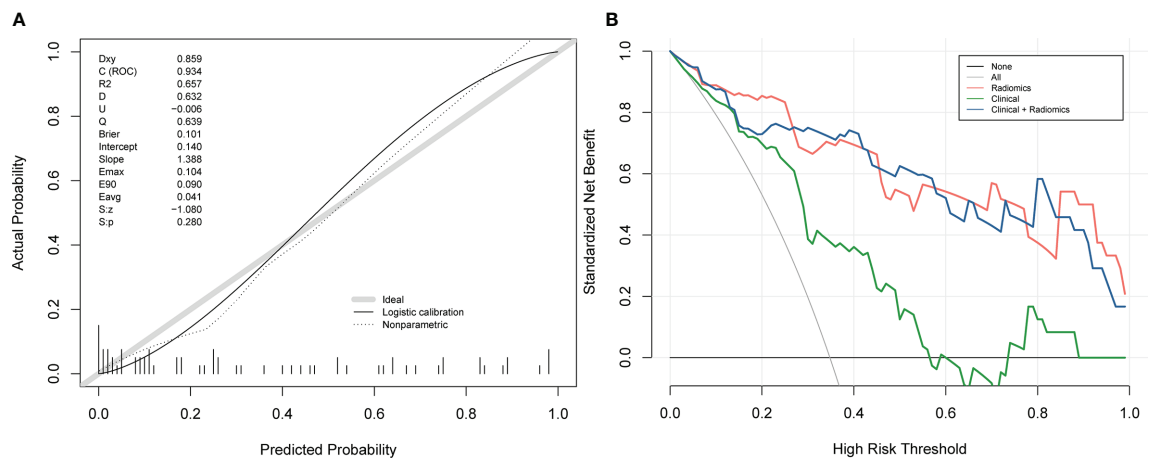

FIGURE 5 | Calibration curves and decision curve analysis of the nomogram. **(A)** Calibration curves of the nomogram. The *x*-axis and the *y*-axis show the nomogram-predicted response probabilities and the actual probabilities, respectively. The calibration curve presents the calibration of the nomogram in terms of the agreement between the predicted response to chemotherapy and the observed probabilities of response to chemotherapy. The diagonal gray line presents a perfect prediction, and the black solid line presents the predictive performance of the nomogram. Better prediction is indicated by a closer fit of the black solid line to the diagonal gray line. **(B)** Decision curve analysis for the combined model, multi-energy radiomics model, and clinical model. The *y*-axis represents the net benefit. The gray line represents the assumption that all patients have a response to chemotherapy; however, the black line is the opposite. The blue line represents the combined model. The red line represents the multi-energy radiomics model. The green line represents the clinical model.

are more likely to benefit from systemic chemotherapy. Furthermore, our study demonstrates that radiomics features extracted from the virtual monochromatic images can reflect heterogeneity of gastric cancer and that radiomics may serve as a promising technique for predicting the response to treatment in patients with AGC.

Existing radiomics models for predicting response to systemic chemotherapy used both pre-treatment and post-treatment CT

images (35). However, the post-treatment nature could narrow its extensive utility in clinical therapy decision-making (36). Thus, pre-treatment images were selected to construct prediction models in the current study. Using a pre-treatment predictive model, clinicians can identify the chemosensitivity of patients, thereby better stratifying patients for more appropriate treatment regimens (36). As a result, the pre-treatment predictive model may broaden its application in the clinical settings and help personalize treatment and improve prognosis of AGC patients.

Dual-energy imaging extends the capabilities of conventional CT offering potentials to improve lesion detection and characterization (33). At present, some scholars have been committed to the combination of dual-energy CT and radiomics or texture analysis (13, 37–42). However, most feature extractions were based on single-energy monochromatic images, 120 kV equivalent mixed images, or iodine images. There were few studies on feature extraction based on multi-energy images, especially in gastric cancer. Li et al. (14) found that the multi-energy image-based radiomics model could better predict lymph node metastasis (LNM) for gastric cancer when compared to the clinical and single-energy model. In terms of monoenergetic selection for radiomics model construction, 70 keV was used as it could resemble a 120-kVp conventional single-energy CT acquisition, while having a higher contrast-to-noise ratio and less image noise (43–46). Meanwhile, according to basic CT physics and algorithms, we also selected 40-keV images as the representative of low-energy dataset (40–70 keV) to reflect the tissue enhancement characteristics and 100-keV images as the representative of high-energy dataset (100–140 keV) to reflect the tissue non-enhanced characteristics. In our comparison of three monoenergetic radiomics models, the 100-keV model achieved a better performance. High-energy monochromatic images have higher image quality and lower background parenchymal noise (47, 48). Thus, we speculate that the radiomics features based on low-noise, high-energy images reflecting the tissue non-enhanced nature are more likely to seize the heterogeneity of tumors. Notably, the 100-keV model did not significantly differ from the multi-energy model or the clinical-radiomics nomogram in terms of response prediction. This finding was consistent with a previous study that the potential benefits of multi-energy images must be evaluated on a case-by-case basis (13). From this, the 100-keV images not only was visually comfortable and extensively useful in clinical routine display (14), but also showed good performance in predicting systemic chemotherapy response of AGC.

DECT-derived IC represents iodine deposition in tissues and is deemed as an alternative measure for tumor vascularity and perfusion (49). Previous studies have explored the application of IC in the field of oncology for diagnosis, the prediction of lymph node metastasis, and the evaluation of therapy response (50–52). Tang et al. revealed that the tumor IC was in good agreement with the pathological regression in evaluating the response of GC to neoadjuvant chemotherapy, and prediction efficacy of IC was superior to that of tumor thickness (16). In the present study, univariate and multivariate analysis results showed that IC was an independent predictor of the response of chemotherapy for GC. Moreover, the IC value of the non-response group was significantly lower than that of the response group, which may indicate that the relatively low blood supply of the tumor before chemotherapy has some difficulties in the targeted organ transportation of chemotherapy drugs, leading to a lower sensitivity of chemotherapy than that of the tumor with relatively rich blood supply before chemotherapy. Although NIC has been proven to be a relatively stable indicators in tumor staging and detection of HER2 status (53, 54), its application and benefits are not entirely clear (55). Previous study revealed that NIC cannot serve as an independent predictive factor for lymph node metastasis in GC (51). Similarly, this study found that NIC was not statistically significant in univariate logistic analysis ($p > 0.05$); however, we still included NIC in the multivariate study and further confirmed it as a non-independent risk factor. Hence, future studies are prompted to discuss and validate the value of NIC in tumor prediction.

Tumor thickness plays an important role in predicting the therapeutic response of GC. Wang et al. revealed that tumor thickness ratio reduction was a good predictor of pathological complete response (pCR) after neoadjuvant chemotherapy (NAC) in patients with GC; however, tumor thickness before NAC was not helpful in predicting pCR (56). We also found that pre-treatment tumor thickness was not correlated with systemic chemotherapy response. Previous studies have suggested that the clinical staging of GC is closely related to the choice of treatment strategy and prognosis. At the same time, we have also demonstrated IC and clinical staging were significantly associated with systemic chemotherapy response, and an improvement of predictive power was observed when IC and clinical staging were added to the radiomics model.

Our study had some limitations. First, this is a pilot study using functional imaging radiomics to predict response to systemic chemotherapy. Although data from two centers were included, the sample size was still limited and lacked a validation group. However, the construction of our radiomics prediction model was based on features screened out using 10-fold cross-validation, ensuring optimal reliability and reproducibility. Furthermore, future collaboration with other dual-energy CT centers is underway to enlarge the sample size. Second, the current study gathered dual-center dual-energy data to increase the statistical power at the expense of increased variability of different manufacturers' scanners; however, we used monochromatic images derived from the fast kilovolt peak-switching and dual-source acquisition paradigms to extract radiomics features to reduce the possible variability. Jacobsen et al. confirmed in a large phantom study that fast kilovolt peak-switching and dual source usually provided the most accurate monochromatic attenuation, and little difference existed in monochromatic error between the two scan protocols used in our study (57). Meanwhile, predictive model developed by current research achieved favorable performance, which further shows the good predictive value of the radiomics features based on different manufacturers' dual-energy CT for chemotherapy response. Future research can attempt to use uniform dual-energy scanners and standardized imaging techniques to establish predictive model.

In conclusion, we developed a pre-treatment dual-energy CT–based radiomics nomogram for predicting clinical response to systemic chemotherapy in patients with AGC. Our preliminary results revealed that integrating multidimensional data including radiomics, clinical factors, and dual-energy parameter could benefit risk stratification, optimize candidate selection for systemic chemotherapy, and, finally, improve quality of life in patients with advanced gastric cancer.

DATA AVAILABILITY STATEMENT

The original contributions presented in the study are included in the article/**Supplementary Material**. Further inquiries can be directed to the corresponding author.

ETHICS STATEMENT

The studies involving human participants were reviewed and approved by the medical ethical committee of Zhengzhou University and Ruijin Hospital. Written informed consent for participation was not required for this study in accordance with the national legislation and the institutional requirements.

AUTHOR CONTRIBUTIONS

Y-yL: manuscript preparation, literature research, and data analysis. HZ: manuscript preparation and literature research. LW: manuscript preparation and data collection. S-sL: data analysis. HL: data collection. H-jL: data analysis assistance. PL and JL: imaging analysis. P-jL: manuscript editing. J-bG: study conception and design, manuscript review, and guarantor of integrity of the entire study. All authors contributed to the article and approved the submitted version.

FUNDING

Funding was provided by the National Natural Science Foundation of China (No.81971615) and the National Key Research and Develop Program of China (No. 2017YFC0112602).

SUPPLEMENTARY MATERIAL

The Supplementary Material for this article can be found online at: https://www.frontiersin.org/articles/10.3389/fonc.2021.740732/full#supplementary-material

REFERENCES

1. Bray F, Ferlay J, Soerjomataram I, Siegel RL, Torre LA, Jemal A. Global Cancer Statistics 2018: GLOBOCAN Estimates of Incidence and Mortality Worldwide for 36 Cancers in 185 Countries. *CA Cancer J Clin* (2018) 68 (6):394–424. doi: 10.3322/caac.21492
2. Necula L, Matei L, Dragu D, Neagu AI, Mambet C, Nedeianu S, et al. Recent Advances in Gastric Cancer Early Diagnosis. *World J Gastroenterol* (2019) 25 (17):2029–44. doi: 10.3748/wjg.v25.i17.2029
3. Smyth EC, Nilsson M, Grabsch HI, van Grieken NC, Lordick F. Gastric Cancer. *Lancet* (2020) 396(10251):635–48. doi: 10.1016/s0140-6736(20) 31288-5
4. Murad AM, Santiago FF, Petroianu A, Rocha PR, Rodrigues MA, Rausch M. Modified Therapy With 5-Fluorouracil, Doxorubicin, and Methotrexate in Advanced Gastric Cancer. *Cancer* (1993) 72(1):37–41. doi: 10.1002/1097-0142(19930701)72:1<37::aid-cncr2820720109>3.0.co;2-p
5. Fuchs CS, Shitara K, Di Bartolomeo M, Lonardi S, Al-Batran SE, Van Cutsem E, et al. Ramucirumab With Cisplatin and Fluoropyrimidine as First-Line Therapy in Patients With Metastatic Gastric or Junctional Adenocarcinoma (RAINFALL): A Double-Blind, Randomised, Placebo-Controlled, Phase 3 Trial. *Lancet Oncol* (2019) 20(3):420–35. doi: 10.1016/s1470-2045(18)30791-5
6. Shah MA, Bang YJ, Lordick F, Alsina M, Chen M, Hack SP, et al. Effect of Fluorouracil, Leucovorin, and Oxaliplatin With or Without Onartuzumab in HER2-Negative, MET-Positive Gastroesophageal Adenocarcinoma: The METGastric Randomized Clinical Trial. *JAMA Oncol* (2017) 3(5):620–7. doi: 10.1001/jamaoncol.2016.5580
7. Van Cutsem E, Moiseyenko VM, Tjulandin S, Majlis A, Constenla M, Boni C, et al. Phase III Study of Docetaxel and Cisplatin Plus Fluorouracil Compared With Cisplatin and Fluorouracil as First-Line Therapy for Advanced Gastric Cancer: A Report of the V325 Study Group. *J Clin Oncol* (2006) 24(31):4991–7. doi: 10.1200/jco.2006.06.8429
8. Glimelius B, Ekström K, Hoffman K, Graf W, Sjödén PO, Haglund U, et al. Randomized Comparison Between Chemotherapy Plus Best Supportive Care With Best Supportive Care in Advanced Gastric Cancer. *Ann Oncol* (1997) 8 (2):163–8. doi: 10.1023/a:1008243606668
9. Van Cutsem E, Sagaert X, Topal B, Haustermans K, Prenen H. Gastric Cancer. *Lancet* (2016) 388(10060):2654–64. doi: 10.1016/s0140-6736(16) 30354-3
10. Du M, Ouyang Y, Meng F, Ma Q, Liu H, Zhuang Y, et al. Nanotargeted Agents: An Emerging Therapeutic Strategy for Breast Cancer. *Nanomedicine (Lond)* (2019) 14(13):1771–86. doi: 10.2217/nnm-2018-0481
11. Al Ajmi E, Forghani B, Reinhold C, Bayat M, Forghani R. Spectral Multi-Energy CT Texture Analysis With Machine Learning for Tissue Classification: An Investigation Using Classification of Benign Parotid Tumours as a Testing Paradigm. *Eur Radiol* (2018) 28(6):2604–11. doi: 10.1007/s00330-017-5214-0
12. Marin D, Boll DT, Mileto A, Nelson RC. State of the Art: Dual-Energy CT of the Abdomen. *Radiology* (2014) 271(2):327–42. doi: 10.1148/radiol.14131480
13. Seidler M, Forghani B, Reinhold C, Pérez-Lara A, Romero-Sanchez G, Muthukrishnan N, et al. Dual-Energy CT Texture Analysis With Machine Learning for the Evaluation and Characterization of Cervical Lymphadenopathy. *Comput Struct Biotechnol J* (2019) 17:1009–15. doi: 10.1016/j.csbj.2019.07.004
14. Li J, Dong D, Fang M, Wang R, Tian J, Li H, et al. Dual-Energy CT-Based Deep Learning Radiomics can Improve Lymph Node Metastasis Risk Prediction for Gastric Cancer. *Eur Radiol* (2020) 30(4):2324–33. doi: 10.1007/s00330-019-06621-x
15. Han D, Yu Y, He T, Yu N, Dang S, Wu H, et al. Effect of Radiomics From Different Virtual Monochromatic Images in Dual-Energy Spectral CT on the WHO/ISUP Classification of Clear Cell Renal Cell Carcinoma. *Clin Radiol* (2021) 76(8):627.e23–627.e29. doi: 10.1016/j.crad.2021.02.033
16. Tang L, Li ZY, Li ZW, Zhang XP, Li YL, Li XT, et al. Evaluating the Response of Gastric Carcinomas to Neoadjuvant Chemotherapy Using Iodine Concentration on Spectral CT: A Comparison With Pathological Regression. *Clin Radiol* (2015) 70(11):1198–204. doi: 10.1016/j.crad.2015.06.083
17. Gerlinger M, Rowan AJ, Horswell S, Math M, Larkin J, Endesfelder D, et al. Intratumor Heterogeneity and Branched Evolution Revealed by Multiregion Sequencing. *N Engl J Med* (2012) 366(10):883–92. doi: 10.1056/NEJMoa1113205
18. Caswell DR, Swanton C. The Role of Tumour Heterogeneity and Clonal Cooperativity in Metastasis, Immune Evasion and Clinical Outcome. *BMC Med* (2017) 15(1):133. doi: 10.1186/s12916-017-0900-y

19. Ligero M, Garcia-Ruiz A, Viaplana C, Villacampa G, Raciti MV, Landa J, et al. A CT-Based Radiomics Signature Is Associated With Response to Immune Checkpoint Inhibitors in Advanced Solid Tumors. *Radiology* (2021) 299 (1):109–19. doi: 10.1148/radiol.2021200928
20. Dong D, Fang MJ, Tang L, Shan XH, Gao JB, Giganti F, et al. Deep Learning Radiomic Nomogram can Predict the Number of Lymph Node Metastasis in Locally Advanced Gastric Cancer: An International Multicenter Study. *Ann Oncol* (2020) 31(7):912–20. doi: 10.1016/j.annonc.2020.04.003
21. Dong D, Tang L, Li ZY, Fang MJ, Gao JB, Shan XH, et al. Development and Validation of an Individualized Nomogram to Identify Occult Peritoneal Metastasis in Patients With Advanced Gastric Cancer. *Ann Oncol* (2019) 30 (3):431–8. doi: 10.1093/annonc/mdz001
22. Dong D, Zhang F, Zhong LZ, Fang MJ, Huang CL, Yao JJ, et al. Development and Validation of a Novel MR Imaging Predictor of Response to Induction Chemotherapy in Locoregionally Advanced Nasopharyngeal Cancer: A Randomized Controlled Trial Substudy (NCT01245959). *BMC Med* (2019) 17(1):190. doi: 10.1186/s12916-019-1422-6
23. Lambin P, Rios-Velazquez E, Leijenaar R, Carvalho S, van Stiphout RG, Granton P, et al. Radiomics: Extracting More Information From Medical Images Using Advanced Feature Analysis. *Eur J Cancer* (2012) 48(4):441–6. doi: 10.1016/j.ejca.2011.11.036
24. Hu H, Gong L, Dong D, Zhu L, Wang M, He J, et al. Identifying Early Gastric Cancer Under Magnifying Narrow-Band Images With Deep Learning: A Multicenter Study. *Gastrointest Endosc* (2021) 93(6):1333–41.e3. doi: 10.1016/j.gie.2020.11.014
25. Meng L, Dong D, Chen X, Fang M, Wang R, Li J, et al. 2D and 3D CT Radiomic Features Performance Comparison in Characterization of Gastric Cancer: A Multi-Center Study. *IEEE J BioMed Health Inform* (2021) 25 (3):755–63. doi: 10.1109/jbhi.2020.3002805
26. Li Z, Zhang D, Dai Y, Dong J, Wu L, Li Y, et al. Computed Tomography-Based Radiomics for Prediction of Neoadjuvant Chemotherapy Outcomes in Locally Advanced Gastric Cancer: A Pilot Study. *Chin J Cancer Res* (2018) 30(4):406–14. doi: 10.21147/j.issn.1000-9604.2018.04.03
27. Sun KY, Hu HT, Chen SL, Ye JN, Li GH, Chen LD, et al. CT-Based Radiomics Scores Predict Response to Neoadjuvant Chemotherapy and Survival in Patients With Gastric Cancer. *BMC Cancer* (2020) 20(1):468. doi: 10.1186/s12885-020-06970-7
28. Zhang L, Dong D, Zhang W, Hao X, Fang M, Wang S, et al. A Deep Learning Risk Prediction Model for Overall Survival in Patients With Gastric Cancer: A Multicenter Study. *Radiother Oncol* (2020) 150:73–80. doi: 10.1016/j.radonc.2020.06.010
29. Zhang W, Fang M, Dong D, Wang X, Ke X, Zhang L, et al. Development and Validation of a CT-Based Radiomic Nomogram for Preoperative Prediction of Early Recurrence in Advanced Gastric Cancer. *Radiother Oncol* (2020) 145:13–20. doi: 10.1016/j.radonc.2019.11.023
30. Eisenhauer EA, Therasse P, Bogaerts J, Schwartz LH, Sargent D, Ford R, et al. New Response Evaluation Criteria in Solid Tumours: Revised RECIST Guideline (Version 1.1). *Eur J Cancer* (2009) 45(2):228–47. doi: 10.1016/j.ejca.2008.10.026
31. Amin MB, Edge SB, Greene FL, Byrd DL, Brookland RK, Washington MK, et al. *AJCC Cancer Staging Manual. 8th ed*. New York, NY: Springer (2017).
32. Borchard F. Classification of Gastric Carcinoma. *Hepatogastroenterology* (1990) 37(2):223–32.
33. Silva AC, Morse BG, Hara AK, Paden RG, Hongo N, Pavlicek W. Dual-Energy (Spectral) CT: Applications in Abdominal Imaging. *Radiographics* (2011) 31 (4):1031–46; discussion 1047-50. doi: 10.1148/rg.314105159
34. Zwanenburg A, Vallieres M, Abdalah MA, Aerts H, Andrearczyk V, Apte E, et al. The Image Biomarker Standardization Initiative: Standardized Quantitative Radiomics for High-Throughput Image-Based Phenotyping. *Radiology* (2020) 295(2):328–38. doi: 10.1148/radiol.2020191145
35. Tan JW, Wang L, Chen Y, Xi W, Ji J, Wang L, et al. Predicting Chemotherapeutic Response for Far-Advanced Gastric Cancer by Radiomics With Deep Learning Semi-Automatic Segmentation. *J Cancer* (2020) 11(24):7224–36. doi: 10.7150/jca.46704
36. Tian X, Sun C, Liu Z, Li W, Duan H, Wang L, et al. Prediction of Response to Preoperative Neoadjuvant Chemotherapy in Locally Advanced Cervical Cancer Using Multicenter CT-Based Radiomic Analysis. *Front Oncol* (2020) 10:77. doi: 10.3389/fonc.2020.00077
37. Homayounieh F, Singh R, Nitiwarangkul C, Lades F, Schmidt B, Sedlmair M, et al. Semiautomatic Segmentation and Radiomics for Dual-Energy CT: A Pilot Study to Differentiate Benign and Malignant Hepatic Lesions. *AJR Am J Roentgenol* (2020) 215(2):398–405. doi: 10.2214/ajr.19.22164
38. Zhou Y, Su GY, Hu H, Ge YQ, Si Y, Shen MP, et al. Radiomics Analysis of Dual-Energy CT-Derived Iodine Maps for Diagnosing Metastatic Cervical Lymph Nodes in Patients With Papillary Thyroid Cancer. *Eur Radiol* (2020) 30(11):6251–62. doi: 10.1007/s00330-020-06866-x
39. Wu J, Zhang Q, Zhao Y, Liu Y, Chen A, Li X, et al. Radiomics Analysis of Iodine-Based Material Decomposition Images With Dual-Energy Computed Tomography Imaging for Preoperatively Predicting Microsatellite Instability Status in Colorectal Cancer. *Front Oncol* (2019) 9:1250. doi: 10.3389/fonc.2019.01250
40. Wang L, Zhang Y, Chen Y, Tan J, Wang L, Zhang J, et al. The Performance of a Dual-Energy CT Derived Radiomics Model in Differentiating Serosal Invasion for Advanced Gastric Cancer Patients After Neoadjuvant Chemotherapy: Iodine Map Combined With 120-kV Equivalent Mixed Images. *Front Oncol* (2020) 10:562945. doi: 10.3389/fonc.2020.562945
41. Reinert CP, Krieg EM, Bösmüller H, Horger M. Mid-Term Response Assessment in Multiple Myeloma Using a Texture Analysis Approach on Dual Energy-CT-Derived Bone Marrow Images - A Proof of Principle Study. *Eur J Radiol* (2020) 131:109214. doi: 10.1016/j.ejrad.2020.109214
42. Choe J, Lee SM, Do KH, Lee JB, Lee SM, Lee JG, et al. Prognostic Value of Radiomic Analysis of Iodine Overlay Maps From Dual-Energy Computed Tomography in Patients With Resectable Lung Cancer. *Eur Radiol* (2019) 29 (2):915–23. doi: 10.1007/s00330-018-5639-0
43. Marin D, Davis D, Roy Choudhury K, Patel B, Gupta RT, Mileto A, et al. Characterization of Small Focal Renal Lesions: Diagnostic Accuracy With Single-Phase Contrast-Enhanced Dual-Energy CT With Material Attenuation Analysis Compared With Conventional Attenuation Measurements. *Radiology* (2017) 284(3):737–47. doi: 10.1148/radiol.2017161872
44. Kaza RK, Caoili EM, Cohan RH, Platt JF. Distinguishing Enhancing From Nonenhancing Renal Lesions With Fast Kilovoltage-Switching Dual-Energy CT. *AJR Am J Roentgenol* (2011) 197(6):1375–81. doi: 10.2214/ajr.11.6812
45. Ogata T, Ueguchi T, Yagi M, Yamada S, Tanaka C, Ogihara R, et al. Feasibility and Accuracy of Relative Electron Density Determined by Virtual Monochromatic CT Value Subtraction at Two Different Energies Using the Gemstone Spectral Imaging. *Radiat Oncol* (2013) 8:83. doi: 10.1186/1748-717x-8-83
46. Ozguner O, Dhanantwari A, Halliburton S, Wen G, Utrup S, Jordan D. Objective Image Characterization of a Spectral CT Scanner With Dual-Layer Detector. *Phys Med Biol* (2018) 63(2):025027. doi: 10.1088/1361-6560/aa9e1b
47. Cha J, Kim HJ, Kim ST, Kim YK, Kim HY, Park GM. Dual-Energy CT With Virtual Monochromatic Images and Metal Artifact Reduction Software for Reducing Metallic Dental Artifacts. *Acta Radiol* (2017) 58(11):1312–9. doi: 10.1177/0284185117692174
48. Sun EX, Wortman JR, Uyeda JW, Lacson R, Sodickson AD. Virtual Monoenergetic Dual-Energy CT for Evaluation of Hepatic and Splenic Lacerations. *Emerg Radiol* (2019) 26(4):419–25. doi: 10.1007/s10140-019-01687-y
49. Deniffel D, Sauter A, Fingerle A, Rummeny EJ, Makowski MR, Pfeiffer D. Improved Differentiation Between Primary Lung Cancer and Pulmonary Metastasis by Combining Dual-Energy CT-Derived Biomarkers With Conventional CT Attenuation. *Eur Radiol* (2021) 31(2):1002–10. doi: 10.1007/s00330-020-07195-9
50. Baxa J, Matouskova T, Krakorova G, Schmidt B, Flohr T, Sedlmair M, et al. Dual-Phase Dual-Energy CT in Patients Treated With Erlotinib for Advanced Non-Small Cell Lung Cancer: Possible Benefits of Iodine Quantification in Response Assessment. *Eur Radiol* (2016) 26(8):2828–36. doi: 10.1007/s00330-015-4092-6
51. Li J, Fang M, Wang R, Dong D, Tian J, Liang P, et al. Diagnostic Accuracy of Dual-Energy CT-Based Nomograms to Predict Lymph Node Metastasis in Gastric Cancer. *Eur Radiol* (2018) 28(12):5241–4. doi: 10.1007/s00330-018-5483-2
52. Lv P, Lin XZ, Li J, Li W, Chen K. Differentiation of Small Hepatic Hemangioma From Small Hepatocellular Carcinoma: Recently Introduced Spectral CT Method. *Radiology* (2011) 259(3):720–9. doi: 10.1148/radiol.11101425
53. Zhao H, Li W, Huang W, Yang Y, Shen W, Liang P, et al. Dual-Energy CT-Based Nomogram for Decoding HER2 Status in Patients With Gastric Cancer. *AJR Am J Roentgenol* (2021) 216(6):1539–48. doi: 10.2214/ajr.20.23528

54. Pan Z, Pang L, Ding B, Yan C, Zhang H, Du L, et al. Gastric Cancer Staging With Dual Energy Spectral CT Imaging. *PloS One* (2013) 8(2):e53651. doi: 10.1371/journal.pone.0053651
55. Xu JJ, Taudorf M, Ulriksen PS, Achiam MP, Resch TA, Nielsen MB, et al. Gastrointestinal Applications of Iodine Quantification Using Dual-Energy CT: A Systematic Review. *Diagnostics (Basel)* (2020) 10(10):814. doi: 10.3390/diagnostics10100814
56. Wang ZL, Li YL, Li XT, Tang L, Li ZY, Sun YS. Role of CT in the Prediction of Pathological Complete Response in Gastric Cancer After Neoadjuvant Chemotherapy. *Abdom Radiol (NY)* (2021) 46(7):3011–8. doi: 10.1007/s00261-021-02967-3
57. Jacobsen MC, Schellingerhout D, Wood CA, Tamm EP, Godoy MC, Sun J, et al. Intermanufacturer Comparison of Dual-Energy CT Iodine Quantification and Monochromatic Attenuation: A Phantom Study. *Radiology* (2018) 287(1):224–34. doi: 10.1148/radiol.2017170896

Conflict of Interest: Author S-sL was employed by the company Siemens Healthineers Ltd.

The remaining authors declare that the research was conducted in the absence of any commercial or financial relationships that could be construed as a potential conflict of interest.

Publisher's Note: All claims expressed in this article are solely those of the authors and do not necessarily represent those of their affiliated organizations, or those of the publisher, the editors and the reviewers. Any product that may be evaluated in this article, or claim that may be made by its manufacturer, is not guaranteed or endorsed by the publisher.

frontiers in Oncology

ORIGINAL RESEARCH
published: 30 March 2022
doi: 10.3389/fonc.2022.836098

Radiomics in Gastric Cancer: First Clinical Investigation to Predict Lymph Vascular Invasion and Survival Outcome Using ^{18}F-FDG PET/CT Images

Liping Yang[1†], Wenjie Chu[1†], Mengyue Li[2], Panpan Xu[1], Menglu Wang[1], Mengye Peng[1], Kezheng Wang[1] and Lingbo Zhang[3*]*

[1] Department of PET-CT, Harbin Medical University Cancer Hospital, Harbin, China, [2] College of Bioinformatics Science and Technology, Harbin Medical University, Harbin, China, [3] Oral Department, The Second Affiliated Hospital of Harbin Medical University, Harbin, China

OPEN ACCESS

Edited by:
Damiano Caruso,
Sapienza University of Rome, Italy

Reviewed by:
Orazio Schillaci,
University of Rome Tor Vergata, Italy
Felix Berlth,
Johannes Gutenberg University Mainz, Germany

***Correspondence:**
Kezheng Wang
wangkezheng9954001@163.com
Lingbo Zhang
zld2003@163.com

[†]These authors have contributed equally to this work and share first authorship

Specialty section:
This article was submitted to Gastrointestinal Cancers: Gastric & Esophageal Cancers, a section of the journal Frontiers in Oncology

Received: 15 December 2021
Accepted: 23 February 2022
Published: 30 March 2022

Citation:
Yang L, Chu W, Li M, Xu P, Wang M, Peng M, Wang K and Zhang L (2022) Radiomics in Gastric Cancer: First Clinical Investigation to Predict Lymph Vascular Invasion and Survival Outcome Using ^{18}F-FDG PET/CT Images. Front. Oncol. 12:836098. doi: 10.3389/fonc.2022.836098

Background: Lymph vascular invasion (LVI) is an unfavorable prognostic indicator in gastric cancer (GC). However, there are no reliable clinical techniques for preoperative predictions of LVI. The aim of this study was to develop and validate PET/CT-based radiomics signatures for predicting LVI of GC preoperatively. Radiomics nomograms were also established to predict patient survival outcomes.

Methods: This retrospective study registered 148 GC patients with histopathological confirmation for LVI status, who underwent pre-operative PET/CT scans (Discovery VCT 64 PET/CT system) from December 2014 to June 2019. Clinic-pathological factors (age, gender, and tumor grade, etc.) and metabolic PET data (maximum and mean standardized uptake value, total lesion glycolysis and metabolic tumor volume) were analyzed to identify independent LVI predictors. The dataset was randomly assigned to either the training set or test set in a 7:3 ratios. Three-dimensional (3D) radiomics features were extracted from each PET- and CT-volume of interests (VOI) singularly, and then a radiomics signature (RS) associated with LVI status is built by feature selection. Four models with different modalities (PET-RS: only PET radiomics features; CT-RS: only CT radiomics features; PET/CT-RS: both PET and CT radiomics features; PET/CT-RS plus clinical data) were developed to predict LVI. Patients were postoperatively followed up with PET/CT every 6-12 months for the first two years and then annually up to five years after surgery. The PET/CT radiomics score (Rad-scores) was calculated to assess survival outcome, and corresponding nomograms with radiomics (NWR) or without radiomics (NWOR) were established.

Results: Tumor grade and maximum standardized uptake value (SUVmax) were the independent LVI predictor. 1037 CT and PET 3D radiomics features were extracted separately and reduced to 4 and 5 features to build CT-RS and PET-RS, respectively. PET/CT-RS and PET/CT-RS plus clinical data (tumor grade and SUVmax) were also

developed. The ROC analysis demonstrated clinical usefulness of PET/CT-RS plus clinical data (AUC values for training and validation, respectively 0.936 and 0.914) and PET/CT-RS (AUC values for training and validation, respectively 0.881 and 0.854), which both are superior to CT-RS (0.838 and 0.824) and PET-RS (0.821 and 0.812). SUVmax and LVI were independent prognostic indicators of both OS and PFS. Decision curve analysis (DCA) demonstrated NWR outperformed NWOR and was established to assess survival outcomes. For estimation of OS and PFS, the C-indexes of the NWR were 0. 88 and 0.88 in the training set, respectively, while the C-indexes of the NWOR were 0. 82 and 0.85 in the training set, respectively.

Conclusions: The PET/CT-based radiomics analysis might serve as a non-invasive approach to predict LVI status in GC patients and provide effective predictors of patient survival outcomes.

Keywords: gastric cancer, PET-CT, nomogram, lymph vascular invasion, survival prognosis, radiomics

INTRODUCTION

Gastric cancer (GC) is currently one of the most common malignant tumors, accounting for the second-highest number of cancer-related fatalities worldwide, seriously threatening human health and life safety (1). Furthermore, approximately 70% of cases occur in Asia, with China accounting for at least half of all cases. Surgical resection is taken as the standard treatment approach for GC that is surgically resectable (2). Unfortunately, the poor survival prognosis arising from postoperative tumor recurrence is still a clinical dilemma. It has been reported that the recurrence rate of GC patients within two years after radical resection was 61.7%, and the average recurrence time was 24.3 months. Especially, 90% of patients with stage III GC had a recurrence rate of 50% and 40% in the first and second years after surgery (3, 4). At present, there are currently no efficient and reliable prognostic bio-markers for identifying high-risk groups for adjuvant therapy in clinical practice.

Malignant tumor cell metastasis is the leading cause of death in patients with malignant tumors, in which lymphatic metastasis is the main way. Lymph vascular invasion (LVI) refers to the infiltration of tumor cells in the lumen of arteries, veins, or lymphatic vessels during histologic examination with hematoxylin and eosin (H&E) stains, D2-40 and CD31 stains, which has previously been demonstrated to prompt the local recurrence and distant metastasis of tumors (5, 6). For instance, LVI has been reported to be an independent prognostic factor for the overall survival (OS) and disease-free survival (PFS) of breast cancer patients (7, 8). Thus, accurate identification of LVI status is conductive to develop personalized treatment planning for breast cancer patients. Meanwhile, a series of studies have found that the occurrence of pathological LVI was closely associated with the progression of GC and poor clinical prognosis. The incidence of LVI was 25% and 44% in moderately and well differentiated and poorly differentiated gastric cancers, respectively, while the 5-year survival rate of GC was only 37.7% in patients with LVI-positive, which was significantly lower than 59.9% of patients with LVI-negative (9–12). Although LVI is considered to be a key prognostic factor of unsatisfactory survival outcomes in various cancers, accurate identification of LVI status prior to operation is still difficult because LVI is mainly found through postoperative pathology.

^{18}F-fluorodeoxyglucose(^{18}F-FDG) positron emission tomography-computed tomography (PET-CT), as a prospect imaging modality, plays a vital role in preoperative staging, treatment efficacy evaluation, tumor residual, and recurrence identification of GC. Nevertheless, predicting LVI of GC patients using quantitative PET metabolic parameters has received minimal attention. Lin et al. found that ratio maximum standardized uptake values (SUVmax) to mean standardized uptake values (SUVmean) is an independent predictor of LVI in hepatocellular carcinoma (13). Noda et al. reported that SUVmax of lung cancer could be employed for the identification of LVI (14). Unfortunately, the clinical usefulness of all these metabolic parameters in predicting LVI has not been demonstrated in GC, which needs to be deeply investigated.

Radiomics, which transformed digital medical images into high-throughput data, is a promising and non-invasive method that can extract high-throughput features (such as shape, intensity, and texture features) (15). It captures relationships between image voxels that may not be perceived by the naked eyes of physicians-even experienced radiologists, which can contribute to the diagnostic and predictive accuracy of the disease (16). Xu et al. reported that total lesion glycolysis (TLG) might be the best indicator for predicting lymph vascular space invasion (LVSI) in cervical cancer without lymphatic metastasis (17). Nie et al. investigated the clinical value of the PET/CT-based radiomics analysis in predicting LVI status, and the results demonstrated the favorable predictive efficacy for LVI status in lung adenocarcinoma patients (18). Several works focused on predicting the LVI status of GC using computed tomography (CT)-derived radiomics features have previously been reported. Chen et al. demonstrated that radiomics analysis based on contrast-enhanced computed tomography (CECT) may help to predict LVI status and PFS (19). In Meng et al.'s study, models constructed with two-

dimensional (2D) radiomics features revealed comparable performances with those constructed with three-dimensional (3D) features in predicting LVI status (20). However, to our knowledge, no previous study has focused on the clinical value of PET-based radiomic signatures in the preoperative prediction of LVI in GC.

In the present study, we intended to develop and validate the PET/CT-based radiomics models for preoperatively predicting the LVI status of GC. Furthermore, we also investigated whether the PET/CT-based nomogram can be applied as a non-invasive method to assess patient survival outcomes.

MATERIALS AND METHODS

Ethical approval was obtained for this retrospective study, and the need for written informed consent was waived. The enrolment flowchart of this study is displayed in **Supplementary Figure 1**. A total of 148 patients with pathologically confirmed GC from December 2014 to June 2019 were enrolled in this study according to the following inclusion criteria:1) PET/CT scans were performed before surgery;2) GC patients with clear pathologically confirmed LVI on surgical resection specimens;3) No previous anti-tumor therapy before surgery such as radiotherapy, chemotherapy and neoadjuvant therapy;4) Patients with detailed clinical data and follow-up information (OS and PFS were followed up until September 30, 2020). The exclusion criteria were as follows: 1) Poor image quality (artifacts related to patient motion, which was assessed by a senior radiologist who has 15-year specialized experience); 2) History of other malignant tumors. Clinical information was obtained through clinical medical record retrieval, including age, gender, lymph node metastasis, cTNM, T stage, N stage, M stage, molecular subtype, tumor grade, tumor thickness, carcinoembryonic antigen (CEA), carbohydrate antigen 125 (CA125), carbohydrate antigen199 (CA199), SUVmax, SUVmean, metabolic tumor volume (MTV) and TLG.

Image Acquisition

Prior to scanning, all patients were required to fast for at least 6 hours. All patients' blood glucose levels should be kept below 11.0 mmol/L. PET/CT images were acquired using the Discovery VCT 64 PET/CT system (GE Healthcare, Milwaukee, USA). A total of 1000-1200ml contrast agent (Meglumine diatrizoate at a concentration of 2%) was injected into the patients 15 minutes before the examinations to fill the gastric cavity, which is a cheap, effective and well-tolerated intracavitary contrast agent with minimal adverse effects. A 3.78 MBq/kg dose of ^{18}F-FDG was administered intravenously, and approximately one hour later, whole-body CT scanning was performed. Specific imaging parameters were listed as follows: tube voltage 140 kV, tube current 140 mA, slice thickness 3 mm, reconstruction interval 3 mm, matrix size 512 × 512, and field of view 650 mm. After the CT scan, the emission scan was followed by a 1.5-2 min transmission scan per bed position. After the completion of the CT scan, the PET emission scan was followed by a 2 min per bed position. Image reconstructions were performed based on the 3D ordered subset expectation-maximization algorithm (2 iterations and 17 subsets).

Image Analysis

The PET/CT images were analyzed by two radiologists blinded to the clinical and pathological results, (Reader 1, P.X and Reader 2, C.G with 10- and 15-years' experience in the interpretation of PET/CT images, respectively). The metabolic parameters were measured by drawing a region-of-interest (ROI) on the axial PET image based on a threshold of 40% of SUVmax using commercial software (PET VCAR; GE Healthcare, USA). Any disagreement was resolved by consensus. SUVmax was defined at the highest value on one pixel with the highest counts within the ROI (21).

Tumor Segmentation and Radiomics Feature Extraction

The overview of the radiomics workflow is displayed in **Figure 1**. Axial PET and CT Digital Imaging and Communications in Medicine images obtained from the Picture Archiving and Communication System were applied for tumor segmentation. The tumor lesion was delineated on axial PET and CT images using LIFEx software (open-source software; www.lifexsoft.org/index.php) (**Figure 1A**). All 3D segmentation was first delineated automatically by means of a fixed threshold of 40% of the SUVmax, which were corrected by a radiologist manually afterward, blinded to surgical and pathological results.

We adopted three steps to preprocess the PET and CT images prior to feature extraction (22). Firstly, we resampled all images to a uniform voxel size of 1 mm × 1 mm × 1 mm using linear interpolation to minimize the influence of different layer thicknesses. Secondly, based on the gray-scale discretization process (bin width for CT = 25, bin width for PET = 0.1), we convert the continuous image into discrete values. Finally, we use the Laplacian of Gaussian and wavelet image filters to eliminate the mixed noise in the image digitization process in order to obtain low- or high-frequency features. Radiomics features were extracted from each PET-derived volume of interest (VOI) and CT-derived VOI by applying dedicated AK software (Artificial Intelligence Kit; GE Healthcare), which is in compliance with image biomarker standardization initiative guidelines (23). A total of 2074 radiomics features were extracted from each VOIs (1037 for CT, 1037 for PET) including (i) 198 for first-order feature, (ii) 14 for shape feature, (iii) 264 for gray level co-occurrence matrix (GLCM) feature, (iv) 176 for gray level size zone matrix (GLSZM) feature, (v) 176 for gray level run length matrix (GLRLM) feature, (vi) 55 for neighborhood gray tone difference matrix (NGTDM) feature, (vii) 154 for gray level dependence matrix (GLDM) feature.

Radiomic Feature Selection and Model Development

After the radiomics features extraction, Z-score normalization was done on each radiomics feature. In addition, the same preprocessing procedure was also applied to the testing set. The dataset was randomly assigned to either the training set or

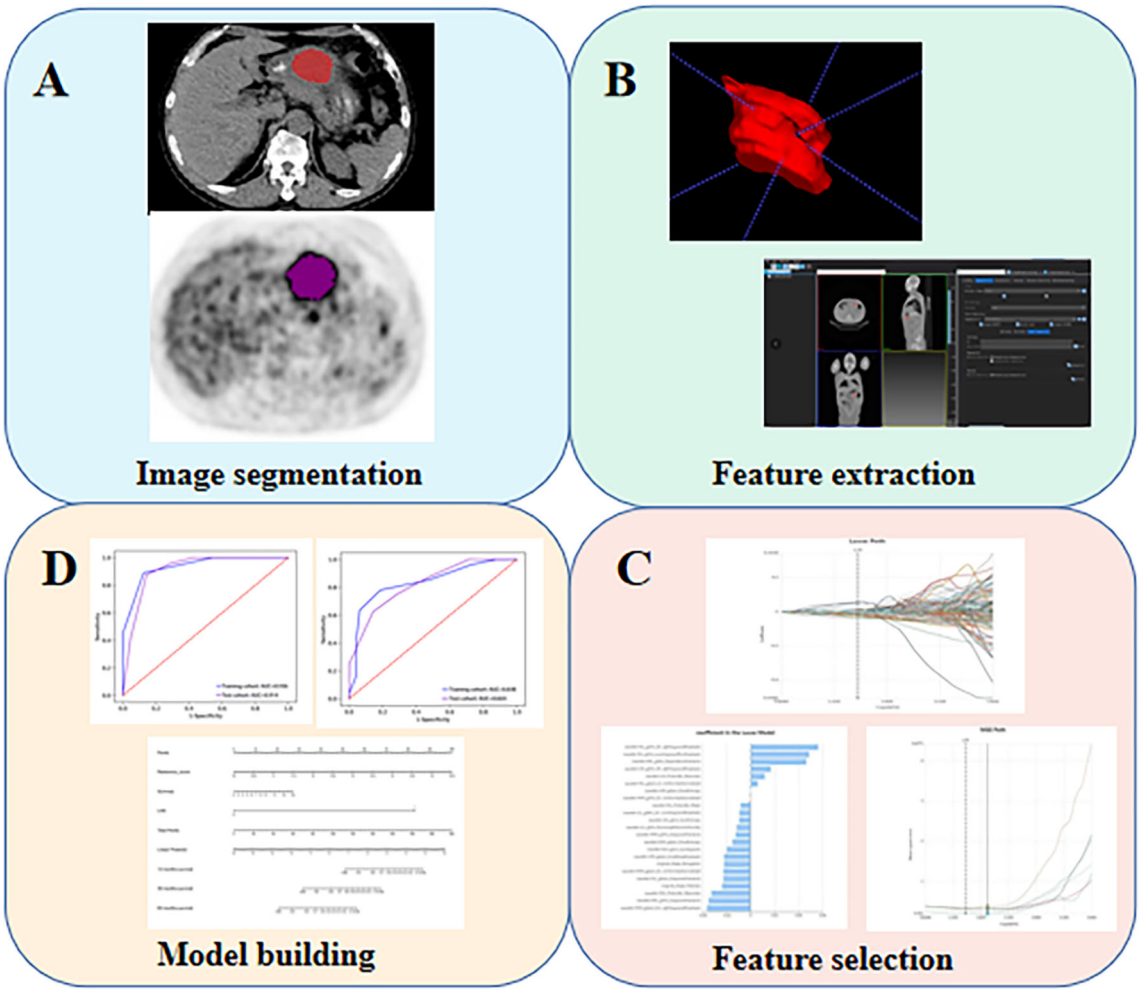

FIGURE 1 | The flow diagram of this study. **(A)** Image segmentation; **(B)** Feature extraction; **(C)** Feature selection; **(D)** Model building.

test set in 7:3 ratios. All cases in the training set were used to train the predictive model, while cases in the test set were utilized to independently evaluate the model's performance.

Firstly, intra- and inter-class correlation coefficients (ICCs) were calculated to assess the intra- and inter-observer reproducibility. Reader 1 and Reader 2 drew the VOIs of 40 cases (20 LVI-present GCs and 20 LVI-absent GCs) of CT images and PET images randomly selected from the whole cohort. Reader 1 repeated the segmentations two weeks later. ICC greater than 0.80 indicated good agreement of feature extraction. The VOI segmentation for the remaining cases were performed by Reader 1. Next, the feature selection was carried out by using a step-by-step selection method. Firstly, univariate logistic regression analysis with the Mann-Whitney U test was utilized to select features with P-value< 0.05 for the subsequent analysis. Secondly, multivariate logistic regression analysis was applied to choose features closely related to LVI status. Finally, a subset of the most informative features was retained using the least absolute shrinkage and selection operator (LASSO) method. The k-Nearest Neighbor (KNN) was applied for model construction, and four sets of machine learning models (a CT-RS, a PET-RS, a PET/CT-RS, a PET/CT-RS incorporating clinical and metabolic parameters) were developed to predict LVI of GC. The diagnostic performance of the radiomics models was evaluated regarding the area under the curve (AUC), sensitivity, specificity, and accuracy.

Construction of Radiomics Nomograms

In this study, among all pathologic and therapeutic factors, SUVmax and pathologic LVI were demonstrated to be associated with survival prognosis, which were incorporated into the nomogram's construction (**Supplementary Tables 4–7**). A PET/CT radiomics score (Rad-scores) was calculated, and corresponding nomograms with radiomics (NWR) or without radiomics (NWOR) were established by incorporating the independent LVI predictors as well as the Rad-score to assess survival outcome. Calibration curve analysis and Decision curve analysis (DCA) were performed to assess the clinical value of the nomograms.

Follow Up and Survival Analysis

Patients were postoperatively followed up every 6-12 months for the first 2 years and then annually up to five years. The endpoints of this study were PFS and OS. PFS is defined as the time interval from surgery to the recurrence or progression of the disease. OS is defined as the time interval from surgery to death. Survival curves were drawn using the Kaplan-Meier approach and compared using the log-rank test. All the prognostic factors (including pathologic LVI status, gender, age, lymph node metastasis, tumor grade, molecular subtype, T stage, N stage, M stage, cTNM, CEA, CA125, CA199, Tumor thickness, SUVmax, SUVmean, MTV and TLG were evaluated by univariate analysis using the Kaplan-Meier approach. Statistically significant variables were analyzed for the multivariate Cox forward stepwise regression model to select independent predictors of OS and PFS.

Statistical Analyses

Univariate analysis (chi-square test or Mann-Whitney U test) and multivariate logistic regression was used to screen out final significant variables by using SPSS software (Version 25.0, IBM). ICC, receiver operating curve (ROC) analysis, calibration plots, DCA, and survival analysis were performed with R statistical software (version 3.5.1). A two-sided *P*-value< 0.001 was used as the criterion to indicate a statistically significant difference.

RESULTS

Patient Characteristics

A total of 148 patients (103 males and 45 females; average age 61; median age 60 years; age range 35-85 years) were recruited for this study, including 69 cases of LVI-present and 79 cases of LVI-absent. The clinic-pathological variables and PET metabolic parameters of all patients are displayed in **Table 1**. In univariate logistic regression analysis, there was no significant statistical difference in gender, age, molecular subtype, T stage, M stage, cTNM, CEA, CA125, CA199, tumor thickness, SUVmean and MTV between LVI-present and LVI-absent groups ($P > 0.001$), while lymph node metastasis, tumor grade, N stage, SUVmax and TLG were statistically significant ($P < 0.001$). Among these parameters, tumor grade and SUVmax were further shown to be independent LVI predictors (**Supplementary Table 2**).

Intra and Inter-Observer Reproducibility of Feature Extraction

The intra-observer ICC ranged from 0.811 to 0.920, and inter-observer ICCs were ranged from 0.740 to 0.902. Therefore, a favorable intra- and inter-observer reproducibility of radiomics feature extraction was observed in our study.

Performance of the Four Models

After proper feature selection, 4, 5, 9, and 11 RSs were selected respectively to develop the CT-RS, PET-RS, PET/CT-RS, and clinical parameters integrated models for predicting LVI status in GC. After using a step-by-step selection method, four CT and five PET radiomics features were eventually selected to build CT-RS and PET-RS, respectively. Radiomics features and corresponding coefficients and their significance are listed in **Supplementary Table 3**. The ROC analysis demonstrated the clinical usefulness of the integrated model and PET/CT-RS, which both are superior to the CT-RS and PET-RS. All results regarding diagnostic efficacy were demonstrated in **Table 2**, and the ROC curves were as displayed in **Figure 2**. The ROC analysis demonstrated a favorable clinical usefulness of PET/CT-RS plus clinical data (AUC values for training and validation, respectively 0.936 and 0.914) and PET/CT-RS (AUC values for training and validation, respectively 0.881 and 0.854), which both are superior to CT-RS (0.838 and 0.824, both *P* values < 0.001) and PET-RS (0.821 and 0.812, both *P* values < 0.001). The accuracy, precision, sensitivity and specificity were 0.796, 0.827, 0.782 and 0.812 for CT-RS model; 0.767, 0.782, 0.782 and 0.75 for PET-RS model; 0.806, 0.857, 0.764 and 0.854 for PET/CT-RS; 0.883, 0.891, 0.891 and 0.875 for PET/CT-RS incorporating clinical and metabolic parameters, respectively.

Construction and Validation of Radiomics Nomogram

Among all pathologic and therapeutic factors, SUVmax and pathologic LVI were demonstrated to be associated with survival prognosis, which was incorporated into the nomogram's construction (**Supplementary Tables 4–7**). Radiomics features for calculating PET/CT Rad-scores of OS and PFS and their importance and significance were displayed in **Tables 3**, **4**. For estimation of OS, the C-index of the NWR in the training set and test set were 0.88 and 0.84, respectively. The C-index of the NWOR in the training set and test set were 0.82 and 0.80, respectively. For estimation of PFS, the C-index of the NWR in the training set and test set were 0.88 and 0.84, respectively. The C-index of the NWOR in the training set and test set were 0.85 and 0.79, respectively. Diagnostic Performance of the NWR and NWOR in **Table 5** and **Figure 3**. The PET/CT-NWR and PET/CT-NOWR, the corresponding calibration curve, and the decision curve were displayed in **Figures 4**, **5**.

Survival Outcome

As of September 30, 2020, 148 populations had been successfully followed up regarding the OS and PFS. The overall death rate was 50.67% (75/148), and the overall progression rate was 50.67% (75/148). The median OS of all populations was 28.95 months (range, 1-87 months), particularly 16.5 months (range, 1-39 months) for the pathologic LVI-present patients, and 58.7 months (range, 26-87 months) for the pathologic LVI-absent patients. The median PFS of the patients was 17.7 months (range, 1-85 months), particularly 10.4 months (range, 1-26 months) for the pathologic LVI-present patients and 53.3 months (range, 9-85 months) for the pathologic LVI-absent patients. The multivariate Cox regression analysis that SUVmax and pathologic LVI were independent prognostic indicators of both OS [HR=1.210 (95% CI) and 3.814 (95% CI), *P*< 0.001] and PFS [HR=1.233 (95% CI) and 3.988 (95% CI), *P*< 0.001]. Survival curves are displayed in **Supplementary Figures 2–5**.

TABLE 1 | Baseline clinical characteristics of patients.

Clinical factors	LVI-absent	LVI-present	X^2/Z	*P*
Gender			0.3610	0.5479
Female	19 (27.9)	26 (32.5)		
Male	49 (72.1)	54 (67.5)		
Lymph node metastasis			23.1482	< 0.01
Negative	33 (48.5)	10 (12.5)		
Positive	35 (51.5)	70 (87.5)		
Tumor grade			35.6672	< 0.01
Well differentiated	7 (10.3)	1 (1.25)		
Middle differentiated	43 (63.2)	19 (23.8)		
Poorly differentiated	18 (26.5)	60 (75.0)		
Molecular subtype			4.2472	0.2360
Undifferentiated	11 (16.2)	24 (30.0)		
Diffuse type	21 (30.9)	23 (28.8)		
Mixed type	18 (26.5)	18 (22.5)		
Intestinal type	18 (26.5)	15 (18.8)		
T stage			6.4222	0.0928
T1	17 (25.4)	13 (16.3)		
T2	36 (53.7)	40 (50.0)		
T3	14 (20.9)	22 (27.5)		
T4	0 (0.0)	5 (6.25)		
N stage			85.4190	< 0.01
N0	33 (48.5)	6 (7.5)		
N1	29 (42.6)	6 (7.5)		
N2	4 (5.9)	38 (47.5)		
N3	2 (2.94)	30 (37.5)		
M stage			3.1613	0.0754
M0	38 (55.9)	56 (70.0)		
M1	30 (44.1)	24 (30.0)		
cTNM			6.3146	0.0973
I	24 (35.3)	18 (22.5)		
II	11 (16.2)	7 (8.8)		
III	3 (4.4)	5 (6.3)		
IV	30 (44.1)	50 (62.5)		
Age	62.43 ± 9.64	61.33 ± 10.35	0.67	0.5067
CEA	2.19 ± 3.07	20.67 ± 78.25	-1.93	0.0554
CA125	14.34 ± 43.34	20.53 ± 47.75	-0.82	0.4136
CA199	63.12 ± 65.73	126.62 ± 309.72	-1.65	0.1019
SUVmax	6.31 ± 2.25	9.20 ± 2.87	-6.71	< 0.01
Tumor thickness	1.61 ± 0.59	1.70 ± 0.56	-0.90	0.3701
TLG	65.63 ± 62.55	99.04 ± 55.19	-3.43	< 0.01
SUVmean	8.35 ± 4.97	9.32 ± 3.93	-1.32	0.1877
MTV	9.31 ± 5.72	8.99 ± 4.67	0.38	0.7037

SUVmax, maximum standardized uptake value; SUV, mean mean standardized uptake value; TLG, total lesion glycolysis; MTV, metabolic tumor volume; CEA, carcinoembryonic antigen; CA125, carbohydrate antigen 125; CA199, Carbohydrate antigen199; LVI, lymph vascular invasion.

Case Study

Two typical cases were chosen by the domain experts—one patient with features predicting LVI-absent status and one with LVI-present status—to illustrate the performance of our model in predicting LVI status and survival outcome. The detailed medical information, including the CT and PET images and fused images for each patient, are shown in **Supplementary Figures 6A, B**. A: Representative PET/CT images in a 60-year-old patient with stage I A gastric cancer, with evidence of LVI-absent status at postsurgical histological analysis after surgery. For predicted LVI-absent patient, OS and PFS were 47.4 and 28.9 months, respectively. B: Representative PET/CT images in a 68-year-old patient with stage II B gastric cancer, with evidence of LVI-present status at postsurgical histological analysis after surgery. For predicted LVI-present patient, OS and PFS were 16.2 and 8.7 months, respectively.

DISCUSSION

The aim of the present study was to evaluate the diagnostic performance of machine learning models built from a great number of clinicopathological parameters and PET-CT data for predicting pathological LVI status and survival outcomes in GC patients. Our experimental results demonstrated that the PET/CT-RS model incorporating tumor grade and SUVmax exhibited excellent clinical value, which achieved relatively higher AUCs than the PET/CT-RS model did, suggesting the additional value of clinico-pathological variables and metabolic parameters in the identification of LVI status in GC patients. Furthermore, SUVmax and pathologic LVI status were demonstrated to be independent predictors of both OS and PFS, which indicates that SUVmax can serve as a non-invasive bio-marker to facilitate individual treatment strategy schedules.

TABLE 2 | Diagnostic Performance of different radiomics models.

	CT-RS		PET-RS		PET/CT-RS		PET/CT-RS incorporating clinical and metabolic parameters	
	Training set	Test set	Training set	Test set	Training set	Test set	Training set	Test set
Accuracy	0.796	0.733	0.767	0.756	0.806	0.800	0.883	0.867
Precision	0.827	0.750	0.782	0.760	0.857	0.826	0.891	0.875
AUC	0.838	0.824	0.821	0.812	0.881	0.854	0.936	0.914
Sensitivity	0.782	0.750	0.782	0.792	0.764	0.792	0.891	0.875
Specificity	0.812	0.714	0.750	0.714	0.854	0.810	0.875	0.857
PPV	0.827	0.750	0.782	0.760	0.857	0.826	0.891	0.875
NPV	0.765	0.714	0.750	0.750	0.759	0.773	0.875	0.857

PPV indicates positive prediction value; NPV indicates negative prediction value.

Previous studies have investigated the potential of baseline metabolic indexes to predict tumor LVI. A previous study conducted by Hyun, SH et al. reported that tumor-to normal liver standardized uptake value ratio (TLR) of the tumor is closely associated with the occurrence of microvascular invasion (MVI) and constructed a predictive model for preoperative prediction of MVI status yielding an AUC of 0.756 (24). In our study, the conventional clinico-pathological indexes (such as age, gender, tumor markers, tumor grade, and so on) and PET metabolic parameters (SUVmax, SUVmean, TLG, and MTV) were analyzed, and only SUVmax and tumor grade were considered as independent LVI predictors, suggesting the traditional parameters extracted from conventional images demonstrate a limited contribution to LVI prediction.

Different from the naked eye discrimination of traditional imaging modality, radiomics analysis enables automatically

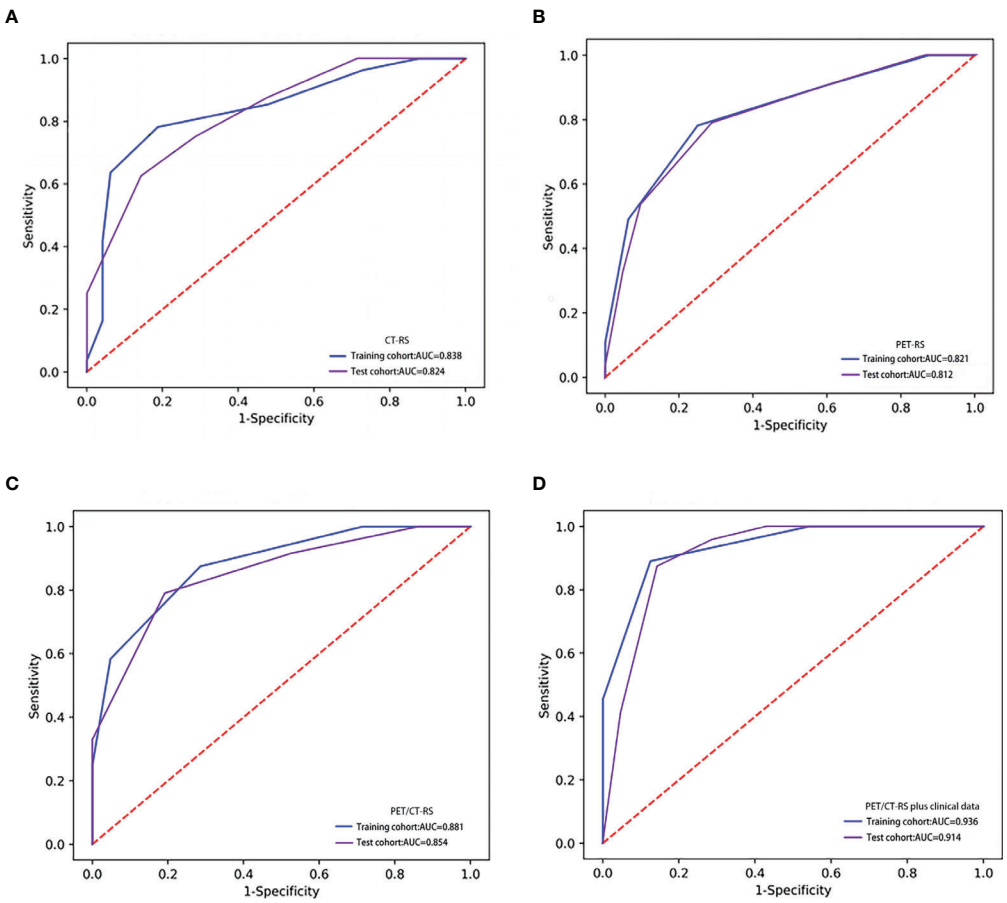

FIGURE 2 | ROCs of different radiomics models in the training and test set. **(A)** The ROC of CT-RS; **(B)** The ROC of PET-RS; **(C)** The ROC of PET/CT-RS; **(D)** The ROC of PET/CT-RS incorporating clinical and metabolic parameters.

TABLE 3 | Radiomics features for calculating PET/CT radiomics scores (Rad-scores) of OS and their importance.

Feature name	Importance
original_glszm_SizeZoneNonUniformityNormalized.PET	2.920620505
original_glszm_SmallAreaEmphasis.PET	6.308496129
wavelet.HLH_firstorder_Kurtosis.PET	0.275069109
log.sigma.3.0.mm.3D_ngtdm_Coarseness.PET	1.76E-06
wavelet.HHH_glcm_ClusterShade.PET	10.57007006
wavelet.HLL_glszm_LargeAreaHighGrayLevelEmphasis.PET	9.41E-10
wavelet.LHH_gldm_SmallDependenceEmphasis.CT	4.869217544
wavelet.LHH_glszm_SizeZoneNonUniformityNormalized.CT	-1.937417252
wavelet.LLH_glszm_LargeAreaLowGrayLevelEmphasis.CT	8.70E-06
wavelet.LLL_glcm_Imc1.CT	3.16013583

filtering comprehensive data from images and deeply investigating tumor heterogeneity. In a previous study, the clinical value of radiomics analysis in the prediction of pathological LVI or MVI has been explored. Zhang et al. reported that radiomics models based on magnetic resonance imaging (MRI) and CT could serve as an effective visual prognostic tool for predicting LVI in rectal cancer. It demonstrated the great potential of preoperative prediction to improve treatment decisions (25). Liu et al. explored the use of dynamic contrast-enhanced (DCE)-MRI-based radiomics for preoperative prediction of LVI in invasive breast cancer and found that the DCE-MRI-based radiomics signature in combination with MRI Axillary lymph node (ALN) status was effective in predicting the LVI status of patients with invasive breast cancer before surgery (26). To our best knowledge, we developed the first-of-its-kind machine learning models based on quantitative radiomics signatures derived from preoperative ^{18}F-FDG PET/CT images to predict LVI status in GC patients, which may serve as a potential biomarker to supplement the traditional clinical and imaging modalities for personalized treatment in GC patients. Our radiomics models demonstrated favorable predictive efficacy, with high AUCs in the training set and validation set. In the validation set, the prediction accuracy of the integrated model is 0.867, while the accuracy of the PET model and the CT model is 0.756 and 0.733, respectively, which demonstrated that the combined model achieved better predictive efficacy than either the PET-based radiomics signatures or the CT-based radiomics signatures alone. Additionally, with the inclusion of clinical indexes and metabolic parameters in the integrated radiomics model, the predictive performance was improved, suggesting that the clinical factors (tumor grade and lymph node metastasis) and metabolic parameters (SUVmax) played a complementary role in predicting LVI and ultimately contribute to improving the prediction efficacy of the integrated model (training set, validation set AUC are 0.936 and 0.914, respectively).

The current AJCC/UICC guidelines do not include LVI as an independent prognostic indicator of GC in the TNM staging system. However, many studies have shown that LVI is an important prognostic factor for GC after surgical treatment and is associated with tumor recurrence. Patients with LVI had been reported to be associated with poorer prognosis (27–29). Partly in line with previous works, we found that SUVmax and pathological LVI were independent predictors of the survival period, suggesting their clinical usefulness in the long-term management of GC patients. Therefore, in addition to establish a PET/CT-based radiomics signature for the prediction of LVI status, the predictive role of this signature in the survival outcome of GC patients was also explored in this study. Previous research has demonstrated that radiomics analysis can be applied to predict survival outcomes in patients with GC. Jiang et al. analyzed clinico-pathological variables and PET/CT-based radiomics features of 214 GC patients, and a radiomics nomogram with the radiomic signature incorporated was constructed to demonstrate the incremental value of the radiomic signature to the TNM staging system for individualized survival estimation (30).

Different from the previous works, we included LVI and SUVmax as stratifying indexes and explored the survival

TABLE 4 | Radiomics features for calculating PET/CT radiomics scores (Rad-scores) of PFS and their importance.

Feature name	Importance
log.sigma.3.0.mm.3D_firstorder_90Percentile.PET	9.70279E-05
original_gldm_LargeDependenceLowGrayLevelEmphasis.PET	3.578397243
original_glszm_SmallAreaEmphasis.PET	8.222186126
wavelet.LLH_ngtdm_Contrast.PET	5.71462E-05
log.sigma.3.0.mm.3D_glszm_SmallAreaLowGrayLevelEmphasis.CT	4.247335367
log.sigma.3.0.mm.3D_ngtdm_Coarseness.CT	2.4324E-06
wavelet.HHH_glcm_ClusterShade.CT	8.907641842
wavelet.HLL_glszm_SmallAreaLowGrayLevelEmphasis.CT	4.175090394
wavelet.LHH_glszm_SizeZoneNonUniformityNormalized.PET	-2.014521921
wavelet.LHL_glrlm_GrayLevelNonUniformityNormalized.CT	1.824925527
wavelet.LLL_glcm_Imc1.CT	5.26516043

TABLE 5 | Diagnostic Performance of the NWR and NWOR.

Model	OS				PFS			
	Training set		Test set		Training set		Test set	
	c-index	95%CI	c-index	95%CI	c-index	95%CI	c-index	95%CI
NWR	0.88	0.84-0.91	0.84	0.80-0.89	0.88	0.84-0.91	0.84	0.80-0.89
NWOR	0.82	0.77-0.86	0.80	0.75-0.86	0.85	0.81-0.88	0.79	0.73-0.80

outcome prediction value of the clinical nomogram. We also provided clinicians an easy-to-use approach to predict survival outcomes by developing a radiomics nomogram that demonstrated favorable discrimination in both the training and testing sets. Additionally, we found an integrated nomogram incorporated PET/CT radiomics and clinical parameters improved survival prediction in GC patients. For estimation of PFS, the c-index of the integrated nomogram is 0.84 in the test set, while the c-index of the clinical parameters-based nomogram is 0.79.

There are some limitations to this study. Firstly, although the final results achieved are ideal, the number of patients included was still limited. A future study with a larger number of samples will be needed to conduct further verification of our results. Secondly, potential selection bias might exist because of the retrospective nature. Therefore, a prospective validation might provide sufficient evidence for clinical application. Thirdly, as tumor segmentation was performed in a manual manner, the exploitation of a more efficient method for tumor segmentation remains an important consideration.

CONCLUSION

In summary, this study demonstrated that the application of radiomics analysis based on PET/CT images shows the potential

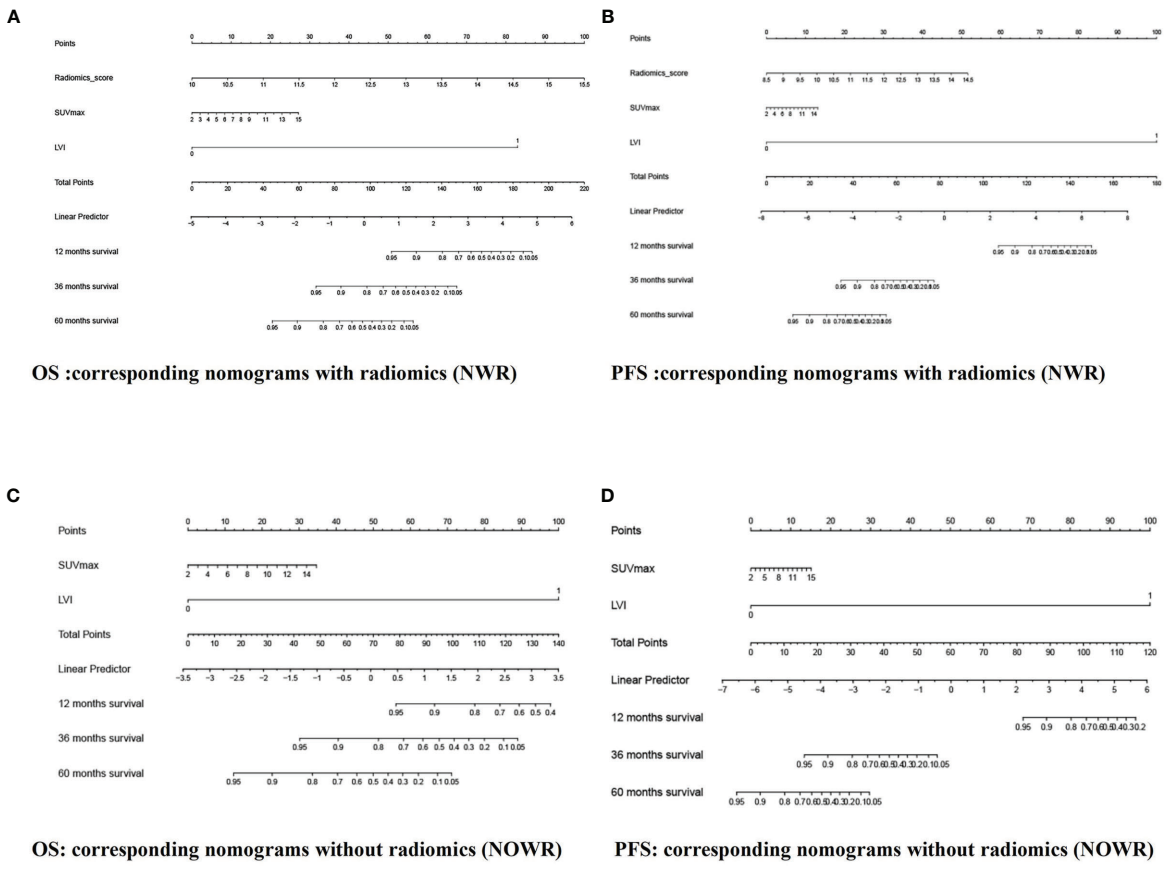

FIGURE 3 | The NWR for OS **(A)** and PFS **(B)** prediction based on rad-score and clinical factors (LVI, SUVmax). The NWOR for OS **(C)** and PFS **(D)** prediction based on clinical factors (LVI, SUVmax).

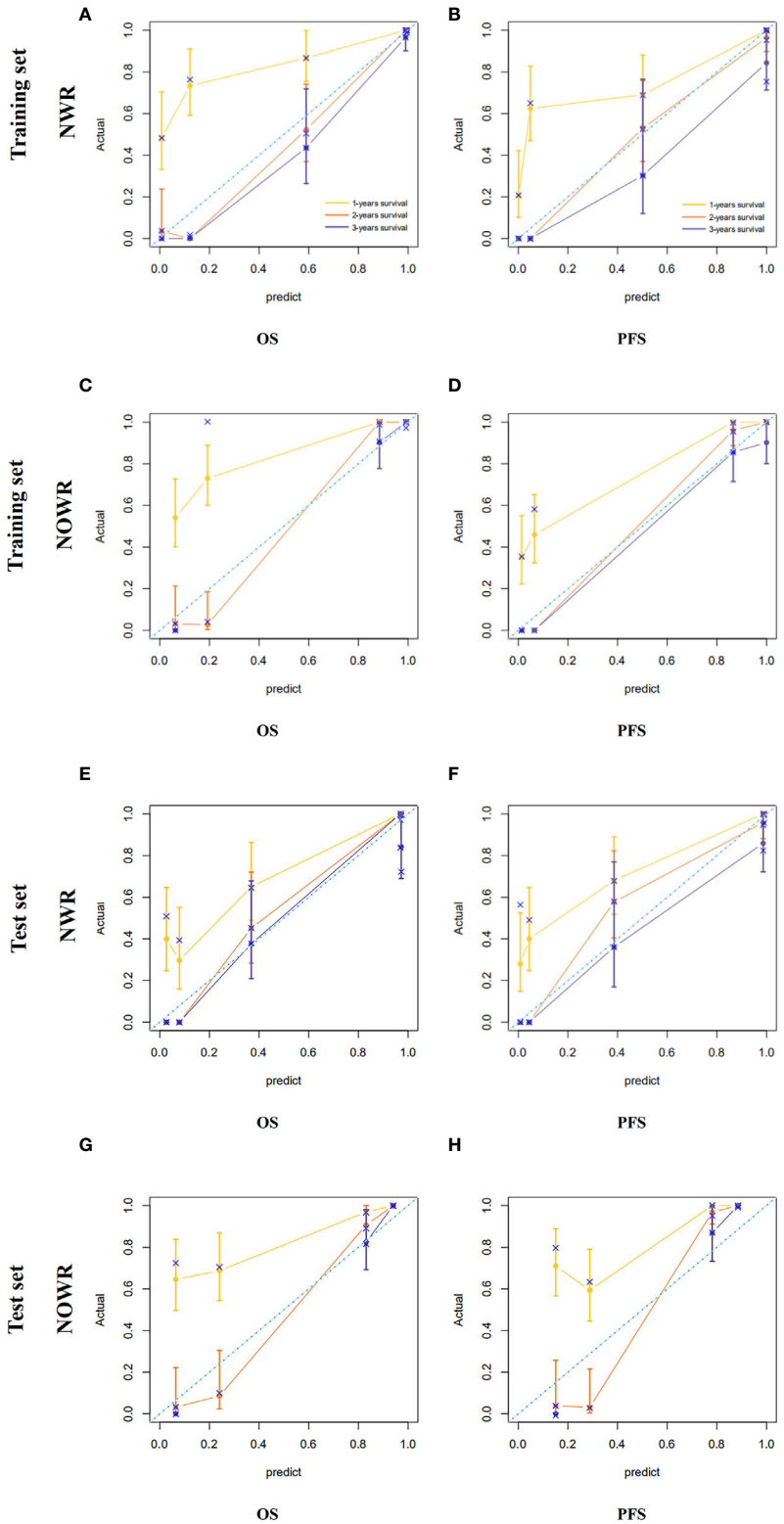

FIGURE 4 | Calibration curve of the NWR for OS **(A)** and PFS **(B)** in the training set. Calibration curve of the NOWR for OS **(C)** and PFS **(D)** in the training set. Calibration curve of the NWR for OS **(E)** and PFS **(F)** in the test set. Calibration curve of the NOWR for OS **(G)** and PFS **(H)** in the test set.

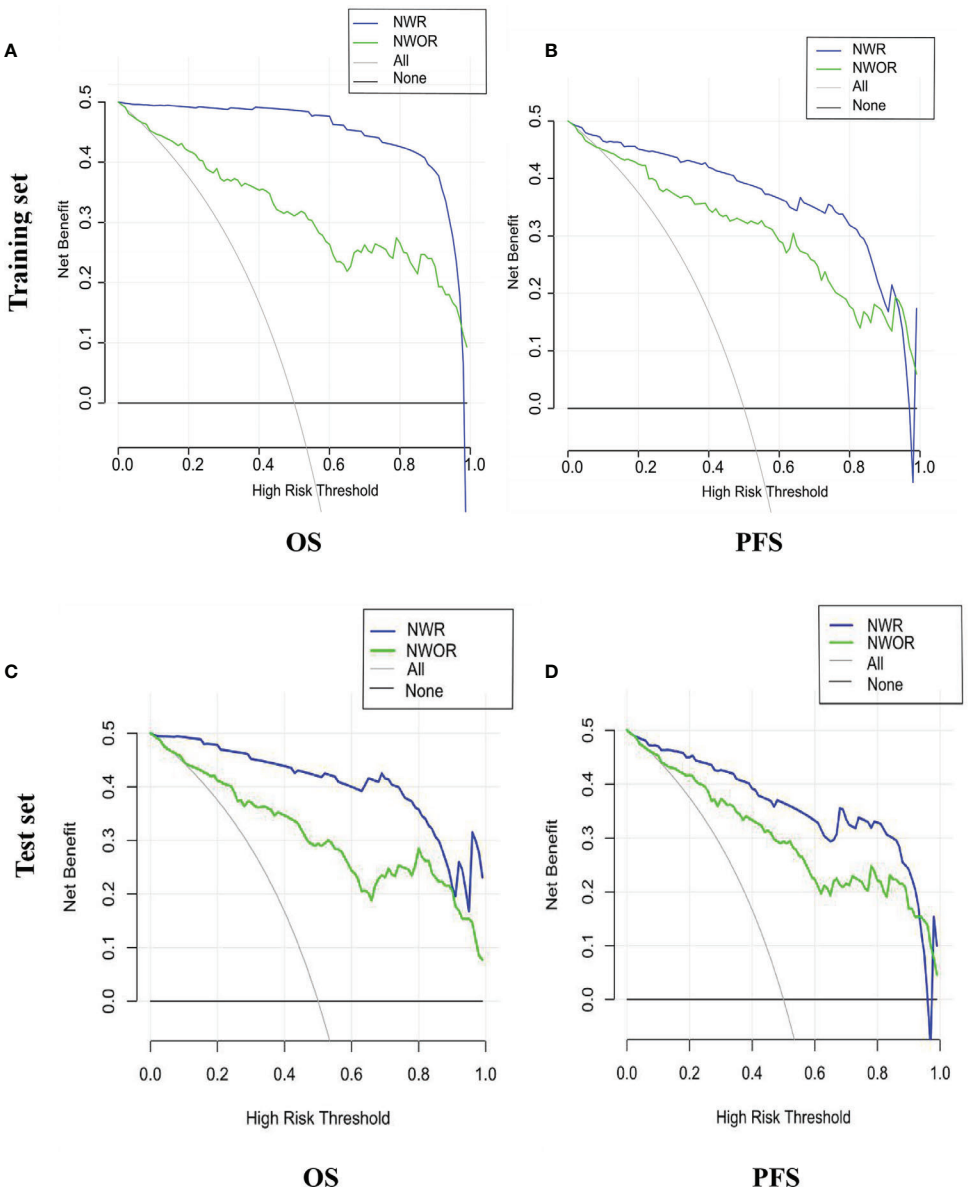

FIGURE 5 | Decision curve of the nomograms for OS **(A)** and PFS **(B)** in the training set. Decision curve of the nomograms for OS **(C)** and PFS **(D)** in the test set.

role of preoperative assessment of LVI status. In addition, we developed an easy-to-use tool to predict the survival outcome of patients with GC. Although further investigation, including a much larger number of populations from multicenter, should be carried out to better expand the generalization ability of this method.

DATA AVAILABILITY STATEMENT

The raw data supporting the conclusions of this article will be made available by the authors, without undue reservation.

ETHICS STATEMENT

The studies involving human participants were reviewed and approved by Harbin Medical University Cancer Hospital. The ethics committee waived the requirement of written informed consent for participation.

AUTHOR CONTRIBUTIONS

Conception and design: LY and WC. Collection and assembly of the data: PX. Development of the methodology: ML. Data

analysis and interpretation: MW and MP. Manuscript writing: All authors. Manuscript review: LZ and KW. All authors contributed to the article and approved the submitted version.

FUNDING

This paper is supported by the National Natural Science Foundation of China General Projects (81571740), Provincial Key Research and Development Program of Heilongjiang Province (GA21C001), Postdoctoral Special Scientific Research Grant of Heilongjiang Provincial Government (LBH-Q17104), Distinguished Young Scientist Funding of Harbin Medical University Affiliated Tumor Hospital (JCQN2019-02), Key Project of the Climbing Funding of the National Cancer Center (NCC201808B019), Haiyan Funding of Harbin Medical University Cancer Hospital (JJQN2019-23). The funders had no role in study design, data collection and analysis, decision to publish, or preparation of the manuscript.

SUPPLEMENTARY MATERIAL

The Supplementary Material for this article can be found online at: https://www.frontiersin.org/articles/10.3389/fonc.2022.836098/full#supplementary-material

REFERENCES

1. Ferlay J, Colombet M, Soerjomataram I, Mathers C, Parkin DM, Piñeros M, et al. Estimating the Global Cancer Incidence and Mortality in 2018: GLOBOCAN Sources and Methods. *Int J Cancer* (2019) 144(8):1941–53. doi: 10.1002/ijc.31937
2. Songun I, Putter H, Kranenbarg EM, Sasako M, van de Velde CJ. Surgical Treatment of Gastric Cancer: 15-Year Follow-Up Results of the Randomised Nationwide Dutch D1D2 Trial. *Lancet Oncol* (2010) 11(5):439–49. doi: 10.1016/s1470-2045(10)70070-x
3. Yu J, Huang C, Sun Y, Su X, Cao H, Hu J, et al. Effect of Laparoscopic vs Open Distal Gastrectomy on 3-Year Disease-Free Survival in Patients With Locally Advanced Gastric Cancer: The CLASS-01 Randomized Clinical Trial. *Jama* (2019) 321(20):1983–92. doi: 10.1001/jama.2019.5359
4. Cunningham D, Starling N, Rao S, Iveson T, Nicolson M, Coxon F, et al. Capecitabine and Oxaliplatin for Advanced Esophagogastric Cancer. *N Engl J Med* (2008) 358(1):36–46. doi: 10.1056/NEJMoa073149
5. Werntz RP, Smith ZL, Packiam VT, Smith N, Steinberg GD. The Impact of Lymphovascular Invasion on Risk of Upstaging and Lymph Node Metastasis at the Time of Radical Cystectomy. *Eur Urol Focus* (2020) 6(2):292–7. doi: 10.1016/j.euf.2018.09.019
6. Takahashi H, Katsuta E, Yan L, Tokumaru Y, Katz MHG, Takabe K. Transcriptomic Profile of Lymphovascular Invasion, a Known Risk Factor of Pancreatic Ductal Adenocarcinoma Metastasis. *Cancers (Basel)* (2020) 12 (8):2033.s. doi: 10.3390/cancers12082033
7. Sonbul SN, Aleskandarany MA, Kurozumi S, Joseph C, Toss MS, Diez-Rodriguez M, et al. Saccharomyces Cerevisiae-Like 1 (SEC14L1) Is a Prognostic Factor in Breast Cancer Associated With Lymphovascular Invasion. *Mod Pathol* (2018) 31(11):1675–82. doi: 10.1038/s41379-018-0092-9
8. Ragage F, Debled M, MacGrogan G, Brouste V, Desrousseaux M, Soubeyran I, et al. Is It Useful to Detect Lymphovascular Invasion in Lymph Node-Positive Patients With Primary Operable Breast Cancer? *Cancer* (2010) 116(13):3093–101. doi: 10.1002/cncr.25137
9. Li P, He HQ, Zhu CM, Ling YH, Hu WM, Zhang XK, et al. The Prognostic Significance of Lymphovascular Invasion in Patients With Resectable Gastric Cancer: A Large Retrospective Study From Southern China. *BMC Cancer* (2015) 15:370. doi: 10.1186/s12885-015-1370-2
10. Araki I, Hosoda K, Yamashita K, Katada N, Sakuramoto S, Moriya H, et al. Prognostic Impact of Venous Invasion in Stage IB Node-Negative Gastric Cancer. *Gastric Cancer* (2015) 18(2):297–305. doi: 10.1007/s10120-014-0362-2
11. Fujikawa H, Koumori K, Watanabe H, Kano K, Shimoda Y, Aoyama T, et al. The Clinical Significance of Lymphovascular Invasion in Gastric Cancer. *In Vivo* (2020) 34(3):1533–9. doi: 10.21873/invivo.11942
12. Wu L, Liang Y, Zhang C, Wang X, Ding X, Huang C, et al. Prognostic Significance of Lymphovascular Infiltration in Overall Survival of Gastric Cancer Patients After Surgery With Curative Intent. *Chin J Cancer Res* (2019) 31(5):785–96. doi: 10.21147/j.issn.1000-9604.2019.05.08
13. Lin CY, Liao CW, Chu LY, Yen KY, Jeng LB, Hsu CN, et al. Predictive Value of 18F-FDG PET/CT for Vascular Invasion in Patients With Hepatocellular Carcinoma Before Liver Transplantation. *Clin Nucl Med* (2017) 42(4):e183–7. doi: 10.1097/rlu.0000000000001545
14. Noda Y, Goshima S, Kanematsu M, Watanabe H, Kawada H, Kawai N, et al. F-18 FDG Uptake on Positron Emission Tomography as a Predictor for Lymphovascular Invasion in Patients With Lung Adenocarcinoma. *Ann Nucl Med* (2016) 30(1):11–7. doi: 10.1007/s12149-015-1023-1
15. Gillies RJ, Kinahan PE, Hricak H. Radiomics: Images Are More Than Pictures, They Are Data. *Radiology* (2016) 278(2):563–77. doi: 10.1148/radiol.2015151169
16. Sollini M, Antunovic L, Chiti A, Kirienko M. Towards Clinical Application of Image Mining: A Systematic Review on Artificial Intelligence and Radiomics. *Eur J Nucl Med Mol Imaging* (2019) 46(13):2656–72. doi: 10.1007/s00259-019-04372-x
17. Xu C, Yu Y, Li X, Sun H. Value of Integrated PET-IVIM MRI in Predicting Lymphovascular Space Invasion in Cervical Cancer Without Lymphatic Metastasis. *Eur J Nucl Med Mol Imaging* (2021) 48(9):2990–3000. doi: 10.1007/s00259-021-05208-3
18. Nie P, Yang G, Wang N, Yan L, Miao W, Duan Y, et al. Additional Value of Metabolic Parameters to PET/CT-Based Radiomics Nomogram in Predicting Lymphovascular Invasion and Outcome in Lung Adenocarcinoma. *Eur J Nucl Med Mol Imaging* (2021) 48(1):217–30. doi: 10.1007/s00259-020-04747-5
19. Chen X, Yang Z, Yang J, Liao Y, Pang P, Fan W, et al. Radiomics Analysis of Contrast-Enhanced CT Predicts Lymphovascular Invasion and Disease Outcome in Gastric Cancer: A Preliminary Study. *Cancer Imaging* (2020) 20(1):24. doi: 10.1186/s40644-020-00302-5
20. Meng L, Dong D, Chen X, Fang M, Wang R, Li J, et al. 2D and 3D CT Radiomic Features Performance Comparison in Characterization of Gastric Cancer: A Multi-Center Study. *IEEE J BioMed Health Inform* (2021) 25 (3):755–63. doi: 10.1109/jbhi.2020.3002805
21. Matti A, Lima GM, Pettinato C, Pietrobon F, Martinelli F, Fanti S. How Do the More Recent Reconstruction Algorithms Affect the Interpretation Criteria of PET/CT Images? *Nucl Med Mol Imaging* (2019) 53(3):216–22. doi: 10.1007/s13139-019-00594-x
22. van Griethuysen JJM, Fedorov A, Parmar C, Hosny A, Aucoin N, Narayan V, et al. Computational Radiomics System to Decode the Radiographic Phenotype. *Cancer Res* (2017) 77(21):e104–7. doi: 10.1158/0008-5472.Can-17-0339
23. Zwanenburg A, Vallières M, Abdalah MA, Aerts H, Andrearczyk V, Apte A, et al. The Image Biomarker Standardization Initiative: Standardized Quantitative Radiomics for High-Throughput Image-Based Phenotyping. *Radiology* (2020) 295(2):328–38. doi: 10.1148/radiol.2020191145
24. Hyun SH, Eo JS, Song BI, Lee JW, Na SJ, Hong IK, et al. Preoperative Prediction of Microvascular Invasion of Hepatocellular Carcinoma Using (18) F-FDG PET/CT: A Multicenter Retrospective Cohort Study. *Eur J Nucl Med Mol Imaging* (2018) 45(5):720–6. doi: 10.1007/s00259-017-3880-4
25. Zhang Y, He K, Guo Y, Liu X, Yang Q, Zhang C, et al. A Novel Multimodal Radiomics Model for Preoperative Prediction of Lymphovascular Invasion in Rectal Cancer. *Front Oncol* (2020) 10:457:457. doi: 10.3389/fonc.2020.00457
26. Liu Z, Feng B, Li C, Chen Y, Chen Q, Li X, et al. Preoperative Prediction of Lymphovascular Invasion in Invasive Breast Cancer With Dynamic Contrast-

Enhanced-MRI-Based Radiomics. *J Magn Reson Imaging* (2019) 50(3):847–57. doi: 10.1002/jmri.26688
27. Liu S, Liu S, Ji C, Zheng H, Pan X, Zhang Y, et al. Application of CT Texture Analysis in Predicting Histopathological Characteristics of Gastric Cancers. *Eur Radiol* (2017) 27(12):4951–9. doi: 10.1007/s00330-017-4881-1
28. Montagnani F, Crivelli F, Aprile G, Vivaldi C, Pecora I, De Vivo R, et al. Long-Term Survival After Liver Metastasectomy in Gastric Cancer: Systematic Review and Meta-Analysis of Prognostic Factors. *Cancer Treat Rev* (2018) 69:11–20. doi: 10.1016/j.ctrv.2018.05.010
29. Nishibeppu K, Komatsu S, Ichikawa D, Imamura T, Kosuga T, Okamoto K, et al. Venous Invasion as a Risk Factor for Recurrence After Gastrectomy Followed by Chemotherapy for Stage III Gastric Cancer. *BMC Cancer* (2018) 18(1):108. doi: 10.1186/s12885-018-4052-z
30. Jiang Y, Yuan Q, Lv W, Xi S, Huang W, Sun Z, et al. Radiomic Signature of (18)F Fluorodeoxyglucose PET/CT for Prediction of Gastric Cancer Survival and Chemotherapeutic Benefits. *Theranostics* (2018) 8(21):5915–28. doi: 10.7150/thno.28018

Conflict of Interest: The authors declare that the research was conducted in the absence of any commercial or financial relationships that could be construed as a potential conflict of interest.

GLOSSARY

LVI	lymph vascular invasion
GC	gastric cancer
2D	two-dimensional
3D	three-dimensional
RSs	radiomics signatures
VOI	volume of interests
Rad-scores	radiomics score
NWR	nomograms with radiomics
NWOR	nomograms without radiomics
SUVmax	maximum standardized uptake value
H&E	hematoxylin and eosin
SUVmean	mean standardized uptake values
^{18}F-FDG PET-CT	^{18}F-fluorodeoxyglucose positron emission tomography-computed tomography
TLG	total lesion glycolysis
CEA	carcinoembryonic antigen
CA125	carbohydrate antigen 125
CA199	carbohydrate antigen 199
MTV	metabolic tumor volume
ROI	region of interest
ICCs	Intra- and inter-class correlation coefficients
KNN	k-Nearest Neighbor (KNN)
Rad-scores	radiomics score
DCA	Decision curve analysis
ROC	receiver operating curve
AUC	area under the curve
TLR	tumor-to normal liver standardized uptake value ratio
MRI	magnetic resonance imaging
CT	computed tomography
DCE	dynamic contrast-enhanced
ALN	Axillary lymph node
MVI	microvascular invasion
LVSI	lymph vascular space invasion
OS	overall survival
PFS	progression-free survival
DFS	disease-free survival
CECT	contrast-enhanced computed tomography

frontiers | Frontiers in Oncology

TYPE Original Research
PUBLISHED 16 September 2022
DOI 10.3389/fonc.2022.883109

OPEN ACCESS

EDITED BY
Bo Zhang,
Sichuan University, China

REVIEWED BY
Nguyen Minh Duc,
Pham Ngoc Thach University of Medicine, Vietnam
Leila Mostafavi,
Harvard Medical School, United States
Jiong Ni,
Tongji University, China
Majidreza Mohebpour,
McGill University Health Centre, Canada
Bogdan Silviu Ungureanu,
University of Medicine and Pharmacy of Craiova, Romania

*CORRESPONDENCE
Zhengrong Li
lzr13@foxmail.com
Yi Cao
doctorcaoyi@126.com

†These authors have contributed equally to this work and share first authorship

SPECIALTY SECTION
This article was submitted to Gastrointestinal Cancers: Gastric and Esophageal Cancers, a section of the journal Frontiers in Oncology

RECEIVED 24 February 2022
ACCEPTED 29 August 2022
PUBLISHED 16 September 2022

CITATION
Zeng Q, Zhu Y, Li L, Feng Z, Shu X, Wu A, Luo L, Cao Y, Tu Y, Xiong J, Zhou F and Li Z (2022) CT-based radiomic nomogram for preoperative prediction of DNA mismatch repair deficiency in gastric cancer. *Front. Oncol.* 12:883109. doi: 10.3389/fonc.2022.883109

CT-based radiomic nomogram for preoperative prediction of DNA mismatch repair deficiency in gastric cancer

Qingwen Zeng[1,2†], Yanyan Zhu[3†], Leyan Li[4], Zongfeng Feng[1,2], Xufeng Shu[1], Ahao Wu[1], Lianghua Luo[1], Yi Cao[1*], Yi Tu[5], Jianbo Xiong[1], Fuqing Zhou[3] and Zhengrong Li[1,2*]

[1]Department of Gastrointestinal Surgery, The First Affiliated Hospital, Nanchang University, Nanchang, China, [2]Institute of Digestive Surgery, The First Affiliated Hospital of Nanchang University, Nanchang, China, [3]Department of Radiology, The First Affiliated Hospital, Nanchang University, Nanchang, China, [4]Jiangxi Medical College, Nanchang University, Nanchang, China, [5]Department of Pathology, The First Affiliated Hospital of Nanchang University, Nanchang, China

Background: DNA mismatch repair (MMR) deficiency has attracted considerable attention as a predictor of the immunotherapy efficacy of solid tumors, including gastric cancer. We aimed to develop and validate a computed tomography (CT)-based radiomic nomogram for the preoperative prediction of MMR deficiency in gastric cancer (GC).

Methods: In this retrospective analysis, 225 and 91 GC patients from two distinct hospital cohorts were included. Cohort 1 was randomly divided into a training cohort (n = 176) and an internal validation cohort (n = 76), whereas cohort 2 was considered an external validation cohort. Based on repeatable radiomic features, a radiomic signature was constructed using the least absolute shrinkage and selection operator (LASSO) regression analysis. We employed multivariable logistic regression analysis to build a radiomics-based model based on radiomic features and preoperative clinical characteristics. Furthermore, this prediction model was presented as a radiomic nomogram, which was evaluated in the training, internal validation, and external validation cohorts.

Results: The radiomic signature composed of 15 robust features showed a significant association with MMR protein status in the training, internal validation, and external validation cohorts (both *P*-values <0.001). A radiomic nomogram incorporating a radiomic signature and two clinical characteristics (age and CT-reported N stage) represented good discrimination in the training cohort with an AUC of 0.902 (95% CI: 0.853–0.951), in the internal validation cohort with an AUC of 0.972 (95% CI: 0.945–1.000) and in the external validation cohort with an AUC of 0.891 (95% CI: 0.825–0.958).

Conclusion: The CT-based radiomic nomogram showed good performance for preoperative prediction of MMR protein status in GC. Furthermore, this model was a noninvasive tool to predict MMR protein status and guide neoadjuvant therapy.

KEYWORDS

gastric cancer (GC), radiomics, microsatellite instability, nomogram, LASSO, DNA mismatch repair deficiency

Introduction

Gastric cancer (GC) is one of the most common malignant diseases and ranks as the fourth leading cause of cancer-related death worldwide (1). According to 2020 statistics, the incidence and mortality of GC both ranked third among solid tumors in China (1). The first diagnosis of GC patients with locally advanced disease is approximately two-thirds, so most guidelines recommend comprehensive therapy as the standard treatment method, mainly including neoadjuvant therapy plus surgery (2, 3). Kim et al. found that GC patients with cStage III disease with microsatellite instability-high (MSI-H) had better survival than those with microsatellite stability (MSS) after neoadjuvant chemotherapy (4). A meta-analysis of four randomized clinical trials of adjuvant chemotherapy based on immunotherapy in GC showed that the overall survival of GC patients with microsatellite instability (MSI) was significantly better than that of patients with MSS (hazard ratio [HR], 0.69; 95% CI, 0.55 to 0.88; P = 0.003) (5). However, An et al. showed that in MSI-H patients with stage II or III GC, adjuvant chemotherapy based on 5-FU did not receive any benefit, which gives a guideline that these patients are not suitable for the 5-FU-based chemotherapy drugs (6). MSI is caused by a lack of DNA mismatch repair protein deficiency (dMMR), which accounts for 6%–25% of GC patients (7). Interestingly, MSI creates a high mutation burden, increases the number of neoantigens in tumor tissues, and these individuals exhibit high levels of immune checkpoint molecules (8, 9). As a result, comprehensive therapy based on anti-PD-1/-L1 Abs may be a good option for MSI GC patients. Thus, assessing the MMR status of all GC patients is a level I recommendation in the current guidelines.

In clinical practice, immunohistochemistry (IHC) or DNA detection is the primary technology to evaluate MSI using postoperative tumor tissues. Although preoperative gastroscopy tumor samples could also be used to detect MSI, sampling bias and poor DNA quality may lead to misleading findings (10, 11). Thus, there is insufficient evidence to choose an appropriate neoadjuvant therapy for patients who are suffering from locally advanced GC. Furthermore, gastroscopic biopsy is a procedure that requires good physical condition for the patient, but it cannot be conducted on patients who have inadequate circumstances, including poor coagulation, cardiopulmonary dysfunction, and unacceptable gastroscopy. In some primary hospitals, there is difficulty in implementing these technologies. Therefore, developing a relatively non-invasion and acceptable strategy for detecting the MMR status of GC patients is an urgent task (12).

In comparison to gastroscopic biopsy and surgery without invasive injury, computed tomography (CT) is a noninvasive technology commonly used for the diagnosis, response evaluation, and postoperative follow-up of gastric cancer (13). Prior studies have demonstrated that quantitative radiomic features of CT images are associated with elements of the tumor microenvironment, such as the tumor stroma, gene expression level, and even tumor-infiltrating lymphocytes (11, 14, 15). Referring to the immunohistochemistry scores for α-smooth muscle actin and periostin, Yuming et al. built a deep-learning model to precisely assess tumor stroma using CT images in GC, which can guide treatment decisions and predict prognosis for patients (11). Human epidermal growth factor receptor 2 (HER2) status may be accurately predicted using a radiomic nomogram that combines a radiomic signature and carcinoembryonic antigen level (CEA) (16). Currently, Okihide et al. utilized five clinicopathological features (age, sex, location, T stage, and distant metastasis) to predict MSI (AUC = 0.82, 95% CI: 0.75–0.87) in GC. However, the main collecting clinicopathological features are derived from postoperative gastrectomy (17). As can be observed, predicting MMR status of GC patients based on clinicopathological features falls well short of clinical diagnostic standards. Furthermore, MSI was associated with tumor location, size and lymph node status in GC CT images (18). According to the above results, constructing a prediction model based on radiomic features may produce the desired result for the MSI diagnosis.

Although model-based radiomic features perform well in the identification of MMR deficiency in colorectal cancer (8, 19), this is the first study to employ radiomic features to predict MMR

status in GC. This study aimed to develop and validate a CT-based radiomic nomogram for the preoperative prediction of MMR deficiency in GC.

Materials and methods

Patients

This retrospective study was approved by the Ethics Committee of the First Affiliated Hospital of Nanchang University and the patients. Cohort 1 included 252 GC patients who underwent radical gastrectomy were enrolled in this study with preoperative contrast-enhanced CT examination from June 2018 to December 2021 at the First Affiliated Hospital of Nanchang University (Donghu Hospital). Another cohort 2 collected 91 GC patients from April 2020 to December 2021 at the First Affiliated Hospital of Nanchang University (Xianghu Hospital). The inclusion criteria were as follows (1): histologically proven diagnosis of GC; (2) preoperative contrast-enhanced CT within a month; (3) MMR protein status tested by IHC; and (4) no preoperative adjuvant therapy. The exclusion criteria were as follows: (1) any preoperative adjuvant therapy; (2) poor quality CT images: poor filling of the stomach with unsatisfactory gastric distention and substantial motion artifacts; and (3) lack of clinical data. Cohort 1 was randomly divided into the training (n = 176) and internal validation (n = 76) cohorts at a rate of 7:3 (Figure 1). The training cohort contained proficient DNA mismatch repair (pMMR, n = 105) and dMMR (n = 71). The internal validation cohort contained pMMRs (n = 46) and dMMRs (n = 30). Cohort 2 was used as an external validation cohort, which contained pMMR (n = 64) and dMMR (n = 27).

The collected preoperative clinical characteristics of the patients included age, body mass index (BMI), sex, tumor location, CEA status (normal or abnormal), CA19-9 status (normal or abnormal), CA12-5 status (normal or abnormal), AFP status (normal or abnormal), and CT-reported T stage (T1, T2, T3, T4) and N stage (N0, Nx). The normal range of CEA, CA19-9, CA12-5, and AFP was, respectively, 0–6.5 ng/ml, 0–27 U/ml, 0–35 U/ml, and 0–7 ng/ml. Additionally, we measured several semantic features to compare the difference in predictive level with radiomic features, including long diameters of the tumor, short diameters of the tumor, tumor thickness, and CT value of the tumor in the portal phase. The reference for CT imaging classification of gastric cancer was based on the Chinese Society of Clinical Oncology (CSCO): Clinical guidelines for the diagnosis and treatment of gastric cancer, 2021 (20). Reference for CT imaging classification of gastric cancer can be referred to Supplementary Figure 1.

MMR protein status evaluation

To determine MMR protein status, we employed IHC to test four correlated proteins, including mutL homolog 1 (MLH1), mutS homolog 2 (MSH2), mutS homolog 6 (MSH6) and mismatch repair system component (PMS2). According to MSI status, GC patients were divided into three groups: MSI-H, MSI-L, and MSI stability (MSS). The expression level of

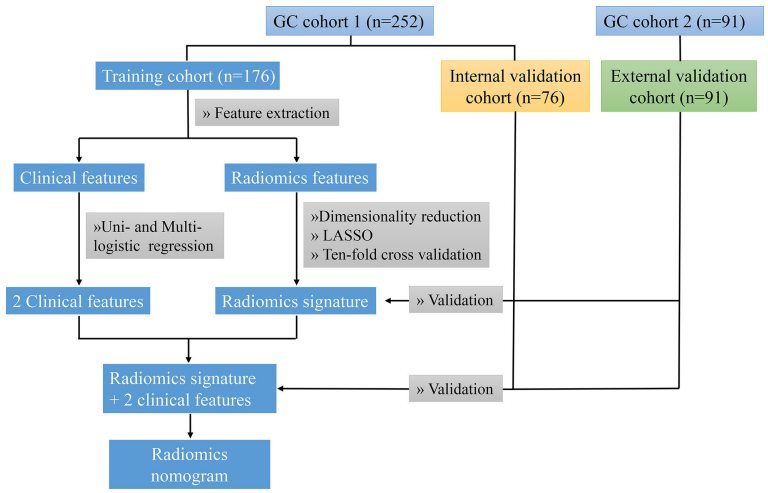

FIGURE 1
The technology roadmap represents workflow in this study. The GC cohort 1 was collected from the First Affiliated Hospital of Nanchang University (Donghu hospital), and the cohort 2 was collected from the First Affiliated Hospital of Nanchang University (Xianghu hospital).

MMR proteins was used to diagnose MSI status. The positive staining of all four proteins represented MSS/MSI-L (pMMR), but the MMR proteins with anyone assessed as negative represented MSI-H (dMMR) (21).

CT image acquisition

Before abdominal contrast-enhanced CT, all patients received Racanisodamine Hydrochloride injection 20 mg *via* intramuscular injection and drank 1,000–2,000 ml of water. The picture archiving and communication system (Carestream, Canada) was used to export CT images of the portal venous phase. Contrast-enhanced CT scanning of cohort 1 was performed using a 192-channel CT (Siemens Healthcare) in Donghu hospital. Cohort 2 was scanned by 256-channel CT (Siemens Healthcare) and 320-channel CT (Aquilion ONE) in Xianghu hospital. The acquisition parameters were as follows: tube voltage of 80 to 120 kVp; tube current of 120–300 mAs; the pitch of 0.6 to 1.25 mm; an image matrix of 512 × 512; and reconstruction slice thickness of 1 or 2 mm. After intravenous injection of contrast media (1.5 ml/kg, at a rate of 2.5–3.5 ml/s), the arterial phase and portal venous phase were acquired within 25–30 s and 65–70 s, respectively.

Radiomic features extraction

The extent of the tumor lesion was enhanced and more easily distinguished between the tumor and peripheral normal tissue during the portal venous phase, and many previous studies used this phase to segment tumor lesions (22, 23). In this study, we employed ITK-SANP software (version 3.6.0, USA) to manually segment regions of interest (ROIs) (Figure 2). Lesions were located by significantly enhanced parts and thickening of the gastric wall for incorporation with the clinical characteristics of pathology specimens (24). The ROIs were manually drawn carefully to highlight neighboring upper and lower slices of the solid tumor, while we were careful to avoid involving the normal gastric wall and nearby air or fluid (8). Radiologist 1 (Zhu with 5 years of experience) delineated the ROI of all 343 GC patients. We randomly selected 30 patients, re-drew their ROIs for feature extraction by Zhu one month later, and analyzed the result to prevent intraobserver differences from affecting the reproducibility of radiomic features. To confirm the interobserver reproducibility, a second radiologist (Zhou, who has 10 years of experience) delineated the ROIs for these 30 patients (16). Radiomic features were extracted using PyRadiomics software (version 2.2.0) (25). Finally, eight hundred and fifty-one radiomic features were extracted and classified into four categories: shape, size, texture, and wavelet (Supplementary Table S1).

Radiomic feature selection and radiomic signature establishment

Intra- and interclass correlation coefficients (ICCs) were used to evaluate the reproducibility and robustness of the extracted radiomic features. Only radiomic features with an ICC ≥0.8 were considered highly stable and retained for subsequent analysis. A Z-score normalization was used to standardize the radiomic feature data in the training, internal validation, and external validation cohorts. Then, we employed the Mann–Whitney U test to identify significantly different features between the pMMR and dMMR groups, with $P < 0.05$ in the training cohort (15). The least absolute shrinkage and selection operator (LASSO) regression was used for feature

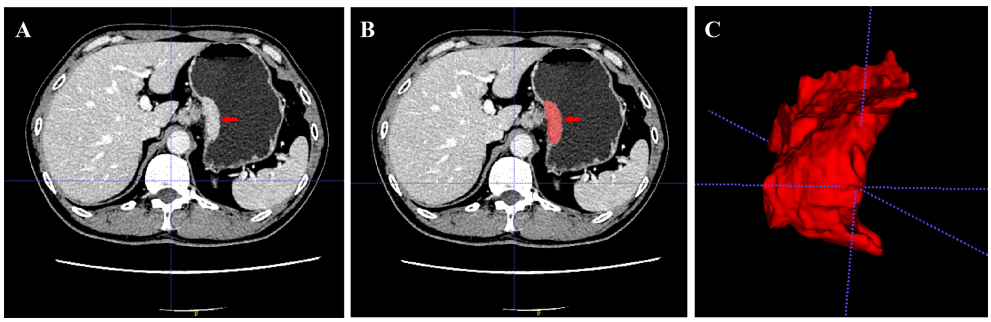

FIGURE 2
Manual segmentation of tumor with a GC patient. **(A)** A slice portal venous phase of contrast-enhanced CT images of the tumor. **(B)** the red label masks a slice CT image of the tumor with manual segmentation. **(C)** Three-dimensional (3D) image of the tumor with manual segmentation.

selection and radiomic signature construction in the training cohort. We used 10 cross-validations to define the regularization parameter λ. Finally, the radiomic score (Rad-score) was developed and demonstrated as a formula that was calculated by determining a linear combination of the selected features and the product of their respective coefficients. The R software package "Glmnet" was used for LASSO logistic regression.

The discriminative ability of the radiomic signature for predicting MMR deficiency was based on the receiver operating characteristic (ROC) curve and the area under the curve (AUC).

Establishment of the radiomic nomogram

A univariate logistic regression analysis was used to investigate the correlation between MMR deficiency and clinical characteristics in cohort 1 GC patients. Multivariate logistic regression analysis was used to build a prediction model by incorporating radio-score and clinical characteristics with *P*-values <0.05 in the univariate logistic regression analysis. The chosen features with *P*-values <0.05 in the multivariable analysis were used to build a radiomics-based model, which was presented as a radiomic nomogram in the training cohort. The ROC curve was applied to evaluate the discriminative performance of the radiomic nomogram in training, internal validation, and external validation cohorts. A calibration curve was applied to evaluate the radiomic nomogram in all cohorts. To estimate the clinical usefulness of the prediction models, decision curve analysis (DCA) was performed to assess the net benefit of the radiomic nomogram and signature in the training, internal validation, and external validation cohorts.

Statistical analysis

In this study, we employed IBM SPSS Statistics (Version 20.0, USA) to assess the clinical data. The t-tests or the Mann–Whitney U-test were used to compare the numerical data (age and BMI), while the Chi-square or Fisher tests were used to compare the categorical data (sex, sex, tumor location, CEA, CA19-9, CA12-5, AFP level, CT-reported T stage, and N stage) in the training, internal validation, and external validation cohorts. Furthermore, the t-test or the Mann–Whitney U-test was used to assess the correlation between radiomic features and MMR status in the training cohort, which was the first dimensionality reduction. The R software (version 3.3.1, Austria; http://www.R-project.org) was used to study the radiomic feature data and build a prediction model. A *P*-value of <0.05 was defined as statistically significant.

Results

Patients' clinical characteristics

The characteristics of GC patients are presented in Table 1. Cohort 1 was randomly divided into a training cohort (n = 176, average age: 62 years old; range: 23–87 years old) with 107 males and 69 females, and an internal validation cohort (n = 76, average age: 62 years old; range: 30–83 years old) with 50 males and 26 females. There were 91 GC patients, 55 males and 36 females (average age: 61 years old; range: 37–78 years old) in the external validation cohort. In the training cohort, statistically significant differences in age, sex, tumor location, CEA level, and CT-reported T stage were identified between pMMR and dMMR patients (*P*-value <0.05), while other clinical features (BMI, CA19-9 level, CA125 level, AFP level, and CT-reported N stage) showed no statistically significant differences (*P*-value >0.05). Furthermore, we found that age and CT-reported N stage showed statistically significant differences between pMMR and dMMR patients in the internal validation cohort. There were also only two clinical features (sex and CEA level) that had significant differences in the external validation cohort.

Radiomic signature establishment

Of eight hundred and fifty-one radiomic features extracted from the delineated ROIs, 49 features with ICCs <0.8 were excluded (Supplementary Table S2). A total of 802 radiomic features were found to be substantially different between pMMR and dMMR patients, and they were used to build a radiomic signature *via* least absolute shrinkage and selection operator regression with tenfold cross-validation. Finally, 15 radiomic features were chosen to evaluate the Rad-score of each GC patient (Supplementary Table S3). The difference in Rad-scores was statistically significant between pMMR and dMMR patients in training, internal validation, and external validation cohorts (*P*-value <0.001). The radiomic signature in the training cohort is depicted in Figure 3.

The Rad-score of the dMMR group was significantly higher than that of the pMMR group in training, internal validation, and external validation cohorts. The AUC of the radiomic signature for the training cohort was 0.876 (95% CI: 0.824–0.928) (Figure 4A). The training cohort had a sensitivity of 77.4%, a specificity of 83.8%, and an accuracy of 81.3%. In the internal validation cohort, the AUC of the radiomic signature was higher than that of the training cohort (AUC = 0.966, 95% CI: 0.933–0.999) (Figure 4B). The internal validation cohort had a sensitivity of 75.9%, a specificity of 95.7%, and an accuracy of 88.0%. Furthermore, the AUC of the radiomic signature for the external validation cohort was 0.913 (95% CI: 0.857–0.969) with

TABLE 1 Characteristics of GC patients in training, internal validation and external validation cohorts.

Characteristics	Training cohort (n = 176)		*P*-value	Internal validation cohort (n = 76)		*P*-value	External validation cohort (n = 91)		*P*-value
	pMMR	dMMR		pMMR	dMMR		pMMR	dMMR	
Age (year)	59.70 ± 9.91	65.94 ± 11.47	**<0.001**	58.15 ± 11.72	64.23 ± 12.18	**0.033**	61.72 ± 8.15	61.30 ± 11.29	0.828
BMI	22.10 ± 3.39	21.98 ± 3.47	0.825	22.29 ± 3.08	22.40 ± 2.81	0.884	22.54 ± 2.93	22.80 ± 3.68	0.714
Sex			**0.024**			0.715			**0.001**
Male	71	36		31	19		46	9	
Female	34	35		15	11		18	18	
Tumor location			**0.039**			0.855			0.558
Upper-third	31	10		11	6		15	4	
Middle-third	26	17		10	8		18	10	
Lower-third	48	44		25	16		31	13	
CEA level			**0.003**			0.299			**0.030**
Normal	87	69		38	28		54	27	
Abnormal	18	2		8	2		10	0	
CA19-9 level			0.617			0.694			0.719
Normal	86	56		37	23		50	22	
Abnormal	19	15		9	7		14	5	
CA12-5 level			0.781			1.000			0.579
Normal	98	67		44	29		62	25	
Abnormal	7	4		2	1		2	2	
AFP level			0.722			0.153			0.508
Normal	101	69		46	28		63	26	
Abnormal	4	2		0	2		1	1	
CT-reported T stage			**<0.001**			0.258			0.141
T1	18	11		7	6		6	2	
T2	16	12		4	3		7	4	
T3	32	19		14	14		19	14	
T4	39	29		21	7		32	7	
CT-reported N stage			0.089			**0.019**			0.647
N0	42	45		18	20		48	19	
N1 + N2 + N3	63	26		28	10		16	8	
Rad-scores	−2.36 ± 2.63	1.01 ± 1.73	**<0.001**	−3.52 ± 4.00	1.67 ± 1.57	**<0.001**	−2.33 ± 3.80	0.93 ± 1.24	**<0.001**

pMMR, proficient DNA mismatch repair; dMMR, deficient DNA mismatch repair; BMI, body mass index; CEA normal range: 0–6.5 ng/ml; CA19-9 normal range: 0-27 U/ml; CA12-5 normal range: 0-35 U/ml, AFP normal range: 0-7 ng/ml. The bolded P-value showed statistically significant (P-value<0.05).

a sensitivity of 74.1%, specificity of 84.4%, and accuracy of 81.3% (Figure 4C).

The performance difference between CT features and selected radiomic features to predict MMR status

To compare the performance between semantic features and 15 selected radiomic features to predict MMR status, we constructed predictive models, respectively. The highest AUC values of semantic features were 0.64 (95% CI: 0.52–0.75) and 0.64 (95% CI: 0.53–0.74) in the internal validation and external cohorts (Table 2). However, 15 selected radiomic features showed significantly better performance, with the highest AUC values of 0.82 (95% CI: 0.72–0.90) and 0.71 (95% CI: 0.60–0.80) in the internal validation and external cohorts (Table 3). The AUC value of the radiomic signature was also significantly higher than the combined CT features model in the internal validation and external cohorts.

Construction of radiomic nomogram

In the univariate and multivariate logistic regression analyses, age, CT-reported N stage, and Rad-score were independent predictors for assessing MMR status. In the univariate analysis, sex and CEA level were significantly

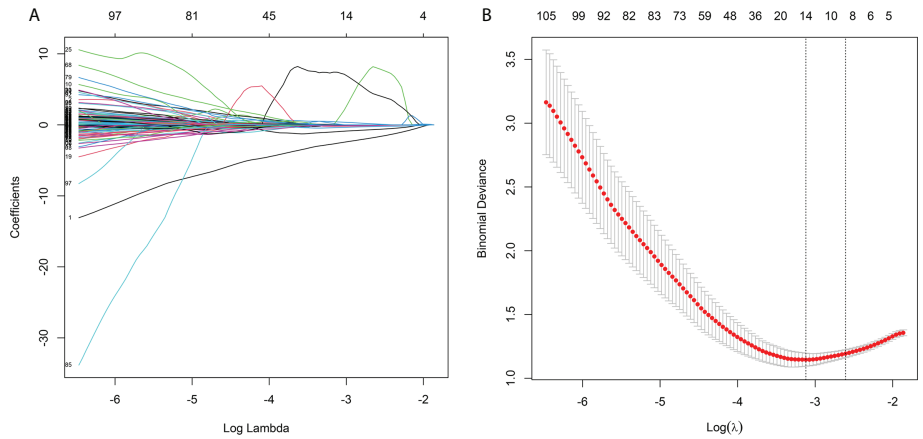

FIGURE 3
Feature selection using LASSO logistic regression and the least absolute shrinkage. **(A)** LASSO coefficient profiles of the features. Different color line shows the corresponding coefficient of each feature. **(B)** Tuning parameter (λ) selection in LASSO model. The first vertical line was drawn *via* ten-fold cross-validation based on minimum criteria.

correlated with MMR status, while no statistically significant correlation was found in the multivariate analysis (Table 4). Then, we used age, CT-reported N stage, and the Rad-score to build a radiomic nomogram to predict MMR status in the three cohorts (Figure 6A). The radiomic nomogram showed good performance for predicting MMR status in the training cohort with an AUC of 0.902 (95% CI: 0.853–0.951), in the internal validation cohort with an AUC of 0.972 (95% CI: 0.945–1.000), and in the external validation cohort with an AUC of 0.891 (95% CI: 0.825–0.958) (Figure 5). The training cohort showed a sensitivity of 80.3%, a specificity of 91.4%, and an accuracy of 86.9%. The internal validation cohort had a sensitivity of 70.0%, a specificity of 97.8%, and an accuracy of 86.8%. The external validation cohort had a sensitivity of 77.8%, a specificity of 81.3%, and an accuracy of 80.2%. The calibration curve of the radiomic signature and nomogram of three cohorts is presented in Figure 6B and Supplementary Figure 2, suggesting that the prediction model was acceptable. The DCA showed that the radiomic signature and nomogram would offer a more net benefit than either the default of all dMMR or non-dMMR in the three cohorts (Figure 6C and Supplementary Figure 2).

Discussion

In this study, we developed and validated a prediction model to assess the MMR status of GC patients based on a radiomic signature and two clinical features: age and CT-reported N stage. The radiomic nomogram performed well in predicting MMR status in the training (AUC = 0.902), internal validation (AUC = 0.972), and external validation (AUC = 0.891) cohorts.

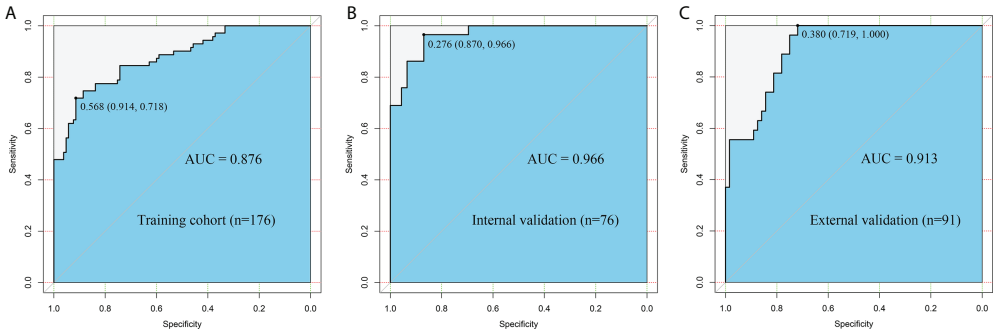

FIGURE 4
The ROC curves of the radiomic signature in the **(A)** training cohort, **(B)** internal validation cohort, and **(C)** external validation cohort.

TABLE 2 The performance of CT features extracted by radiologist to predict MMR status

Semantic features	AUC (95%CI)	
	Internal validation cohort	External validation cohort
Long diameters of tumor (mm)	0.57 (0.45–0.69)	0.63 (0.52–0.73)
Short diameters of tumor (mm)	0.54 (0.42–0.65)	0.55 (0.44–0.66)
Tumor thickness (mm)	0.53 (0.42–0.65)	0.58 (0.47–0.68)
CT value of tumor in PP (HU)	0.53 (0.41–0.65)	0.64 (0.53–0.74)
Location (up and mid vs low)	0.53 (0.42–0.65)	0.57 (0.46–0.67)
CT-reported N stage (N0 vs Nx)	0.64 (0.52–0.75)	0.52 (0.42–0.63)
CT-reported T stage	0.60 (0.49–0.71)	0.60 (0.49–0.70)
Combined semantic features model	0.63 (0.49–0.76)	0.53 (0.39–0.66)

MMR status. 95% CI, 95% confidence interval.

An increasing number of studies have confirmed that MSI-H or MMR deficiency is a remarkable biomarker for the diagnosis, treatment, and prognosis of GC patients (26, 27). MSI is defined as a phenotype of high mutation genomic MS, which is on account of MMR deficiency. Currently, MSI or MMR deficiency is detected by IHC and PCR-based molecular testing using tumor tissue after gastrectomy (28, 29). However, postoperative pathological results did not give timely advice on neoadjuvant therapy for individuals with locally advanced GC. Although preoperative gastroscopy can sample tumor tissue for testing MMR status, two limitations remain: histological assessment is also impacted by tumor tissue dynamic progression and geographic heterogeneity. Ottini et al. confirmed the heterogeneity of intratumoral MSI patterns observed in GC biology by assessing the microsatellite allele pattern in various sections of the same tumor studied (30). Similarly, Mathiak et al. showed that a biphasic MSH2 expression status in the same GC neoplasm (5%–23% of the tumor area was MSS and 85% MSI) (31). Radiomics features extracted from CT images were used in this study to assess the whole tumor and were easily repeated throughout the treatment period with no invasion. Previous studies showed that dMMR GC was significantly associated with CT semantic features, including a lower location, fewer lymph nodes, and smaller tumor thickness, implying that dMMR may be evaluated *via* radiomic features (18). To our knowledge, this is the first study to assess the potential of radiomic features to predict MMR status in GC based on preoperative clinical characteristics. Our

TABLE 3 The performance of selected radiomic features to predict MMR status.

Radiomics features	AUC (95% CI)	
	Internal validation cohort	External validation cohort
Original shape elongation	0.82 (0.72–0.90)	0.68 (0.57–0.77)
Original shape flatness	0.61 (0.49–0.72)	0.57 (0.45–0.66)
Original shape surface area	0.68 (0.57–0.79)	0.59 (0.48–0.69)
Original glcm Imc2	0.72 (0.60–0.82)	0.68 (0.57–0.77)
Wavelet LHL glcm cluster shade	0.56 (0.44–0.67)	0.58 (0.48–0.69)
Wavelet LHL glcm cluster tendency	0.61 (0.50–0.72)	0.69 (0.59–0.78)
Wavelet LHL glcm Idn	0.67 (0.56–0.78)	0.54 (0.43–0.64)
Wavelet HLL glcm Idn	0.66 (0.55–0.77)	0.59 (0.48–0.69)
Wavelet LHL glrlm run entropy	0.65 (0.53–0.76)	0.70 (0.60–0.79)
Wavelet LHH first order 10 percentile	0.53 (0.41–0.64)	0.59 (0.48–0.69)
Wavelet HHH first order total energy	0.66 (0.54–0.76)	0.61 (0.50–0.71)
Wavelet HHL first order total energy	0.65 (0.53–0.76)	0.63 (0.52–0.73)
Wavelet HLH glszm small area high gray level emphasis	0.69 (0.58–0.79)	0.68 (0.57–0.77)
Wavelet LHL gldm small dependence emphasis	0.56 (0.44–0.67)	0.71 (0.60–0.80)
Wavelet HHL glrlm low gray level run emphasis	0.67 (0.55–0.77)	0.63 (0.52–0.73)
Radiomics signature	0.97 (0.93–1.00)	0.91 (0.86–0.97)

95% CI, 95% confidence interval.

TABLE 4 Univariate and multivariate logistic regression analysis of risk factors of MMR status.

Variable	Univariate Logistic Regression		Multivariate Logistic Regression	
	OR (95% CI)	*P* value	OR (95% CI)	*P* value
Sex (male *vs* female)	0.57 (0.34–0.97)	**0.036**	0.49 (0.21–1.12)	0.094
Age	1.05 (1.02–1.08)	**<0.001**	1.05 (1.01–1.09)	**0.014**
BMI	0.99 (0.92–1.07)	0.900		
CEA level (normal vs abnormal)	0.20 (0.07–0.58)	**0.003**	2.94 (0.82–10.50)	0.097
CA19-9 level (normal vs abnormal)	1.22 (0.65–2.28)	0.528		
CA12-5 level (normal vs abnormal)	0.82 (0.26–2.52)	0.732		
AFP level (normal vs abnormal)	1.51 (0.37–6.20)	0.563		
Location (up and mid vs low)	1.31 (0.90–1.90)	0.146		
CT-reported N stage (N0 vs Nx)	0.36 (0.21–0.61)	**<0.001**	2.30 (1.04–5.07)	**0.038**
CT-reported T stage	0.94 (0.75–1.19)	0.654		
Rad-scores	3.23 (2.38–4.38)	**<0.001**	2.98 (2.18–4.08)	**<0.001**

OR, odds ratio; 95% CI, 95% confidence interval; BMI, body mass index; CEA normal range: 0–6.5 ng/ml; CA19-9 normal range: 0–27 U/ml; CA12-5 normal range: 0–35 U/ml, AFP normal range: 0–7 ng/ml. The bolded P-value showed statistically significant (P-value <0.05).

study confirmed that the radiomic signature based on CT images performed well in predicting the MMR status of GC in the training (AUC = 0.876, 95% CI: 0.824–0.928), internal validation (AUC = 0.966, 95% CI: 0.933–0.999), and external validation cohorts (AUC = 0.913, 95% CI: 0.857–0.969). In comparison to colorectal cancer research, our prediction model appears to have greater diagnostic power for assessing MMR GC status (8, 19). Furthermore, a gastroscopic biopsy or surgery is a procedure that requires good physical condition for the patient, but it cannot be conducted on patients who have inadequate circumstances. Thus, this prediction model was a useful supplement strategy for predicting the MMR status of GC with a relatively non-invasion technique.

Radiomics converts medical pictures into mineable data by high-throughput extraction of numerous quantitative based on shape, size, volume, and other factors, which has proved useful in the investigation of diseased conditions (32, 33). Radiomic features differ from traditional semantic features of medical images extracted by radiologists in that they contain more messages about tumors and are more objective (33). In the radiomic signature, elongation represented the best independent risk to predict MMR status in GC with an AUC of 0.82 (95% CI: 0.72–0.90) in the internal validation cohort. Likewise, shape-related radiomic features, such as elongation, flatness, and surface area, outperformed semantic shape features extracted by radiologists. Several similar studies confirmed that elongation, flatness, standard deviation, skewness, kurtosis, and tumor contrast were promising radiomic features for gene expression prediction (34, 35). In particular, elongation and flatness features showed better identification of high Ki-67 expression in adrenocortical carcinoma by the Spearman rank method (36). The remaining independent predictors of radiomic features were 11 wavelet features and one gray level co-occurrence matrix feature. The AUC value of the radiomic

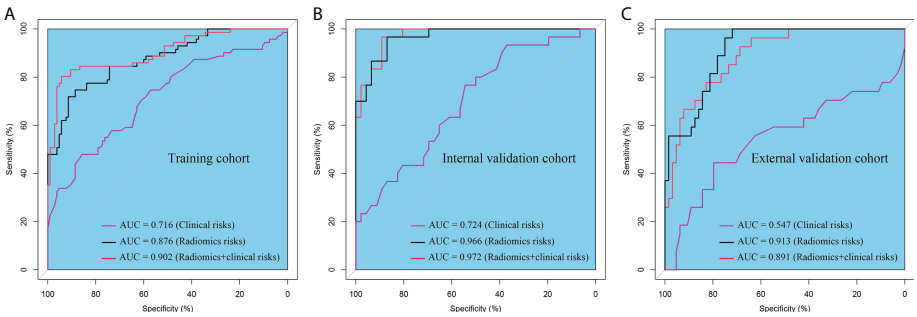

FIGURE 5
The ROC curves of the clinical risk, radiomic signature and radiomic nomogram (radiomic signature + clinical risk) in the **(A)** training cohort, **(B)** internal validation cohort, and **(C)** external validation cohort.

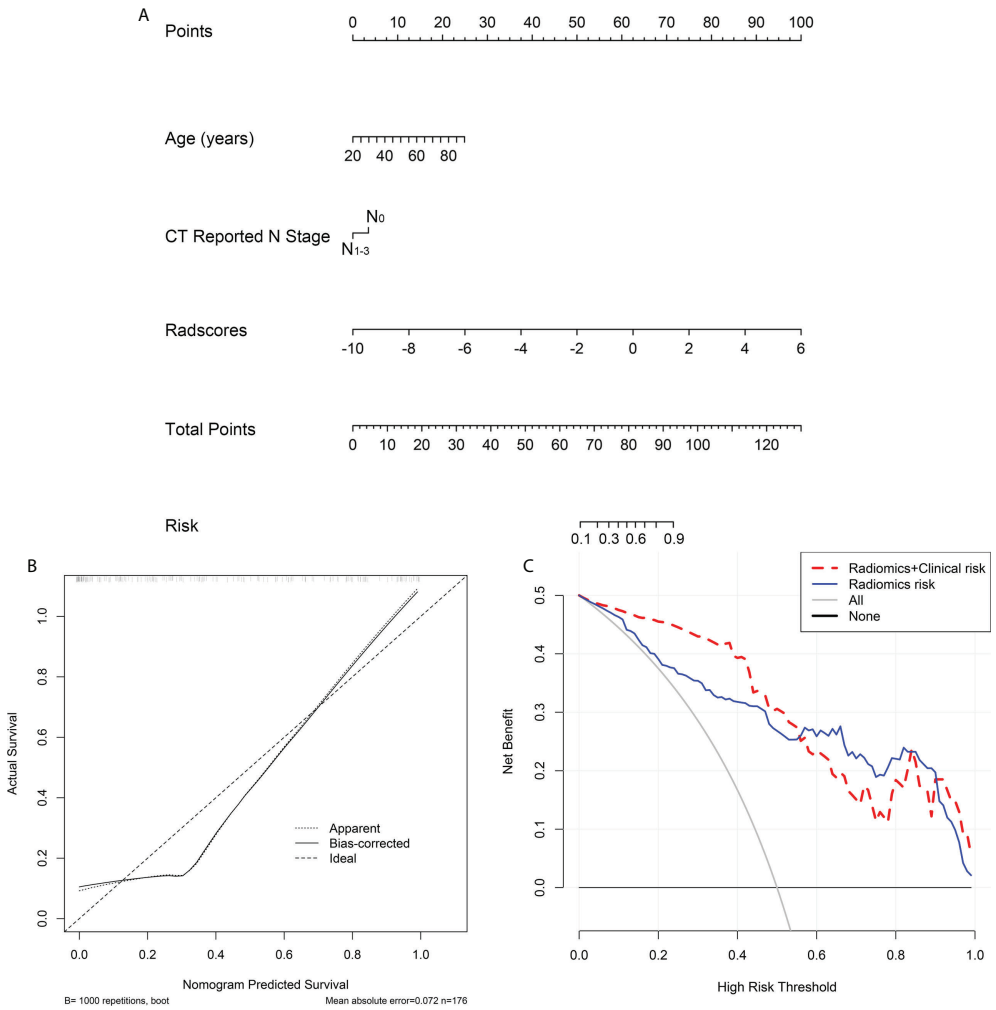

FIGURE 6
Radiomics nomogram developed with ROC, calibration curves, and decision curve analysis (DCA). **(A)** A radiomic nomogram was constructed in the training cohort *via* radiomic signature, age and CT reported N stage. **(B)** Calibration curve of the radiomic nomogram in the training cohort. **(C)** DCAs for radiomic nomogram and signature in the training cohort.

signature was significantly higher than the combined CT features model in the internal validation and external cohorts with 0.97 (95% CI: 0.93–1.00) and 0.91 (95% CI: 0.86–0.97). Several previous researches demonstrated that wavelet features were significantly correlated with heterogeneity indices at the cellular level, which were promising radiomic features to evaluate prognosis in colorectal liver metastases patients (37). In this study, the radiomic signature that we constructed showed a reliable model to predict MMR status in GC, outperforming traditional semantic features extracted by radiologists.

Additionally, many studies have focused on the correlation between MMR status and different clinical features, which can be used to discriminate molecular expression levels and give individualized therapeutic guidance (38, 39). Previous studies showed that dMMR GCs were significantly correlated with female sex, advanced age, distal location, and intestinal type (40, 41). Martinez and coworkers discovered that GC patients with dMMR showed an earlier clinical stage (TNM stage I or II) and Borrmann type I or II, while they were initially diagnosed (21). In our studies, we found that the dMMR phenotype was also significantly associated with older age and fewer CT-reported lymphatic metastases. However, no association was detected between dMMR and CEA, CA19-9, CA12-5, or AFP levels in the blood tumor markers. Furthermore, Yexing and colleagues built a radiomic nomogram based on the radiomic signature and clinical features that performed well in determining HER2 status (16). We employed age, CT-reported N stage, and the Rad-score to develop a radiomic nomogram to

predict MMR status. The radiomic nomogram showed good performance for predicting MMR status in the training cohort with an AUC of 0.902 (95% CI: 0.853–0.951), in the internal validation cohort with an AUC of 0.972 (95% CI: 0.945–1.000), and in the external validation cohort with an AUC of 0.891 (95% CI: 0.825–0.958). Okihide et al. constructed a clinical features model to predict dMMR, which showed lower evaluating capability with an AUC of 0.82 (95% CI: 0.75–0.87) and the model was not tested by the validation cohort, which may make the model unrepresentable (17). Therefore, our radiomic nomogram can efficiently discriminate dMMR GCs using a radiomic signature and clinical features in the preoperative.

Currently, radiomics-based GC research has focused on preoperative lymph node metastasis, Lauren categorization, the tumor immune milieu, genetic subtypes, and GC prognosis prediction (42–47). Identifying dMMR is crucial in our research since it guides preoperative clinical management for GC patients. Firstly, dMMR seems to be a biomarker for GC, which was associated with less lymphatic metastasis and an earlier T stage (41). Secondly, GC patients with confirmed MMR status are extremely important in clinical practice for guiding adjuvant and perioperative treatment (48, 49). A 1,990 GC patient study showed that dMMR GCs did not have better benefits in terms of disease-free survival (DFS) than pMMR GCs following R0 resection (6). When GC patients were treated only with surgery vs groups treated with chemotherapy, stage II or III GCs with dMMR status were correlated with better overall survival (OS) (50). The above results were confirmed by a multinational meta-analysis, which showed that GC patients with pMMR benefit from surgery plus chemotherapy rather than dMMR (51). Thirdly, MMR status might be associated with a response to immune checkpoint inhibitors in GC patients. A meta-analysis including 2,545 GC patients (including phase III KEYNOTE-062, CheckMate-649, JAVELIN Gastric 100, and KEYNOTE-061) revealed that GC patients with dMMR should be identified as a highly immunosensitive and specific subgroup for anti-PD-1 therapy (5), because of their intrinsic mutational burden-activated expression of immune checkpoints and inflammation (4, 52). Therefore, when patients are diagnosed, their MMR status must be accurately identified in order to provide a customized therapeutic schedule.

In this study, the main limitation is the retrospective nature of the study, which might have resulted in selection bias. However, we first built and validated a radiomic nomogram to assess the MMR protein status of GC patients based on the radiomic signature and clinical features. Secondly, because the distinction between tumor tissue and adjacent normal gastric tissue can be maximized in the portal venous phase, the radiomic features were only extracted from CT images of the portal phase. We will use other phases to evaluate MMR protein status in the future. Thirdly, although the study cohorts were collected from two hospitals, multi-center cohorts are really needed to verify the generalization ability of the predictive model. Fourthly, at the same time, we should design prospective research to demonstrate the practicability of the radiomic model.

Conclusion

We developed and validated a radiomic nomogram model that might be accurate to assess the MMR protein status of GC patients based on the radiomic signature and clinical features (age and CT-reported N stage). This prediction model is also a noninvasive detection model that can guide preoperative clinical management.

Data availability statement

The datasets presented in this study can be found in online repositories. The names of the repository/repositories and accession number(s) can be found in the article/ Supplementary Material.

Ethics statement

This study was reviewed and approved by the Ethics Committee of the First Affiliated Hospital of Nanchang University. Written informed consent for participation was not required for this study in accordance with the national legislation and the institutional requirements.

Author contributions

QZ, ZF, and LeL conceived the project and wrote the manuscript. YZ and FZ drew the ROI of CT images. XS, AW, and LiL participated in data analysis. YC and YT participated in discussion and language editing. JX and ZL reviewed the manuscript. All authors contributed to the article and approved the submitted version.

Funding

This work was supported by the National Natural Science Foundation of China (No. 81860428), the Key R&D General Project of Jiangxi Science and Technology Department (20203 BBGL73187), and Youth Fund of Jiangxi Provincial Science and Technology Department (20202 BABL216051).

Conflict of interest

The authors declare that the research was conducted in the absence of any commercial or financial relationships that could be construed as a potential conflict of interest.

Publisher's note

All claims expressed in this article are solely those of the authors and do not necessarily represent those of their affiliated organizations, or those of the publisher, the editors and the reviewers. Any product that may be evaluated in this article, or claim that may be made by its manufacturer, is not guaranteed or endorsed by the publisher.

Supplementary material

The Supplementary Material for this article can be found online at: https://www.frontiersin.org/articles/10.3389/fonc.2022.883109/full#supplementary-material

References

1. Sung H, Ferlay J, Siegel RL, Laversanne M, Soerjomataram I, Jemal A, et al. Global cancer statistics 2020: GLOBOCAN estimates of incidence and mortality worldwide for 36 cancers in 185 countries. *CA Cancer J Clin* (2021) 71:209–49. doi: 10.3322/caac.21660

2. Lin JX, Xu YC, Lin W, Xue FQ, Ye JX, Zang WD, et al. Effectiveness and safety of apatinib plus chemotherapy as neoadjuvant treatment for locally advanced gastric cancer: A nonrandomized controlled trial. *JAMA Netw Open* (2021) 4: e2116240. doi: 10.1001/jamanetworkopen.2021.16240

3. Wang Y, Li Z, Shan F, Miao R, Xue K, Li Z, et al. Current status of diagnosis and treatment of early gastric cancer in China–data from China gastrointestinal cancer surgery union. *Zhonghua Wei Chang Wai Ke Za Zhi* (2018) 21:168–74.

4. Kim ST, Cristescu R, Bass AJ, Kim KM, Odegaard JI, Kim K, et al. Comprehensive molecular characterization of clinical responses to PD-1 inhibition in metastatic gastric cancer. *Nat Med* (2018) 24:1449–58. doi: 10.1038/s41591-018-0101-z

5. Pietrantonio F, Randon G, Di Bartolomeo M, Luciani A, Chao J, Smyth EC, et al. Predictive role of microsatellite instability for PD-1 blockade in patients with advanced gastric cancer: a meta-analysis of randomized clinical trials. *ESMO Open* (2021) 6:100036. doi: 10.1016/j.esmoop.2020.100036

6. An JY, Kim H, Cheong JH, Hyung WJ, Kim H, Noh SH. Microsatellite instability in sporadic gastric cancer: its prognostic role and guidance for 5-FU based chemotherapy after R0 resection. *Int J Cancer* (2012) 131:505–11. doi: 10.1002/ijc.26399

7. Akagi K, Oki E, Taniguchi H, Nakatani K, Aoki D, Kuwata T, et al. Real-world data on microsatellite instability status in various unresectable or metastatic solid tumors. *Cancer Sci* (2021) 112:1105–13. doi: 10.1111/cas.14798

8. Li Z, Zhong Q, Zhang L, Wang M, Xiao W, Cui F, et al. Computed tomography-based radiomics model to preoperatively predict microsatellite instability status in colorectal cancer: A multicenter study. *Front Oncol* (2021) 11:666786. doi: 10.3389/fonc.2021.666786

9. Svensson MC, Borg D, Zhang C, Hedner C, Nodin B, Uhlen M, et al. Expression of PD-L1 and PD-1 in chemoradiotherapy-naive esophageal and gastric adenocarcinoma: Relationship with mismatch repair status and survival. *Front Oncol* (2019) 9:136. doi: 10.3389/fonc.2019.00136

10. Ospina OE, Wilson CM, Soupir AC, Berglund A, Smalley I, Tsai KY, et al. spatialGE: Quantification and visualization of the tumor microenvironment heterogeneity using spatial transcriptomics. *Bioinformatics* (2022) 38:2645–7. doi: 10.1093/bioinformatics/btac145

11. Jiang Y, Liang X, Han Z, Wang W, Xi S, Li T, et al. Radiographical assessment of tumour stroma and treatment outcomes using deep learning: a retrospective, multicohort study. *Lancet Digit Health* (2021) 3:e371–82. doi: 10.1016/S2589-7500(21)00065-0

12. Kubota Y, Kawazoe A, Sasaki A, Mishima S, Sawada K, Nakamura Y, et al. The impact of molecular subtype on efficacy of chemotherapy and checkpoint inhibition in advanced gastric cancer. *Clin Cancer Res* (2020) 26:3784–90. doi: 10.1158/1078-0432.CCR-20-0075

13. Sang NV, Duc NM, Duc PH, Tuan PA. The value of multidetector-row computed tomography in lymph node staging of gastric cancer: a preliminary Vietnamese study. *Contemp Oncol (Pozn)* (2020) 24:125–31. doi: 10.5114/wo.2020.97484

14. Gao X, Ma T, Cui J, Zhang Y, Wang L, Li H, et al. A CT-based radiomics model for prediction of lymph node metastasis in early stage gastric cancer. *Acad Radiol* (2021) 28:e155–64. doi: 10.1016/j.acra.2020.03.045

15. Gao X, Ma T, Bai S, Liu Y, Zhang Y, Wu Y, et al. A CT-based radiomics signature for evaluating tumor infiltrating treg cells and outcome prediction of gastric cancer. *Ann Transl Med* (2020) 8:469. doi: 10.21037/atm.2020.03.114

16. Li Y, Cheng Z, Gevaert O, He L, Huang Y, Chen X, et al. A CT-based radiomics nomogram for prediction of human epidermal growth factor receptor 2 status in patients with gastric cancer. *Chin J Cancer Res* (2020) 32:62–71. doi: 10.21147/j.issn.1000-9604.2020.01.08

17. Suzuki O, Yamaguchi T, Fukuchi M, Mochiki E, Arai T, Akagi K, et al. Prediction model for gastric cancer with DNA mismatch repair deficiency. *Anticancer Res* (2021) 41:975–82. doi: 10.21873/anticanres.14851

18. Cao Q, Lai SY, Xu N, Lu Y, Chen S, Zhang XS, et al. Computed tomography features of gastric cancer patients with DNA mismatch repair deficiency. *Front Oncol* (2021) 11:619439. doi: 10.3389/fonc.2021.619439

19. Li J, Yang Z, Xin B, Hao Y, Wang L, Song S, et al. Quantitative prediction of microsatellite instability in colorectal cancer with preoperative PET/CT-based radiomics. *Front Oncol* (2021) 11:702055. doi: 10.3389/fonc.2021.702055

20. Wang FH, Zhang XT, Li YF, Tang L, Qu XJ, Ying JE, et al. The Chinese society of clinical oncology (CSCO): Clinical guidelines for the diagnosis and treatment of gastric cancer, 2021. *Cancer Commun (Lond)* (2021) 41:747–95. doi: 10.3760/cma.j.issn.1671-0274.2018.02.010

21. Martinez-Ciarpaglini C, Fleitas-Kanonnikoff T, Gambardella V, Llorca M, Mongort C, Mengual R, et al. Assessing molecular subtypes of gastric cancer: microsatellite unstable and Epstein-Barr virus subtypes. methods for detection and clinical and pathological implications. *ESMO Open* (2019) 4:e000470. doi: 10.1136/esmoopen-2018-000470

22. Sun KY, Hu HT, Chen SL, Ye JN, Li GH, Chen LD, et al. CT-based radiomics scores predict response to neoadjuvant chemotherapy and survival in patients with gastric cancer. *BMC Cancer* (2020) 20:468. doi: 10.1186/s12885-020-06970-7

23. Li R, Li J, Wang X, Liang P, Gao J. Detection of gastric cancer and its histological type based on iodine concentration in spectral CT. *Cancer Imaging* (2018) 18:42. doi: 10.1186/s40644-018-0176-2

24. Kim DK, Kang SH, Kim JS, Rou WS, Joo JS, Kim MH, et al. Feasibility of using two-dimensional axial computed tomography in pretreatment decision making for patients with early gastric cancer. *Med (Baltimore)* (2020) 99:e18928. doi: 10.1097/MD.0000000000018928

25. van Griethuysen JJM, Fedorov A, Parmar C, Hosny A, Aucoin N, Narayan V, et al. Computational radiomics system to decode the radiographic phenotype. *Cancer Res* (2017) 77:e104–7. doi: 10.1158/0008-5472.CAN-17-0339

26. Cristescu R, Lee J, Nebozhyn M, Kim KM, Ting JC, Wong SS, et al. Molecular analysis of gastric cancer identifies subtypes associated with distinct clinical outcomes. *Nat Med* (2015) 21:449–56. doi: 10.1038/nm.3850

27. Miceli R, An J, Di Bartolomeo M, Morano F, Kim ST, Park SH, et al. Prognostic impact of microsatellite instability in Asian gastric cancer patients enrolled in the ARTIST trial. *Oncology* (2019) 97:38–43. doi: 10.1159/000499628

28. Luchini C, Bibeau F, Ligtenberg MJL, Singh N, Nottegar A, Bosse T, et al. ESMO recommendations on microsatellite instability testing for immunotherapy in cancer, and its relationship with PD-1/PD-L1 expression and tumour mutational

burden: a systematic review-based approach. *Ann Oncol* (2019) 30:1232–43. doi: 10.1093/annonc/mdz116

29. Berg KD, Glaser CL, Thompson RE, Hamilton SR, Griffin CA, Eshleman JR. Detection of microsatellite instability by fluorescence multiplex polymerase chain reaction. *J Mol Diagn* (2000) 2:20–8. doi: 10.1016/S1525-1578(10)60611-3

30. Puliga E, Corso S, Pietrantonio F, Giordano S. Microsatellite instability in gastric cancer: Between lights and shadows. *Cancer Treat Rev* (2021) 95:102175. doi: 10.1016/j.ctrv.2021.102175

31. Mathiak M, Warneke VS, Behrens HM, Haag J, Boger C, Kruger S, et al. Clinicopathologic characteristics of microsatellite instable gastric carcinomas revisited: Urgent need for standardization. *Appl Immunohistochem Mol Morphol* (2017) 25:12–24. doi: 10.1097/PAI.0000000000000264

32. Salvatore C, Castiglioni I, Cerasa A. Radiomics approach in the neurodegenerative brain. *Aging Clin Exp Res* (2021) 33:1709–11. doi: 10.1007/s40520-019-01299-z

33. Mayerhoefer ME, Materka A, Langs G, Haggstrom I, Szczypinski P, Gibbs P, et al. Introduction to radiomics. *J Nucl Med* (2020) 61:488–95. doi: 10.2967/jnumed.118.222893

34. Juan MW, Yu J, Peng GX, Jun LJ, Feng SP, Fang LP. Correlation between DCE-MRI radiomics features and ki-67 expression in invasive breast cancer. *Oncol Lett* (2018) 16:5084–90. doi: 10.3892/ol.2018.9271

35. Zhou B, Xu J, Tian Y, Yuan S, Li X. Correlation between radiomic features based on contrast-enhanced computed tomography images and ki-67 proliferation index in lung cancer: A preliminary study. *Thorac Cancer* (2018) 9:1235–40. doi: 10.1111/1759-7714.12821

36. Ludwig CG, Lauric A, Malek JA, Mulligan R, Malek AM. Performance of radiomics derived morphological features for prediction of aneurysm rupture status. *J Neurointerv Surg* (2021) 13:755–61. doi: 10.1136/neurintsurg-2020-016808

37. Granata V, Fusco R, Setola SV, De Muzio F, Dell' Aversana F, Cutolo C, et al. CT-based radiomics analysis to predict histopathological outcomes following liver resection in colorectal liver metastases. *Cancers (Basel)* (2022) 14:1648. doi: 10.3390/cancers14071648

38. Polom K, Marano L, Marrelli D, De Luca R, Roviello G, Savelli V, et al. Meta-analysis of microsatellite instability in relation to clinicopathological characteristics and overall survival in gastric cancer. *Br J Surg* (2018) 105:2645–7. doi: 10.1002/bjs.10663

39. Pereira MA, Ramos M, Dias AR, Faraj SF, Ribeiro RRE, de Castria TB, et al. Expression profile of markers for targeted therapy in gastric cancer patients: HER-2, microsatellite instability and PD-L1. *Mol Diagn Ther* (2019) 23:761–71. doi: 10.1007/s40291-019-00424-y

40. Bermudez A, Arranz-Salas I, Mercado S, Lopez-Villodres JA, Gonzalez V, Rius F, et al. Her2-positive and microsatellite instability status in gastric cancer-clinicopathological implications. *Diagnostics (Basel)* (2021) 11:944. doi: 10.3390/diagnostics11060944

41. Zubarayev M, Min EK, Son T. Clinical and molecular prognostic markers of survival after surgery for gastric cancer: tumor-node-metastasis staging system and beyond. *Transl Gastroenterol Hepatol* (2019) 4:59. doi: 10.21037/tgh.2019.08.05

42. Dong D, Fang MJ, Tang L, Shan XH, Gao JB, Giganti F, et al. Deep learning radiomic nomogram can predict the number of lymph node metastasis in locally advanced gastric cancer: an international multicenter study. *Ann Oncol* (2020) 31:912–20. doi: 10.1016/j.annonc.2020.04.003

43. Jiang Y, Wang H, Wu J, Chen C, Yuan Q, Huang W, et al. Noninvasive imaging evaluation of tumor immune microenvironment to predict outcomes in gastric cancer. *Ann Oncol* (2020) 31:760–8. doi: 10.1016/j.annonc.2020.03.295

44. Wang XX, Ding Y, Wang SW, Dong D, Li HL, Chen J, et al. Intratumoral and peritumoral radiomics analysis for preoperative Lauren classification in gastric cancer. *Cancer Imaging* (2020) 20:83. doi: 10.1186/s40644-020-00358-3

45. Wang S, Feng C, Dong D, Li H, Zhou J, Ye Y, et al. Preoperative computed tomography-guided disease-free survival prediction in gastric cancer: a multicenter radiomics study. *Med Phys* (2020) 47:4862–71. doi: 10.1002/mp.14350

46. Yang J, Wu Q, Xu L, Wang Z, Su K, Liu R, et al. Integrating tumor and nodal radiomics to predict lymph node metastasis in gastric cancer. *Radiother Oncol* (2020) 150:89–96. doi: 10.1016/j.radonc.2020.06.004

47. Zhang W, Fang M, Dong D, Wang X, Ke X, Zhang L, et al. Development and validation of a CT-based radiomic nomogram for preoperative prediction of early recurrence in advanced gastric cancer. *Radiother Oncol* (2020) 145:13–20. doi: 10.1016/j.radonc.2019.11.023

48. van Velzen MJM, Derks S, van Grieken NCT, Haj Mohammad N, van Laarhoven HWM. MSI as a predictive factor for treatment outcome of gastroesophageal adenocarcinoma. *Cancer Treat Rev* (2020) 86:102024. doi: 10.1016/j.ctrv.2020.102024

49. Sohn BH, Hwang JE, Jang HJ, Lee HS, Oh SC, Shim JJ, et al. Clinical significance of four molecular subtypes of gastric cancer identified by the cancer genome atlas project. *Clin Cancer Res* (2017) 23:4441–9. doi: 10.1158/1078-0432.CCR-16-2211

50. Kim SY, Choi YY, An JY, Shin HB, Jo A, Choi H, et al. The benefit of microsatellite instability is attenuated by chemotherapy in stage II and stage III gastric cancer: Results from a large cohort with subgroup analyses. *Int J Cancer* (2015) 137:819–25. doi: 10.1002/ijc.29449

51. Pietrantonio F, Raimondi A, Choi YY, Kang W, Langley RE, Kim YW, et al. MSI-GC-01: Individual patient data (IPD) meta-analysis of microsatellite instability (MSI) and gastric cancer (GC) from four randomized clinical trials (RCTs). *J Clin Oncol* (2019) 37:66–6. doi: 10.1200/JCO.2019.37.4_suppl.66

52. Di Bartolomeo M, Morano F, Raimondi A, Miceli R, Corallo S, Tamborini E, et al. Prognostic and predictive value of microsatellite instability, inflammatory reaction and PD-L1 in gastric cancer patients treated with either adjuvant 5-FU/LV or sequential FOLFIRI followed by cisplatin and docetaxel: A translational analysis from the ITACA-s trial. *Oncologist* (2020) 25:e460–8. doi: 10.1634/theoncologist.2019-0471

frontiers | Frontiers in Oncology

TYPE Original Research
PUBLISHED 22 December 2022
DOI 10.3389/fonc.2022.1026305

OPEN ACCESS

EDITED BY
Bo Zhang,
Sichuan University, China

REVIEWED BY
Youping Xiao,
Fujian Provincial Cancer Hospital, China
Yazhou Wu,
Army Medical University, China

*CORRESPONDENCE
Chuangzhen Chen
czchen2@stu.edu.cn
Fangcai Wu
280550109@qq.com

†These authors have contributed equally to this work and share first authorship

SPECIALTY SECTION
This article was submitted to Gastrointestinal Cancers: Gastric and Esophageal Cancers, a section of the journal Frontiers in Oncology

RECEIVED 23 August 2022
ACCEPTED 01 December 2022
PUBLISHED 22 December 2022

CITATION
Liu W, Zeng C, Wang S, Zhan Y, Huang R, Luo T, Peng G, Wu Y, Qiu Z, Li D, Wu F and Chen C (2022) A combined predicting model for benign esophageal stenosis after simultaneous integrated boost in esophageal squamous cell carcinoma patients (GASTO1072). *Front. Oncol.* 12:1026305. doi: 10.3389/fonc.2022.1026305

A combined predicting model for benign esophageal stenosis after simultaneous integrated boost in esophageal squamous cell carcinoma patients (GASTO1072)

Weitong Liu[1,2†], Chengbing Zeng[1†], Siyan Wang[1†], Yizhou Zhan[1], Ruihong Huang[1], Ting Luo[1,3], Guobo Peng[1], Yanxuan Wu[1], Zihan Qiu[4], Derui Li[1], Fangcai Wu[1*] and Chuangzhen Chen[1*]

[1]Department of Radiation Oncology, Cancer Hospital of Shantou University Medical College, Shantou, China, [2]Department of Radiation Oncology, Jieyang People's Hospital, Jieyang, China, [3]Department of Radiation Oncology, Shenshan Central Hospital, Sun Yat-Sen Memorial Hospital, Sun Yat-Sen University, Shanwei, China, [4]Department of Otolaryngology-Head and Neck Surgery, The First Affiliated Hospital of Shantou University Medical College, Shantou, China

Purpose: We aimed to develop a combined predicting model for benign esophageal stenosis (BES) after simultaneous integrated boost (SIB) with concurrent chemotherapy in patients with esophageal squamous cell carcinoma (ESCC).

Methods: This study included 65 patients with EC who underwent SIB with chemotherapy. Esophageal stenosis was evaluated using esophagograms and the severity of eating disorders. Risk factors were investigated using univariate and multivariate analyses. Radiomics features were extracted based on contrast-enhanced CT (CE-CT) before treatment. The least absolute shrinkage and selection operator (LASSO) regression analysis was used for feature selection and radiomics signature construction. The model's performance was evaluated using Harrell's concordance index and receiver operating characteristic curves.

Results: The patients were stratified into low- and high-risk groups according to BES after SIB. The area under the curves of the clinical model, Rad-score, and the combined model were 0.751, 0.820 and 0.864, respectively. In the validation cohort, the AUCs of these three models were 0.854, 0.883 and 0.917, respectively. The Hosmer-Lemeshow test showed that there was no deviation from model fitting for the training cohort (p=0.451) and validation cohort (p=0.481). The C-indexes of the nomogram were 0.864 and 0.958 for the training and validation cohort, respectively. The model combined with Rad-score and clinical factors achieved favorable prediction ability.

Conclusion: Definitive chemoradiotherapy could alleviate tumor-inducing esophageal stenosis but result in benign stenosis. We constructed and tested a combined predicting model for benign esophageal stenosis after SIB. The nomogram incorporating both radiomics signature and clinical prognostic factors showed favorable predictive accuracy for BES in ESCC patients who received SIB with chemotherapy.

Trial registration number and date of registration: Registered in www.Clinicaltrial.gov, ID: NCT01670409, August 12, 2012

KEYWORDS

esophageal cancer, esophageal stenosis, radiomics, chemoradiotherapy, radiotherapy

Introduction

Esophageal cancer (EC) is a common gastrointestinal malignancy, with squamous cell carcinoma (ESCC) being the predominant type. It has a high incidence in Eastern and Central Asia (1, 2). Patients with locally advanced disease, particularly those with unresectable tumors have an unsatisfactory prognosis, on account of a less than 30% 5-year survival rate (3). For locally advanced EC patients who reject or cannot tolerate surgery, concurrent chemoradiotherapy has been a standard recommendation due to higher long-term survival rates and insignificant differences in late toxicity compared to single radiotherapy (4).

Recently, a clinical approach known as simultaneous integrated boost (SIB) that delivers a higher dose fractionation to the gross tumor volume while delivering a lower dose fractionation to the clinical target volume has been approved as feasible with acceptable toxicities (5–7). We also explored this therapeutic mode for esophageal squamous cell carcinoma (ESCC) in a phase II clinical trial. Preliminary results demonstrated that tumor control and overall survival improved when compared with historical data (8). The long-term outcome has been reported in European Society for Therapeutic Radiology and Oncology (ESTRO), and the phase III clinical trial was currently being conducted. Although the tolerability of such treatment regimens was acceptable in these studies, their treatment-related late toxicities were not well established, particularly in the case of benign esophageal stenosis (BES). BES arises from various etiologies including peptic, radiation, and caustic injury. It differs from malignant esophageal stenosis due to tumor mass and can impair the patient's quality of life and lead to serious complications like weight loss, malnutrition, and aspiration (9). The late toxicities of esophageal radiotherapy were predominantly manifested as benign stenosis and esophageal dysmotility (10, 11). Previous studies have shown that esophageal stenosis after conventional fractional radiotherapy of EC was correlated with the extent of the circumference involved (ECI), T stage, the longitudinal length of the tumor (LLT), and the wall thickness of the affected esophagus (12–14). Whether these factors continue to be related to BES after SIB has not been verified.

Radiomics, which extracted high-dimensional quantitative features from radiographic images to provides additional information on the heterogeneity and phenotype of tumor aggressiveness (15–17). It can be used for disease detection, cancer diagnosis, and treatment outcome prediction (18–23). Previous radiomics studies on EC have mainly focused on predicting tumor differentiation, staging, lymph node metastasis, and survival outcomes (24–27). To our knowledge, there has been no radiomics-based studies on toxicity prediction for high-dose radiotherapy in patients with ESCC.

Hence, this study sought to identify both clinical and radiomics features correlated with BES after SIB in patients with ESCC and develop a nomogram for prediction.

Methods and materials

Patients

From August 2012 to January 2018, we investigated 107 patients with ESCC who received SIB with concurrent chemotherapy from a single-arm, prospective phase II clinical trial called "simultaneous modulated accelerated radiotherapy combined with chemotherapy for esophageal cancer" (clinical trial: NCT01670409) at the Cancer Hospital of Shantou University Medical College. The trial protocol has previously been published (8). A prospective phase III clinical trial called "simultaneous modulated accelerated radiotherapy combined with chemotherapy vs concurrent chemoradiotherapy for esophageal cancer" is currently enrolling patients. Inclusion criteria: (a)Measurable lesions on imaging; (b)No obvious

esophageal mass or lymph node enlargement compressing the esophagus on CT imaging after treatment; (c)No recurrence in the tumor area during follow-up ≥ 6 months. Exclusion criteria: (a)Control failure of the tumor area during or after treatment; (b)Failure to complete radiotherapy; (c)Surgery after complete radiotherapy. As shown in Figure 1, the final study enrolled 65 patients. These patients were divided into a training group (n= 43) and a validation group (n= 22) in a ratio of 2:1.

Pre-treatment evaluation

The extent of the disease was evaluated by imaging, serological examination, and endoscopic biopsy. The clinical stage was defined according to the American Joint Cancer Committee (AJCC) staging system 6th (28). LLT and ECI were evaluated by barium esophagography, endoscopy and CE-CT images (CT scanner: 16-row Spiral CT of Bright Speed Series of GE Medical Systems, USA). CT scanning parameters were setting as follows: Tube voltage,120KpV; Rotation time, 0.75 seconds; Pitch, 1.375; Matrix, 512×512; Field of visual, 360 mm×360 mm. The wall thickness was defined by measuring the thickest portion of the tumor. The extent of circumference involvement was demarcated as follows: (a)Level 1, ≤1/2 of circumference involvement; (b)Level 2, ≥1/2 of circumference involvement but less than whole circumference involvement; (c) Level 3, whole circumference involvement. Target area delineation and radiotherapy plans were determined by CT images analyzed in the Eclipse planning system.

Treatment

All patients were treated with SIB in conjunction with chemotherapy. A higher-than-standard dose of 66 Gy/30 F was delivered to the gross tumor volume, and a lower dose of 54 Gy/30 F was delivered to the sub-clinical tumor volume. Chemotherapy was based on cisplatin and 5-fluorouracil (5-FU) for four cycles: two cycles of concurrent chemotherapy, and two cycles of adjuvant chemotherapy, after completing radiotherapy.

Follow up

For the first 2 years after treatment, patients were assessed every 3 months and then twice a year. An evaluation of patients' history, physical examination, serological test, chest X-ray with barium esophagography or CE-CT scan, and abdominal ultrasound were performed.

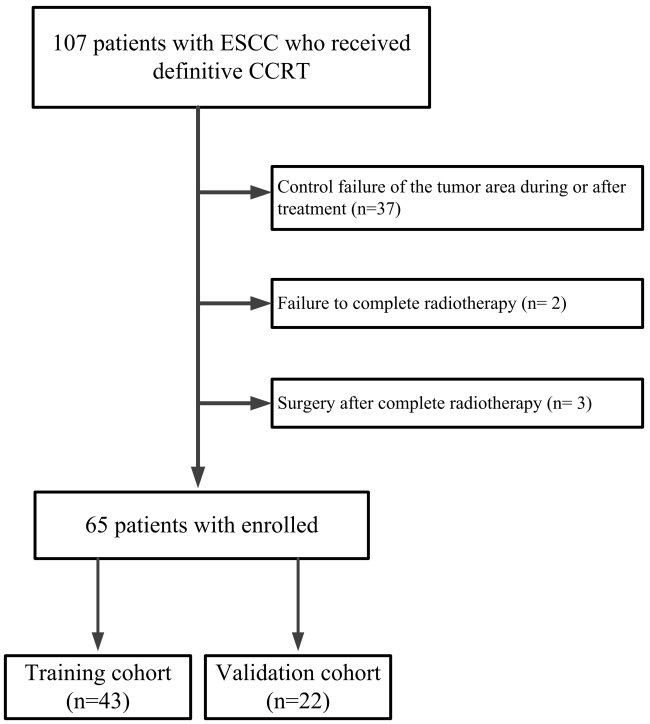

FIGURE 1
The workflow of Inclusion and Exclusion.

Outcome indicators

Esophagograms, which were performed prior to, during, after, and during follow-up examination, were used to measure the degree of esophageal stenosis. By using a barium esophagogram, we measured the widest part (a in Figure 2A) of the oral side lumen diameter and the narrowest part (b in Figure 2A) of the primary site. The stenotic ratio (c; expressed as a percentage) was then determined as c = (a-b)/a×100% (12–14). The maximum value of the stenotic ratios in follow-up review at all points in time was defined as the degree of post-treatment BES.

In the follow up review, the severity of eating disorders was recorded and categorized according to the Radiation Therapy Oncology Group (RTOG) late radiation injury score: (a)Grade 0, none; (b)Grade 1, slightly difficulty in swallowing solids; (c) Grade 2, inability to swallow solid food normally, swallowing semi-solid food; (d)Grade3, ability to swallow only liquids; (e) Grade 4, necrosis or perforation fistula (29).

We integrated the severity of eating disorders Grade 0–1 into the normal diet group and Grade≥2 into the non-normal diet group, then combined the stenotic ratio with the diet grouping to plot the ROC curve. The AUC was calculated to quantify the accuracy of the stenotic ratio in assessing the degree of esophageal stenosis. The optimal cut-off value of the stenotic ratio was determined according to the Youden index. For univariate analysis, a chi-square test, t-test, and rank sum test were performed to explore the correlation between stenotic ratio and clinical factors. For multivariate analysis, binary logistic regression analysis and a linear regression model were used.

CE-CT image acquisition and radiomics extraction

All patients underwent pre-treatment CE-CT scans (Philips Brilliance CT Big Bore Oncology Configuration, Cleveland, OH, USA). The CT voxel size was 1.0 × 1.0 × 3.0 mm^3. The CT images were transmitted to the radiation therapy planning system (Eclipse Planning System version 10.0) *via* the DICOM 3.0 port. All gross tumor volumes (GTVs) were delineated on the planning CT scans by experienced radiation oncologists. The radiomics features were extracted from every GTV using MATLAB R2016a (Mathworks, Natick, USA) and its toolbox (https://cn.mathworks.com/). These features included four groups: the intensity features, the geometric features and the texture features. According to the first-order statistics, the intensity features were calculated from the histogram of voxel intensity values in the volume of interest (VOI). The geometric features describe the shape of the VOI (30). The texture features calculated in all three-dimensional directions within the VOI, which can quantify intra-tumor heterogeneity differences, consist of gray level co-occurrence matrix (GLCM), neighborhood grey-tone difference matrix (NGTDM), gray level size zone matrix (GLSZM) and gray level run length matrix (GLRLM) (31–34). Overall, 96 radiomic features were

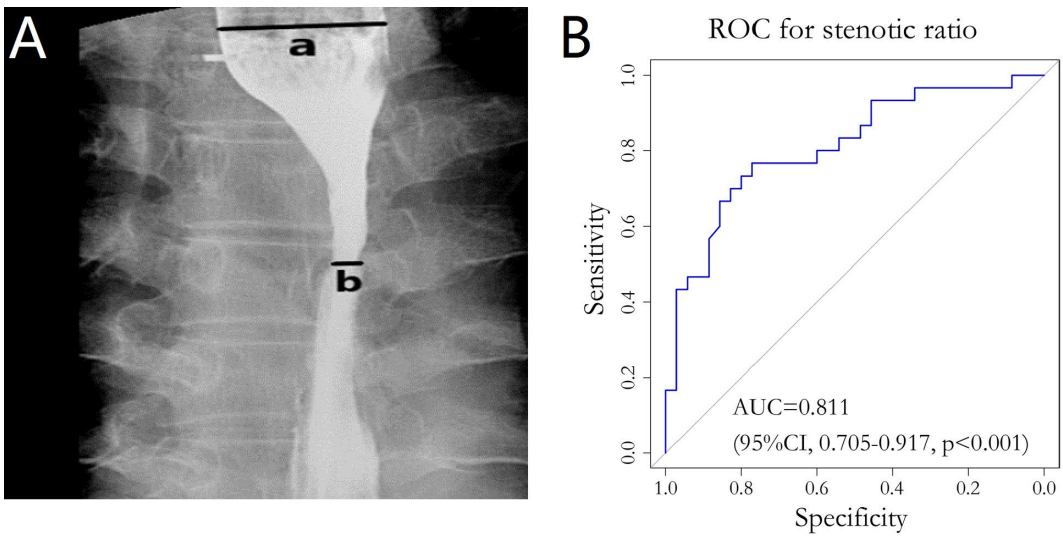

FIGURE 2
(A) Barium esophagography image. The widest part (line a in panel **A**) of the oral side and the narrowest part (line b in panel **A**) of the primary site were clearly demonstrated. **(B)** ROC curve for stenotic ratio and the diet group. ROC, Receiver operating Characteristic; AUC, Area under the curve.

extracted from every GTV. The specific types and algorithms for radiomic feature extraction have been discussed in previous studies (35, 36).

Radiomics features selection and model development

Univariate analysis was used to evaluate radiomics factors for BES. Radiomics variables with a p-value >0.250 were excluded from further analysis. Pearson correlation analysis was used to reduce the correlations between radiomics features. For example, for a pair of features with high correlation (i.e., the absolute value of correlation coefficient ≥ 0.8), the one with a lower p-value in the univariate analysis remained. The least absolute shrinkage and selection operator (LASSO) was chosen for the logistic regression model to select the most useful predictive features and create a radiomics signature model (defined as the Rad-score).

Clinical features selection and model development

Before starting treatment, clinical data including gender, age, tumor location and the TNM stage was gathered. LLT, ECI and number of CT layers in which the wall thickness of affected esophagus (NEWT) >1cm were collected from barium esophagography, endoscopy and CE-CT images. Univariate and multivariate analysis were used to identify the clinical factors correlating with BES after SIB. The potential clinical risk factors constituted the clinical model.

Combined model development

The individualized prediction model included potential clinical risk factors and the Rad-score using multivariate logistic regression analysis. To visualize the patient-level probability estimate of BES, a nomogram was developed based on multivariate logistic regression analysis and tested in the validation cohort.

Assessment of the Rad-score and nomogram

Because the clinical factors (such as ECI, LLT and NEWT>1cm) were measured on the CE-CT imaging, the VIF analysis was also used to assess the collinearity information among the clinical factors and final radiomics features. Variance inflation factor (VIF) was used to evaluate the collinearity among the final radiomics features that constituted the Rad-score. The performance of each model was evaluated using the area under the receiver operating characteristic curves (AUCs), accuracy, sensitivity and specificity.

The predictive power of the nomogram was quantified using Harrell's concordance index (C-index) and assessed using the calibration curve. The Hosmer-Lemeshow test was used to assess the goodness-of-fit of the nomogram (37). Decision curve analysis (DCA) was used to quantify the net benefit at different threshold probabilities and determine the clinical usefulness of the nomogram.

Statistical analysis

For univariate analysis, a chi-square test, t-test, and rank sum test were performed to explore the correlation between stenotic ratio and clinical factors. For multivariate analysis, binary logistic regression analysis and a linear regression model were used.

All statistical tests were conducted using R software version 4.0.5 and SPSS (version 23.0; IBM Corp., Armonk, NY, USA). The "glmnet" package was used to analyze the LASSO logistic model. The "pROC" and "car" were used to calculate the ROC curves and VIF. The C-index was calculated using the Kaplan–Meier "survival" package. The nomogram and calibration curve were built by using "rms" package. The Hosmer-Lemeshow test was calculated using the "generalhoslem" package in the R environment. Differences were considered statistically significant at $p < 0.05$.

Result

Patients' characteristics

The patient characteristics for the two cohorts are shown in Table 1. The average age of 65 patients was 61.16 ± 5.77. There were no differences in patient characteristics between the training group and validation group.

Benign esophageal stenosis after treatment

The last date of follow-up was December 22, 2019, and the median follow-up period was 62 months (17-82 months) for all patients. The change in the mean esophageal stenotic ratio of 65 patients before treatment to 1 year after treatment is shown in Table S1 and Figure S1. The change in the mean esophageal stenotic ratio of 48 patients (17 eliminated, 1 for recurrence, 2 for death, and 14 for missing follow-up) from 3 to 18 months after treatment are shown in Table S2 and Figure S2. It tended to decrease with time and reached a plateau in the ninth months after treatment.

TABLE 1 Clinical characteristics of 65 patients with ESCC after definitive CCRT.

Factors	Training cohort n (%)	Validation cohort n (%)	p-value
Age, years			0.624[b]
Average ± SD	61.16 ± 5.77	61.95 ± 6.78	
BMI, Kg/m^2			0.330[b]
Average ± SD	21.52 ± 3.31	20.70 ± 2.87	
Gender			0.906[c]
Male Female	28 (65.1%) 15 (34.9%)	14 (63.6%) 8 (36.4%)	
Tumour location			0.671[c]
Cervical Upper Middle	3 (7.0%) 18 (41.9%) 22 (51.2%)	3 (13.6%) 9 (40.9%) 10 (45.5%)	
T stage[a]			0.966[c]
T2 T3 T4	9 (20.9%) 21 (48.8%) 13 (30.2%)	5 (22.7%) 11 (50.0%) 6 (27.3%)	
N stage[a]			0.335[c]
N0 N1	19 (44.2%) 24 (55.8%)	7 (40.0%) 15 (68.2%)	
M stage[a]			0.572[c]
M0 M1	37 (86.0%) 6 (14.0%)	20 (90.9%) 2 (9.1%)	
Clinical stage[a]			0.776[c]
II stage III stage IV stage	17 (39.5%) 20 (46.5%) 6 (14.0%)	8 (36.4%) 12 (54.5%) 2 (9.1%)	
ECI			0.778
Level 1	2	2	
Level 2	27	13	
Level 3	14	17	
LLT			0.430
Average ± SD	5.01 ± 1.78	5.06 ± 1.51	
NEWT>1cm			0.911
Average± SD	9.65 ± 7.34	11.14 ± 6.72	

ESCC, esophageal squamous cell carcinoma; CCRT, concurrent chemoradiotherapy; AJCC, American Joint Committee on Cancer staging system (version 6.0[th]); RT, radiotherapy; PF, cisplatin and 5-fluorouracil.
[a]American Joint Committee on Cancer (AJCC) staging system (version 6.0[th])
[b]p-value was analysed using the independent samples t-test
[c]p-value was analysed using the chi-squared test.
IBM, imaging biomarker; CI, confidence interval; HR, hazard ratio.

The peak stenotic ratio for 24 (36.9%), 20 (30.8%), 11 (16.9%), 6 (9.2%), 2 (3.1%), 1 (1.5%), and 1 (1.5%) patient(s) occurred in the third, sixth, ninth, twelfth, fifteenth, eighteenth, and twenty-first months after treatment, respectively. Thirty-five patients (53.8%) had a normal diet when they had a peak stenotic ratio, 26 (40%) had a semi-solid diet, and 4 (6.2%) had a liquid diet. We divided these patients into a normal diet group (35 patients, 53.8%) and a non-normal diet group (30 patients, 46.2%) according to the RTOG late radiation injury score. The ROC curve was plotted by considering the stenotic

ratio as the test variable and the diet group as the status variable, which resulted in AUC=0.811 (95% CI: 0.705-0.917, p<0.001) (Figure 2B). The optimal cut-off value for stenotic ratio was determined to be 58.2% according to the Youden index, and 31 cases (47.7%) with a stenotic ratio >58.2% were defined as the benign stenotic group (high risk group). The rest of patients were defined as the low risk group.

Radiomics selection and Rad-score constructing

Ninety-six radiomics features were reduced to 30 potential factors, which had a p-value ≤ 0.25. Nineteen features were excluded after comparing the inter-variable Pearson correlation analysis. The remained 11 features were performed with non-zero coefficients in the LASSO logistic regression model. Ultimately 7 of them were chosen to construct the Rad-score. As shown in Figure 3, with the optimal tuning parameter λ value of 0.036 and log (λ) = -3.322, the Rad-score calculation formula was constructed using the LASSO logistic regression model (Formula 1):

Rad-score = −0.0037 × Max + 4.7716 × Spherical Disproportion − 1.4654 × Idistcent−2.9222 × Informaiton Measure of Correlation2_GLCM+ 0.1131 × Run_Percentage _ GLRLM−0.9177 × Texture_Strength_NGTDM−1.7964 × Small_Zone_Emphasis_GLSZM + 5

A constant value 5 was used to obtain a Rad-score >0 from the calculation formula. The VIFs of the seven radiomics features were tolerable, ranging from 1.336-2.341 (Table S3).

Development of individualized prediction model

Clinical factors were analyzed using univariate and multivariate Logistic regression, as shown in Table 2. In the training cohort, factors showing a significant correlation with BES after treatment were ECI (p=0.027), LLT (p=0.097), and the number of CT layers in which the wall thickness of affected esophagus>1cm (NEWT>1cm) (p=0.028) in the univariate analysis. VIFs of the seven radiomics features and the three clinical factors were tolerable (VIF<10), ranging from 1.593-8.640 (Table S3). We combined the clinical characteristics and the Rad-score into a multivariate logistic regression model.

Performance of the model and nomogram

The combine model performed the best among three models. Figures 4A, B deplicted the AUCs of different models. For BES, the Rad-score model was superior to the clinical model. The combine model outperformed the Rad-score or the clinical model in the training cohort, and the results were replicated in the validation cohort. The box plot method was used to compare low-risk and high-risk patients in the BES as shown in Figures 4C, D. And the results revealed significant differences (p<0.05, wilcoxon test) between two subgroups of BES in two cohorts. We also constructed a nomogram to visualize the logistic regression model of BES (Figures 5A). As shown in Figure 5B, C, the calibration curve of the nomogram for the

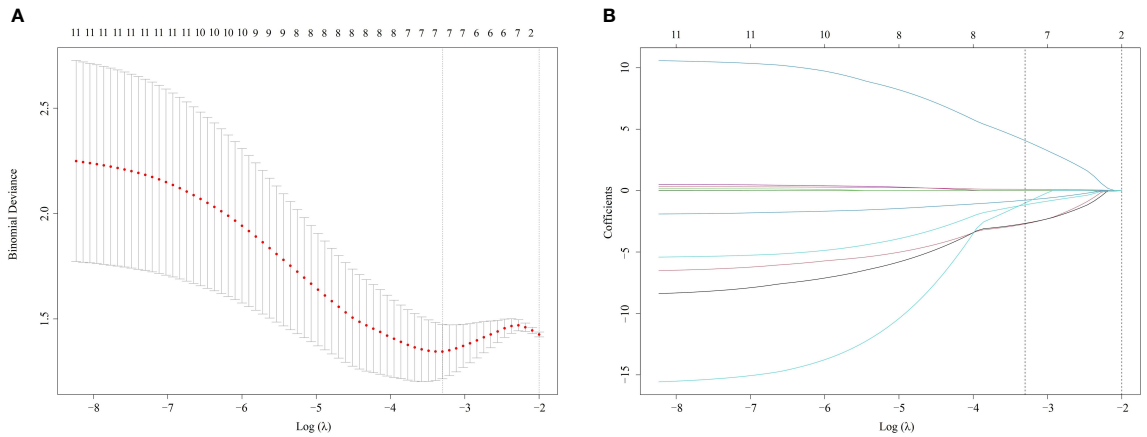

FIGURE 3
Radiomics selection using LASSO logistic regression model **(A)**. The tuning parameter λ selection of LASSO model with 10-fold cross-validation was performed to select radiomic features. At the optimal tuning parameter λ value of 0.036 and log (λ) = -3.322, the left dotted vertical line was set with the minimum criteria where 7 radiomic features were selected. **(B)**. LASSO coefficient profile of 11 Radiomic features. A coefficient profile plot was generated against the log (λ) sequence. The dotted vertical lines were drawn at the 6 non-zero coefficients, with the optimal value of λ. LASSO, least absolute shrinkage and selection operator.

TABLE 2 Univariate and multivariate association of Rad-score and clinical characteristic Logistic regression analysis of BES (likelihood Ratio: Backward stepwise).

Variables	Training cohort				Validation cohort			
	Univariate		Multivriate		Univariate		Multivriate	
	OR	*p*	OR(95%CI)	*p*	OR	*p*	OR(95%CI)	*p*
Age	1.010	0.848						
Gender	1.319	0.666						
Tumour location	1.524	0.401						
Clinical stage	0.722	0.470						
BMI	1.035	0.712						
LLT	1.365	**0.097**	1.008 (0.571-1.780)	0.977	1.614	0.148	0.566(0.165-1.945)	0.367
ECI	4.314	**0.027**	3.112(0.777-12.469)	0.109	5.210	0.069	6.080(0.735-50.303)	0.094
NEWT>1cm	1.116	**0.028**	1.087 (0.981-1.206)	0.112	1.249	0.027	1.384(1.008-1.901)	0.044

OR, odds ratio; CI, confidence interval; BMI, Body Mass Index; LLT, longitudinal length of tumor; ECI, the extent of circumference involvement; NEWT>1cm, the number of CT layers in which the wall thickness of affected esophagus>1cm.
The bold values refers to the clinical factors which were included in the clinical models.

probability prediction of BES had good prognostic performance. The DCA showed the nomogram had clinical utility in predicting the power of risk of BES within a wide range of reasonable threshold probability (Figure 6). The Hosmer-Lemeshow test revealed no deviation from model fitting for the training cohort (p=0.451) and validation cohort (p=0.481). The C-indices of the nomogram were 0.864 and 0.958 for the training and validation cohorts, respectively.

Discussion

For patients with locally advanced EC, approximately half had local recurrence and poor overall survival (38, 39). Some researchers have applied SIB to the therapy of EC to improve local control (8). Nonetheless, information on late toxicity of SIB, which contributes to the comprehensive evaluation of this therapeutic mode, is limited. Benign esophageal stenosis is one of the most common late toxicities that leads to significant deterioration in quality of life despite tumor regression. The benefits must be balanced against the risk of toxicities. Thus, developing an individual predictive model is critical for clinical decision making.

We expected that characteristics other than clinical factors, such as texture and distribution on CT imaging, might contribute to the severity of benign esophageal stenosis. As a result, our study yields promising results. We found that the Rad-score, which consisted of seven radiomics features, was discovered to be an independent risk factor for BES after SIB. In terms of clinical factors, CEI, LLT and NEWT>1cm were identified as potential factors for BES in univariate analysis, however these clinical factors were only weakly correlated with BES in multivariate analysis.

Although several studies have identified risk factors for esophageal stenosis, clinicians are unable to identify specific patients who may develop BES after radiotherapy (12–14). It is necessary to identify patients who have a high risk of BES after SIB before treatment, as these patients might be more suitable for surgery or immunotherapy. And the radiation dose should be further explored in such patients. Hence, a prediction model based on radiomics and clinical factors that discriminated severe BES after SIB with high diagnostic performance was developed in this study.

The radiomics signature model incorporates some individual radiomics features as predictors to probe the clinical utility of features that have been explored and investigated in many studies (40, 41). Max was extracted from the intensity features. It measures the maximum value of the gray level intensity. According to our findings, a smaller Max value may be related to a poor BES result. SphericalDisproportion refers to the ratio of the tumor region's perimeter to the perimeter of a sphere with the same surface area as the tumor region. Idistcent describes the maximum distance between the vertices of the tumor surface grid in the axial plane. Tumors with a larger SphericalDisproportion or a smaller Idistcent had more irregular shape, which was associated with poorer treatment response (15, 42, 43). In terms of texture feature, the Information Measure of Correlation2_GLCM refers to the consistency of the gray level of image texture in the row or column directions. It is high when gray levels are equally distributed along the row or column direction in contoured structures. A smaller Information Measure of Correlation2_GLCM, indicating the ROI heterogeneity (44). Run_Percentage_GLRLM measures the texture roughness by dividing run length by voxels in ROI. Texture_Strength_NGTDM represents the significance and uniqueness of voxels on a three-dimensional level.

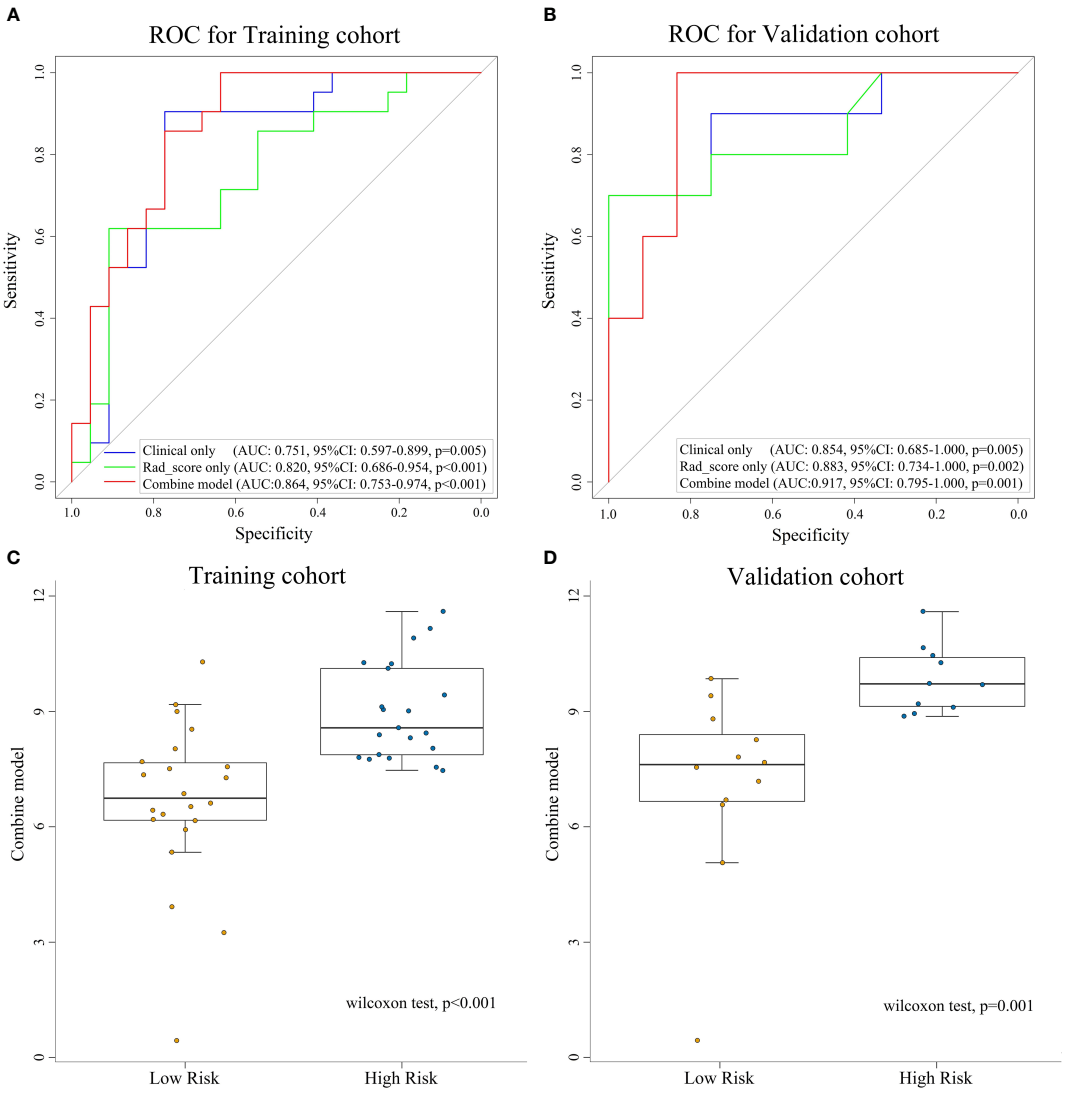

FIGURE 4
ROC curves for assessing the different performance of three models in training cohort **(A)** and validation cohort **(B)**. The box plots of combine model for low-risk and high-risk groups for training cohort **(C)** and validation cohort **(D)**. ROC, receive operation characteristic; AUC, area under the curve; CI, confidence interval; Rad-score, radiomic score.

Small_Zone_Emphasis_GLSZM describes of the distribution of small areas. The finer the contoured structures are, the larger the value, the smaller the zone. The previous studies observed that Information Measure of Correlation2_GLCM, the Run_Percentage_GLRLM, Texture_Strength_NGTDM and Small_Zone_Emphasis_GLSZM are highly relevant to the heterogeneity and prognosis of Specific types of tumor (15, 44, 45). These results demonstrate the possibility of using radiomics multivariate analysis and the high OR of the radiomics signature model might able to predict BES in patients with ESCC. However, these seven radiomic features did not achieve the significant statistical value due to insufficient number of patients. It needs to be further confirmed in the validation cohort and larger prospective cohorts. Several previous studies have reported that combining radiomic signatures (or features) and clinical risk factors improved the predictive accuracy of these models (26, 35, 46, 47). Thus, we developed a nomogram that incorporates the Rad-score as well as these clinical factors. These clinical factors are generally available during treatment, and the collection of information does not require additional examinations or place an additional economic burden on patients. Despite the fact that these clinical factors were insignificantly different in multivariate analysis, incorporating them into the radiomics signature model, which comprised the combined model, improved the AUC in predicting BES and achieved excellent discrimination in this cohort.

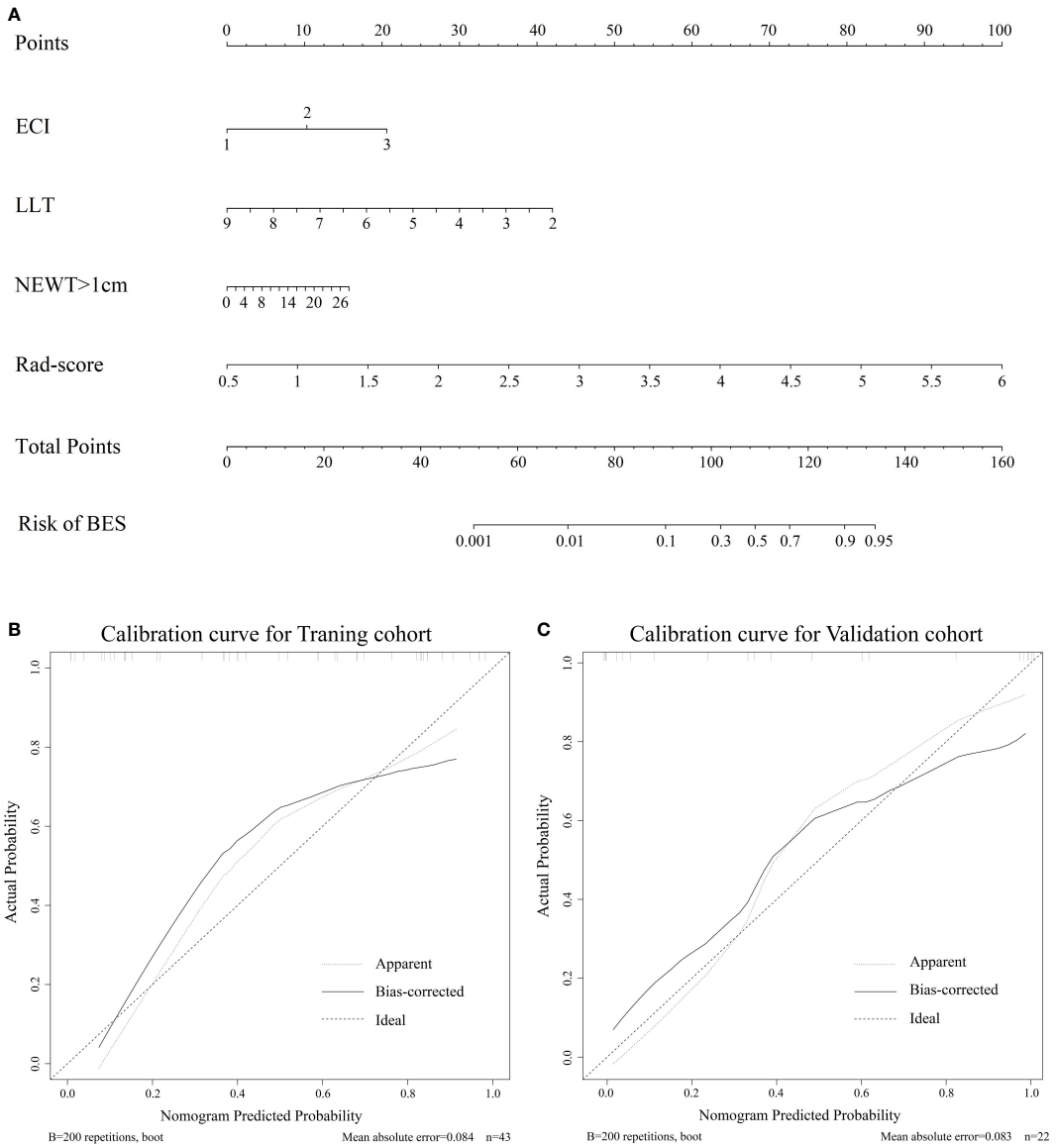

FIGURE 5
(A). The nomogram for the prediction of BES. The constructed nomograms were used to estimate the risk of BES for individual ESCC patients. Calibration curves of the combined nomogram in the training cohort **(B)** and validation cohort **(C)**. The calibration curves describe the calibration of the combine nomogram in terms of the conformity between the predicted risk of BES and observed BES outcomes. The 45° dotted line represents a perfect prediction, the solid lines represent the bias-corrected performance of the combine nomogram. BES, benign esophageal stenosis; ESCC, esophageal squamous cell carcinoma; ECI: the extent of circumference involvement; LLT: longitudinal length of tumor; NEWT>1cm: number of CT layers with esophageal wall thickness >1 cm.

This study demonstrated that the esophageal stenotic ratio tended to decrease during and after treatment, with the mean stenotic ratio dropping from 72.0% before treatment to 46.5% 1 year after treatment, reflecting a distinct remission of stenosis caused by tumor mass. Re-stenosis was considered because the maximum stenotic ratio during follow-up was greater than that at the completion of treatment. Two other studies (12, 14) reported that the peak stenotic ratio occurred–5-8 and 6-8 months after treatment, but specific numbers and proportions of cases at each point in time were not displayed. In previous studies (12–14), the evaluation of stenosis has basically referred to the barium esophagogram as follows: Grade 1 (<25%), Grade 2 (25~50%), Grade 3 (50~75%), and Grade 4 (75~100%); grade ≥3 is defined as stenosis, or referred to the RTOG late radiation injury score, which was classified based on the patients' subjective experience of eating disorders. Atsumi K et al.,

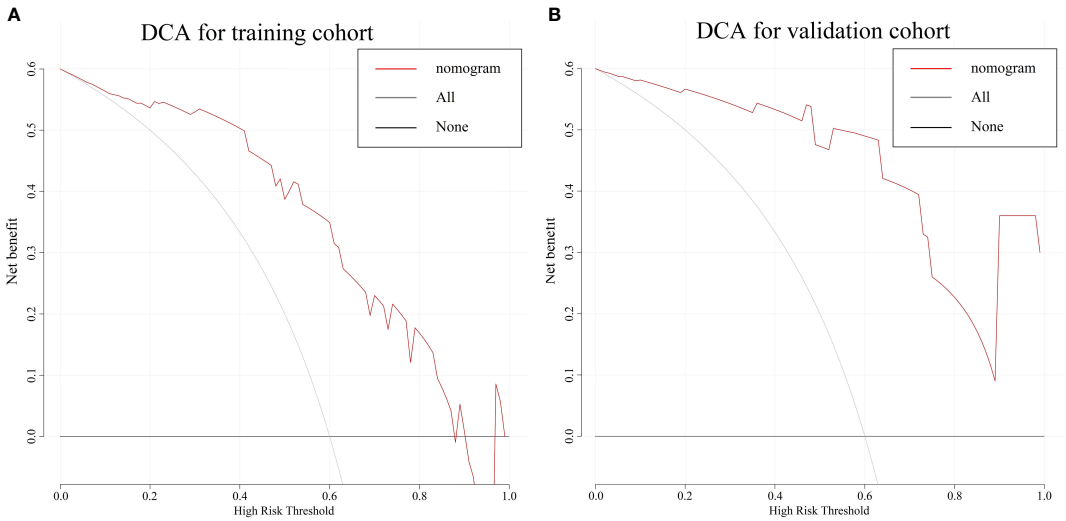

FIGURE 6
The DCA for the combine nomogram in the training cohort **(A)** and validation cohort **(B)**. The y-axis represents the net benefit. The x-axis represents the threshold probability. The red line represents the radiomics nomogram. The grey line represents the hypothesis that all patients had BES. The black line represents the hypothesis that no patients had BES. The DCA in two cohorts showed the nomogram had clinical benefit. DCA, Decision curve analysis; BES, benign esophageal stenosis.

Wang et al., and Luo et al. all used stenotic ratio to assess the degree of BES after high dose radiotherapy (ranging 54-71.4Gy, 56-66Gy, 56-70Gy, respectively), and 23%, 43.5% and 33.8% of patients had a stenotic ratio >50% respectively in their researches (12–14). All the above studies found BES was not correlated with RT dose. In this study, we combined the RTOG late radiation injury score and stenotic ratio to create an ROC curve, and the result showed AUC=0.811, indicating that the stenotic ratio was considered capable of objectively evaluating the extent of esophageal stenosis. According to the optimal cut-off value, stenotic ratio>58.2% was defined as benign stenosis. The rate of BES after 66 Gy radiotherapy was 47.7%. The evaluation of stenosis could be more accurate and convincing by the integration of the two above.

Previous studies have explored the risk factors for esophageal stenosis after conventional fractional radiotherapy. The extent of circumference involvement, T stage, tumor length, and the wall thickness of the affected esophagus has been confirmed by Atsumi et al. in a 109 EC patient study, Wang et al. in a 61-patient study, Luo et al. in a 71-patient study, and Kim et al. in a 62-patient study (12–14, 48). The extent of circumference involvement was a risk factor for stenosis after endoscopic mucosal resection of early EC (49).

Dysphagia is the most common symptom in advanced patients and has a significant impact on quality of life. The mechanism of BES after chemoradiotherapy has not been determined due to limited pathological data. It is commonly assumed that post-radiotherapy esophageal stenosis is caused by radiation-induced fibrosis (RIF). Because of fibrosis and inflammation of the submucosa and muscular layers, the esophagus loses its elasticity, resulting in post-radiotherapy esophageal stenosis 4-12 months after therapy and developing in a few years (50). However, the stenotic ratio of patients in our study tended to reach a plateau after 9 months. This may be because long-term esophageal peristalsis controlled by autonomic nerves, even without food intake, may decrease the damage of fibrosis. For BES, balloon dilatation, stent implantation, bypass operation, and drug infusion are the most commonly used palliative treatments (51), but they had unsatisfactory outcomes for high re-stenosis rate and complications, like perforation and hemorrhage (52–54).

This study was conducted prospectively to indentify the risk factors associated with BES by combining objective evaluation using esophagography with subjective evaluation of the severity of eating disorders in patients, and build an individual predictive model incorporating radiomics features and clinical factors. It could be a useful guide when choosing a treatment option for patients with EC as well as an important piece of information when acquiring a patient's informed consent before radiotherapy.

The innovation of this study is that this study was a prospective study for BES after SIB for ESCC. Since the difficulty of long time follow up, there is scarce data for BES after high dose radiotherapy for esophageal cancer. The application of radiomics in CE-CT imaging has been focused on specific topics, such as survival outcomes and diagnosis (55).

To the best of our knowledge, this is the first predict model that applied radiomics to assess BES after SIB.

The limitations of this study include the lack of comparison with patients receiving standard-dose radiotherapy because all the patients in these prospective studies received SIB. The NCCN Guidelines state that a standard dose of definitive radiation for esophageal cancer is 50–50,4 Gy (1.8–2.0 Gy/day) (total 25–28 fractions). However, more than 50% of patients who had standard-dose CRT subsequently experienced recurrence or distant metastases and passed away from this illness (56). A dose of 60.0 Gy or more has become a more common dose of CCRT in Asian nations where ESCC is the predominate histological type since studies have shown that a greater dose than 50.4 Gy of CCRT could be safely administered without significant adverse effects and yield a high probability of local control (8, 57, 58). Since high dose radiotherapy of 60 Gy or more with 2 Gy per fraction, is frequently used in China to treat esophageal cancer, it can be challenging to collect clinical information concerning standard dose of radiotherapy, particularly for a prospective study. Our hospital is currently conducting a phase III trial, and we will eventually include a standard dose of radiotherapy in our prediction model. There were no T1 patients in our study; therefore, the impact of T stage on esophageal stenosis after SIB needs further verification. Another limitation of our study is the small sample size and the lack of external validation of the model. Clinical data for BES was difficult to acquire due to long time follow up. Wang et al. analyzed BES after radiotherapy ranging 56-66Gy and included 62 patients from 2005 to 2008 (12). Luo et al. analyzed BES after radiotherapy ranging 56-70Gy and included 71 patients from 2010 to 2013 (14). Jun W. Kim et al. analyzed BES after radiotherapy ranging 45-90Gy and included 62 patients from 2001 to 2015 (48). These were all retrospective studies with a wider range of radiotherapy dose. The challenge of gathering information of BES is a pervasive problem in this research field. That is why the sample size in this study is small and it is indeed a weakness. To overcome the shortcoming of limited sample size we did use the 10-fold cross validation method in this study. K-fold cross validation was reported to reduce the uncertainty of input dataset partition in previous study (59, 60). Multicenter validation with a larger sample size is required for clinical applications.

Conclusion

In conclusion, BES due to tumor mass could achieve varying degrees of remission after simultaneous modulated accelerated radiotherapy, but BES occurs after radiotherapy at the same time. BES after SIB was potential associated with the Rad-score, CEI, LLT and NEWT>1cm. We developed a nomogram that incorporates both the Rad-score and clinical prognostic factors to predict the risk of BES in patients with ESCC who received definitive CCRT.

Data availability statement

The raw data supporting the conclusions of this article will be made available by the authors, without undue reservation.

Ethics statement

This study was performed in line with the principles of the Declaration of Helsinki. Approval was granted by the Ethics Committee of Shantou University Medical College (2013-04-28/ No. SUMC2013XM-0085). Informed consent was obtained from all individual participants included in the study. The patients/ participants provided their written informed consent to participate in this study.

Author contributions

All authors contributed to the study conception and design. Material preparation, data collection and analysis were performed by CC, WL, CZ, and SW. The first draft of the manuscript was written by WL and all authors commented on previous versions of the manuscript. All authors contributed to the article and approved the submitted version.

Funding

This study was funded by Shantou University Medical College Clinical Research Enhancement Initiative, N0201424 (to CC); Science and Technology Special Fund of Guangdong Province of China, 2019-132 (to CC); Strategic and Special Fund for Science and Technology Innovation of Guangdong Province of China, 180918114960704 (to CC); Innovative Research Group Project of the National Natural Science Foundation of China, 82173079 (to CC).

Conflict of interest

The authors declare that the research was conducted in the absence of any commercial or financial relationships that could be construed as a potential conflict of interest.

Publisher's note

All claims expressed in this article are solely those of the authors and do not necessarily represent those of their affiliated organizations, or those of the publisher, the editors and the reviewers. Any product that may be evaluated in this article, or

claim that may be made by its manufacturer, is not guaranteed or endorsed by the publisher.

Supplementary material

The Supplementary Material for this article can be found online at: https://www.frontiersin.org/articles/10.3389/fonc.2022.1026305/full#supplementary-material

SUPPLEMENTARY FIGURE 1
The change in the mean esophageal stenotic ratio of 65 patients before treatment to 1 year after treatment. Seven points in x axis represent before treatment, twentieth fraction, complete treatment, 3, 6, 9, and 12 months after completing treatment.

SUPPLEMENTARY FIGURE 2
The change in the mean esophageal stenotic ratio of 48 patients from 3 to 18 months after treatment. Six points in x axis represent 3, 6, 9, 12, 15, and 18 months after completing treatment.

References

1. Lin Y, Totsuka Y, Shan B, Wang C, Wei W, Qiao Y, et al. Esophageal cancer in high-risk areas of China: Research progress and challenges. *Ann Epidemiol* (2017) 27(3):215–21. doi: 10.1016/j.annepidem.2016.11.004

2. Feng RM, Zong YN, Cao SM, Xu RH. Current cancer situation in China: good or bad news from the 2018 global cancer statistics? *Cancer Commun (London England)* (2019) 39(1):22. doi: 10.1186/s40880-019-0368-6

3. Doosti-Irani A, Holakouie-Naieni K, Rahimi-Foroushani A, Mansournia MA, Haddad P. A network meta-analysis of the treatments for esophageal squamous cell carcinoma in terms of survival. *Crit Rev Oncol Hematol* (2018) 127:80–90. doi: 10.1016/j.critrevonc.2018.05.007

4. Cooper JS, Guo MD, Herskovic A, Macdonald JS, Martenson JAJr., Al-Sarraf M, et al. Chemoradiotherapy of locally advanced esophageal cancer: Long-term follow-up of a prospective randomized trial (RTOG 85-01). *Radiat Ther Oncol Group Jama* (1999) 281(17):1623–7. doi: 10.1001/jama.281.17.1623

5. Kim HJ, Suh YG, Lee YC, Lee SK, Shin SK, Cho BC, et al. Dose-response relationship between radiation dose and loco-regional control in patients with stage II-III esophageal cancer treated with definitive chemoradiotherapy. *Cancer Res Treat Off J Korean Cancer Assoc* (2017) 49(3):669–77. doi: 10.4143/crt.2016.354

6. Yu WW, Zhu ZF, Fu XL, Zhao KL, Mao JF, Wu KL, et al. Simultaneous integrated boost intensity-modulated radiotherapy in esophageal carcinoma: Early results of a phase II study. *Strahlentherapie und Onkologie: Organ der Deutschen Rontgengesellschaft [et al]* (2014) 190(11):979–86. doi: 10.1007/s00066-014-0636-y

7. Li C, Ni W, Wang X, Zhou Z, Deng W, Chang X, et al. A phase I/II radiation dose escalation trial using simultaneous integrated boost technique with elective nodal irradiation and concurrent chemotherapy for unresectable esophageal cancer. *Radiat Oncol (London England)* (2019) 14(1):48. doi: 10.1186/s13014-019-1249-5

8. Chen J, Guo H, Zhai T, Chang D, Chen Z, Huang R, et al. Radiation dose escalation by simultaneous modulated accelerated radiotherapy combined with chemotherapy for esophageal cancer: a phase II study. *Oncotarget* (2016) 7 (16):22711–9. doi: 10.18632/oncotarget.8050

9. Shah JN. Benign refractory esophageal strictures: widening the endoscopist's role. *Gastrointest Endosc* (2006) 63(1):164–7. doi: 10.1016/j.gie.2005.08.033

10. Coia LR, Engstrom PF, Paul A. Nonsurgical management of esophageal cancer: report of a study of combined radiotherapy and chemotherapy. *J Clin oncology: Off J Am Soc Clin Oncol* (1987) 5(11):1783–90. doi: 10.1200/JCO.1987.5.11.1783

11. Coia LR, Myerson RJ, Tepper JE. Late effects of radiation therapy on the gastrointestinal tract. *Int J Radiat Oncol Biol Phys* (1995) 31(5):1213–36. doi: 10.1016/0360-3016(94)00419-L

12. Wang C, Lv C, Wang J, Liu J, Guo J, Li H. Analysis of risk factors of developing esophageal stricture after radiotherapy for esophageal carcinoma. *Zhong Guo Zhong Liu Lin Chuang* (2010) 37(10):579–81+86. doi: 10.3969/j.issn.1000-8179.2010.10.011

13. Atsumi K, Shioyama Y, Arimura H, Terashima K, Matsuki T, Ohga S, et al. Esophageal stenosis associated with tumor regression in radiotherapy for esophageal cancer: frequency and prediction. *Int J Radiat Oncol Biol Phys* (2012) 82(5):1973–80. doi: 10.1016/j.ijrobp.2011.01.047

14. Luo J, Lu X, Zhou X, Lu Z. Shi guan ai fang liao hou liang xing xia zhai de xiang guan yin su fen xi [analysis of risk factors of esophageal benign stricture after radiotherapy for esophageal carcinoma]. *Zhong Hua Zhong Liu Fang Zhi Za Zhi* (2015) 22(13):1046–9. doi: 10.16073/j.cnki.cjcpt.2015.13.012

15. Lambin P, Leijenaar RTH, Deist TM, Peerlings J, de Jong EEC, van Timmeren J, et al. Radiomics: the bridge between medical imaging and personalized medicine. *Nat Rev Clin Oncol* (2017) 14(12):749–62. doi: 10.1038/nrclinonc.2017.141

16. Thawani R, McLane M, Beig N, Ghose S, Prasanna P, Velcheti V, et al. Radiomics and radiogenomics in lung cancer: A review for the clinician. *Lung Cancer (Amsterdam Netherlands)* (2018) 115:34–41. doi: 10.1016/j.lungcan.2017.10.015

17. Bodalal Z, Trebeschi S, Nguyen-Kim TDL, Schats W, Beets-Tan R. Radiogenomics: bridging imaging and genomics. *Abdominal Radiol (New York)* (2019) 44(6):1960–84. doi: 10.1007/s00261-019-02028-w

18. Gillies RJ, Kinahan PE, Hricak H. Radiomics: Images are more than pictures, they are data. *Radiology* (2016) 278(2):563–77. doi: 10.1148/radiol.2015151169

19. van Rossum PSN, Xu C, Fried DV, Goense L, Court LE, Lin SH. The emerging field of radiomics in esophageal cancer: current evidence and future potential. *Trans Cancer Res* (2016) 5(4):410–23. doi: 10.21037/tcr.2016.06.19

20. Limkin EJ, Sun R, Dercle L, Zacharaki EI, Robert C, Reuzé S, et al. Promises and challenges for the implementation of computational medical imaging (radiomics) in oncology. *Ann Oncol Off J Eur Soc Med Oncol* (2017) 28(6):1191–206. doi: 10.1093/annonc/mdx034

21. Sah BR, Owczarczyk K, Siddique M, Cook GJR, Goh V. Radiomics in esophageal and gastric cancer. *Abdominal Radiol (New York)* (2019) 44(6):2048–58. doi: 10.1007/s00261-018-1724-8

22. Liu L, Yi X, Lu C, Qi L, Zhang Y, Li M, et al. Applications of radiomics in genitourinary tumors. *Am J Cancer Res* (2020) 10(8):2293–308.

23. Sjoquist KM, Burmeister BH, Smithers BM, Zalcberg JR, Simes RJ, Barbour A, et al. Survival after neoadjuvant chemotherapy or chemoradiotherapy for resectable oesophageal carcinoma: An updated meta-analysis. *Lancet Oncol* (2011) 12(7):681–92. doi: 10.1016/S1470-2045(11)70142-5

24. Cheng L, Wu L, Chen S, Ye W, Liu Z, Liang C. [CT-based radiomics analysis for evaluating the differentiation degree of esophageal squamous carcinoma]. *Zhong nan da xue xue bao Yi xue ban = J Cent South Univ Med Sci* (2019) 44 (3):251–6. doi: 10.11817/j.issn.1672-7347.2019.03.004

25. Wu L, Wang C, Tan X, Cheng Z, Zhao K, Yan L, et al. Radiomics approach for preoperative identification of stages I-II and III-IV of esophageal cancer. *Chin J Cancer Res = Chung-kuo yen cheng yen chiu* (2018) 30(4):396–405. doi: 10.21147/j.issn.1000-9604.2018.04.02

26. Shen C, Liu Z, Wang Z, Guo J, Zhang H, Wang Y, et al. Building CT radiomics based nomogram for preoperative esophageal cancer patients lymph node metastasis prediction. *Trans Oncol* (2018) 11(3):815–24. doi: 10.1016/j.tranon.2018.04.005

27. Xie C, Yang P, Zhang X, Xu L, Wang X, Li X, et al. Sub-Region based radiomics analysis for survival prediction in oesophageal tumours treated by definitive concurrent chemoradiotherapy. *EBioMedicine* (2019) 44:289–97. doi: 10.1016/j.ebiom.2019.05.023

28. Greene FL, Page DL, Fleming ID, Fritz A, Balch CM, Haller DG, et al. *AJCC cancer staging manual (6th edition). 6 edition*. New York: Springer (2002). pp. 91–8.

29. Cox JD, Stetz J, Pajak TF. Toxicity criteria of the radiation therapy oncology group (RTOG) and the European organization for research and treatment of cancer (EORTC). *Int J Radiat oncology biology physics* (1995) 31(5):1341–6. doi: 10.1016/0360-3016(95)00060-C

30. Zwanenburg A, Vallières M, Abdalah MA, Aerts HJWL, Andrearczyk V, Apte A, et al. The image biomarker standardization initiative: Standardized quantitative radiomics for high-throughput image-based phenotyping. *Radiology* (2020) 295(2):328–38. doi: 10.1148/radiol.2020191145

31. Amadasun MaK R. Textural features corresponding to textural properties. *IEEE Trans Systems Man Cybernetics* (1989) 19:1264–74. doi: 10.1109/21.44046

32. Sun C, Wee WG. Neighboring gray level dependence matrix for texture classification. *Comput Gr Image Process* (1983) 23:341–52. doi: 10.1016/0734-189X(83)90032-4

33. Thibault G, Angulo J, Meyer F. Advanced statistical matrices for texture characterization: Application to cell classification. *IEEE Trans BioMed Eng* (2014) 61(3):630–7. doi: 10.1109/TBME.2013.2284600

34. Galloway MM. Texture analysis using gray level run lengths. *Comput Graphics Image Process* (1975) 4(2):172–9. doi: 10.1016/S0146-664X(75)80008-6

35. Zhai TT, van Dijk LV, Huang BT, Lin ZX, Ribeiro CO, Brouwer CL, et al. Improving the prediction of overall survival for head and neck cancer patients using image biomarkers in combination with clinical parameters. *Radiotherapy oncology: J Eur Soc Ther Radiol Oncol* (2017) 124(2):256–62. doi: 10.1016/j.radonc.2017.07.013

36. Zeng C, Zhai T, Chen J, Guo L, Huang B, Guo H, et al. Imaging biomarkers of contrast-enhanced computed tomography predict survival in oesophageal cancer after definitive concurrent chemoradiotherapy. *Radiat Oncol (London England)* (2021) 16(1):8. doi: 10.1186/s13014-020-01699-w

37. Kramer AA, Zimmerman JE. Assessing the calibration of mortality benchmarks in critical care: The hosmer-lemeshow test revisited. *Crit Care Med* (2007) 35(9):2052–6. doi: 10.1097/01.CCM.0000275267.64078.B0

38. Minsky BD, Pajak TF, Ginsberg RJ, Pisansky TM, Martenson J, Komaki R, et al. INT 0123 (Radiation therapy oncology group 94-05) phase III trial of combined-modality therapy for esophageal cancer: high-dose versus standard-dose radiation therapy. *J Clin Oncol: Off J Am Soc Clin Oncol* (2002) 20(5):1167–74. doi: 10.1200/JCO.2002.20.5.1167

39. Muijs CT, Beukema JC, Mul VE, Plukker JT, Sijtsema NM, Langendijk JA. External beam radiotherapy combined with intraluminal brachytherapy in esophageal carcinoma. *Radiothe Oncol J Eur Soc Ther Radiol Oncol* (2012) 102 (2):303–8. doi: 10.1016/j.radonc.2011.07.021

40. Rishi A, Zhang GG, Yuan Z, Sim AJ, Song EY, Moros EG, et al. Pretreatment CT and (18) f-FDG PET-based radiomic model predicting pathological complete response and loco-regional control following neoadjuvant chemoradiation in oesophageal cancer. *J Med Imaging Radiat Oncol* (2021) 65(1):102–11. doi: 10.1111/1754-9485.13128

41. Kao YS, Hsu Y. A meta-analysis for using radiomics to predict complete pathological response in esophageal cancer patients receiving neoadjuvant chemoradiation. *In Vivo (Athens Greece)* (2021) 35(3):1857–63. doi: 10.21873/invivo.12448

42. Chen LL, Nolan ME, Silverstein MJ, Mihm MC, Sober AJ, Tanabe KK, et al. The impact of primary tumor size, lymph node status, and other prognostic factors on the risk of cancer death. *Cancer* (2009) 115(21):5071–83. doi: 10.1002/cncr.24565

43. Leijenaar RTH, Carvalho S, Hoebers FJP, Aerts HJWL, van Elmpt WJC, Huang SH, et al. External validation of a prognostic CT-based radiomic signature in oropharyngeal squamous cell carcinoma. *Acta Oncol* (2015) 54(9):1423–9. doi: 10.3109/0284186X.2015.1061214

44. Huang Y-Q, Liang C-H, He L, Tian J, Liang C-S, Chen X, et al. Development and validation of a radiomics nomogram for preoperative prediction of lymph node metastasis in colorectal cancer. *J Clin Oncol Off J Am Soc Clin Oncol* (2016) 34 (18):2157–64. doi: 10.1200/JCO.2015.65.9128

45. van Rossum PSN, Fried DV, Zhang L, Hofstetter WL, van Vulpen M, Meijer GJ, et al. The incremental value of subjective and quantitative assessment of 18F-FDG PET for the prediction of pathologic complete response to preoperative chemoradiotherapy in esophageal cancer. *J Nucl Med* (2016) 57(5):691–700. doi: 10.2967/jnumed.115.163766

46. Jiang Y, Chen C, Xie J, Wang W, Zha X, Lv W, et al. Radiomics signature of computed tomography imaging for prediction of survival and chemotherapeutic benefits in gastric cancer. *EBioMedicine* (2018) 36:171–82. doi: 10.1016/j.ebiom.2018.09.007

47. Hong D, Zhang L, Xu K, Wan X, Guo Y. Prognostic value of pre-treatment CT radiomics and clinical factors for the overall survival of advanced (IIIB-IV) lung adenocarcinoma patients. *Front Oncol* (2021) 11:628982. doi: 10.3389/fonc.2021.628982

48. Kim JW, Kim TH, Kim JH, Lee IJ. Predictors of post-treatment stenosis in cervical esophageal cancer undergoing high-dose radiotherapy. *World J Gastroenterol* (2018) 24(7):862–9. doi: 10.3748/wjg.v24.i7.862

49. Katada C, Muto M, Manabe T, Boku N, Ohtsu A, Yoshida S. Esophageal stenosis after endoscopic mucosal resection of superficial esophageal lesions. *Gastrointest Endosc* (2003) 57(2):165–9. doi: 10.1067/mge.2003.73

50. Straub JM, New J, Hamilton CD, Lominska C, Shnayder Y, Thomas SM. Radiation-induced fibrosis: mechanisms and implications for therapy. *J Cancer Res Clin Oncol* (2015) 141(11):1985–94. doi: 10.1007/s00432-015-1974-6

51. Ahlberg A, al-Abany M, Alevronta E, Friesland S, Hellborg H, Mavroidis P, et al. Esophageal stricture after radiotherapy in patients with head and neck cancer: experience of a single institution over 2 treatment periods. *Head Neck* (2010) 32 (4):452–61. doi: 10.1002/hed.21201

52. Abu-Ghanem S, Sung CK, Junlapan A, Kearney A, DiRenzo E, Dewan K, et al. Endoscopic management of postradiation dysphagia in head and neck cancer patients: A systematic review. *Ann Otol Rhinol Laryng* (2019) 128(8):767–73. doi: 10.1177/0003489419837565

53. Agarwalla A, Small AJ, Mendelson AH, Scott FI, Kochman ML. Risk of recurrent or refractory strictures and outcome of endoscopic dilation for radiation-induced esophageal strictures. *Surg Endosc* (2015) 29(7):1903–12. doi: 10.1007/s00464-014-3883-1

54. Ng TM, Spencer GM, Sargeant IR, Thorpe SM, Bown SG. Management of strictures after radiotherapy for esophageal cancer. *Gastrointest Endosc* (1996) 43 (6):584–90. doi: 10.1016/s0016-5107(96)70196-7

55. Xie CY, Pang CL, Chan B, Wong EY, Dou Q, Vardhanabhuti V. Machine learning and radiomics applications in esophageal cancers using non-invasive imaging methods-a critical review of literature. *Cancers* (2021) 13(10). doi: 10.3390/cancers13102469

56. Li M, Zhang X, Zhao F, Luo Y, Kong L, Yu J. Involved-field radiotherapy for esophageal squamous cell carcinoma: theory and practice. *Radiat Oncol (London England)* (2016) 11:18. doi: 10.1186/s13014-016-0589-7

57. Fan C-Y, Su Y-F, Huang W-Y, Chao H-L, Lin K-T, Lin C-S. Definitive radiotherapy dose escalation with chemotherapy for treating non-metastatic oesophageal cancer. *Sci Rep* (2018) 8(1):12877. doi: 10.1038/s41598-018-31302-y

58. Yu W, Cai X-W, Liu Q, Zhu Z-F, Feng W, Zhang Q, et al. Safety of dose escalation by simultaneous integrated boosting radiation dose within the primary tumor guided by (18)FDG-PET/CT for esophageal cancer. *Radiotherapy Oncol J Eur Soc Ther Radiol Oncol* (2015) 114(2):195–200. doi: 10.1016/j.radonc.2014.12.007

59. Abbasi M, El Hanandeh A. Forecasting municipal solid waste generation using artificial intelligence modelling approaches. *Waste Manage* (2016) 56:13–22. doi: 10.1016/j.wasman.2016.05.018

60. Nguyen XC, Nguyen TTH, La DD, Kumar G, Rene ER, Nguyen DD, et al. Development of machine learning - based models to forecast solid waste generation in residential areas: a case study from Vietnam. *Resour Conserv Recycling* (2021) 167:105381. doi: 10.1016/j.resconrec.2020.105381

frontiers | Frontiers in Oncology

TYPE Original Research
PUBLISHED 04 January 2023
DOI 10.3389/fonc.2022.1059874

OPEN ACCESS

EDITED BY
Damiano Caruso,
Sapienza University of Rome, Italy

REVIEWED BY
Paolo Tini,
Siena University Hospital, Italy
Huan Zhang,
Shanghai Jiao Tong University, China

*CORRESPONDENCE
Bin Dong
dongbin@math.pku.edu.cn
Xiaotian Zhang
zhangxiaotianmed@163.com
Lei Tang
tangl@bjcancer.org
Lin Shen
shenlin@bjmu.edu.cn

†These authors have contributed equally to this work and share first authorship

‡These authors have contributed equally to this work and share corresponding authorship

SPECIALTY SECTION
This article was submitted to Gastrointestinal Cancers: Gastric and Esophageal Cancers, a section of the journal Frontiers in Oncology

RECEIVED 02 October 2022
ACCEPTED 29 November 2022
PUBLISHED 04 January 2023

CITATION
Li J, Chen Z, Chen Y, Zhao J, He M, Li X, Zhang L, Dong B, Zhang X, Tang L and Shen L (2023) CT-based delta radiomics in predicting the prognosis of stage IV gastric cancer to immune checkpoint inhibitors. *Front. Oncol.* 12:1059874. doi: 10.3389/fonc.2022.1059874

CT-based delta radiomics in predicting the prognosis of stage IV gastric cancer to immune checkpoint inhibitors

Jiazheng Li[1†], Zifan Chen[2†], Yang Chen[3], Jie Zhao[4], Meng He[1], Xiaoting Li[1], Li Zhang[2], Bin Dong[5*‡], Xiaotian Zhang[3*‡], Lei Tang[1*‡] and Lin Shen[3*‡]

[1]Department of Radiology, Key Laboratory of Carcinogenesis and Translational Research (Ministry of Education), Peking University Cancer Hospital and Institute, Beijing, China, [2]Center for Data Science, Peking University, Beijing, China, [3]Department of Gastrointestinal Oncology, Key Laboratory of Carcinogenesis and Translational Research (Ministry of Education), Peking University Cancer Hospital and Institute, Beijing, China, [4]National Engineering Laboratory for Big Data Analysis and Applications, Peking University, Beijing, China, [5]Beijing International Center for Mathematical Research (BICMR), Peking University, Beijing, China

Introduction: To explore the prognostic value of CT-based delta radiomics in predicting the prognosis of patients with stage IV gastric cancer treated with immune checkpoint inhibitors (ICI).

Materials and methods: Forty-two patients with stage IV gastric cancer, who had received ICI monotherapy, were enrolled in this retrospective study. Baseline and first follow-up CT scans were analyzed. Intratumoral and peritumoral regions of interest (ROI) were contoured, enabling the extraction of 192 features from each ROI. The intraclass correlation coefficients were used to select features with high stability. The least absolute shrinkage and selection operator was used to select features with high weights for predicting patient prognosis. Kaplan–Meier analysis and log-rank test were performed to explore the association between features and progression free survival (PFS). Cox regression analyses were used to identify predictors for PFS. The C-index was used to assess the prediction performance of features.

Results: Two radiomics features of ΔVintra_ZV and postVperi_Sphericity were identified from intratumoral and peritumoral regions, respectively. The Kaplan–Meier analysis revealed significant differences in PFS between patients with low and high feature value (ΔVintra_ZV: P=0.000; postVperi_Sphericity: P=0.012), and the multivariable cox analysis demonstrated that ΔVintra_ZV was independent predictor for PFS (HR, 1.911; 95% CI: 1.163–3.142; P=0.011), with C-index of 0.705.

Conclusions: Based on CT scans at baseline and first follow-up, the delta radiomics features could efficiently predict the PFS of gastric cancer patients treated with ICI therapy.

KEYWORDS

immunotherapy, gastric cancer, prognosis, radiomics, computed tomography

Introduction

Gastric cancer is one of the malignancies with high mortality rate (1). Despite significant efforts to develop innovative treatment techniques based on cytotoxic chemotherapy, targeted therapy, and radiotherapy, a significant proportion of gastric cancer patients will still demonstrate poor response to conventional therapies or even fast progression after treatment (2). Immune checkpoint inhibitors (ICIs) have revolutionized the treatment of a variety of malignancies, including gastric cancer (3). More specifically, several large multicenter clinical trials demonstrated a significant and durable survival benefit in refractory gastric cancer patients who received ICI therapy, with a duration of response ranging from 8.4 to 9.5 months (3, 4). However, treatment response varied significantly as 60% of patients derived no benefit from ICI therapy, and 21% of patients even showed hyperprogression during treatment (2, 3, 5). Therefore, there is an urgent need for the introduction of precise biomarkers that can predict the response of gastric cancer to ICI at the early treatment stage.

Several predictive tumor biomarkers from biopsy tissue samples could indicate ICI treatment response and prognosis of gastric cancer patients (6), such as positivity of programmed death-ligand 1 (PD-L1), mismatch repair deficiency (dMMR), and Epstein–Barr virus (EBV) (6, 7). However, most patients tested negative for the above-mentioned biomarkers, e.g., 86% of patients with PD-L1 combined positive scores (CPS)<1, 78.4-92.5% of patients with mismatch repair proficiency (pMMR), and 91% of patients with negative EBV according to previous studies (3, 5, 8, 9). Some of these biomarkers predicted that patients with poor treatment response could still respond well to ICI therapy, with reported objective response rates of approximately 6.4-10.9% for PD-L1 CPS < 1, 12.3% for pMMR, and 16.4% for negative EBV, respectively (3, 6, 7). Besides, not all laboratories have the available resources to perform complex immunohistochemistry protocols that are necessary to identify or evaluate potential tumor biomarkers, hindering their subsequent application in clinical practice (10, 11). In addition, given the spatial heterogeneity of gastric cancer, biopsy samples may not always be evaluated appropriately.

Computed tomography (CT) has been widely and routinely used in clinical practice, yet traditional unidimensional measurements made both RECIST and iRECIST criteria no longer meet the needs of the ICI response evaluation and hindered the realization of the precision medicine (12). Radiomics is a useful tool to mine data from radiographic images, such as tumor texture characteristics, which may not be detectable by 'naked-eye' inspection (13). Several studies have verified that radiomics could predict response to neoadjuvant chemotherapy and palliative chemotherapy in patients with gastric cancer, with an area under the curve (AUC) of 0.74-0.82 (14–16). Recently, one study explored the response prediction performance of baseline CT radiomics in patients treated with immunotherapy combined with chemotherapy and showed promising results, with an AUC over 0.7 (17). To the best of our knowledge, the prognostic value of radiomics features in patients with gastric cancer treated with ICI monotherapy has not been elucidated. Therefore, this study aimed to use delta radiomics to extract information from CT scans (at baseline and first follow-up) and predict the survival of patients with stage IV gastric cancer treated by ICI.

Materials and methods

Patients

This study was performed in line with the principles of the Declaration of Helsinki. Written informed consent of this retrospective study was waived. Data from 101 consecutive patients with stage IV gastric cancer who had received anti-programmed cell death protein 1/programmed cell death ligand 1 (PD-1/PD-L1) antibody alone or in combination with anti-cytotoxic T lymphocyte-associated antigen 4 (CTLA-4) antibody were collected in the Peking University Cancer Hospital, Beijing, China, between 2016 and 2020. Inclusion criteria were as follows: (a) histologically confirmed gastric adenocarcinoma; (b) patients treated with ICI monotherapy (anti-PD-1/PD-L1 alone or in combination with anti-CTLA-4 antibodies); (c) availability of baseline enhanced abdominal/pelvic CT scans performed <30 days before ICI treatment; (d) availability of the first follow-up enhanced abdominal/pelvic CT scans two to three cycles after ICI treatment initiation. Exclusion criteria were as follows: (a) patients with primary gastric surgical treatment (n=53) (b) patients with other synchronous or metachronous malignant neoplasms (n=4); (c) thickness of primary gastric lesions <10mm on CT (n=1); (d) CT images with obvious artifacts (n=1). Finally, 42 patients were included in our study. The following clinicopathological data were retrospectively collected from patients' medical records: age, gender, Eastern Cooperative Oncology Group performance status score (ECOG PS), treatment regimen, treatment cycles of ICI before first follow-up, Lauren subtype, degree of differentiation, PD-L1 status, MMR status, EBV status, peritoneal metastasis, hepatic metastasis, the number of metastatic sites. We registered patients with PD-L1 CPS ≥ 1 as PD-L1 positive cases (4). The flowchart is shown in Figure 1.

Treatment regimens and follow-up protocol

There were 29 patients received anti-PD-1/PD-L1 treatment alone, including seven patients received GLS-010 (zimberelimab)

(240mg d1 d15 Q28d), six patients received CS1003 (nofazinlimab) (200mg d1 Q21d), four patients received toripalimab (3mg/kg d1 d15 Q28d), three patients received BGB-A317 (tislelizumab) (200mg d1 Q21d), three patients received pembrolizumab (200mg d1 Q14d), two patients received atezolizumab (1200mg d1 Q21d), two patients received MSB2311 (20mg/kg d1 Q21d), one patients received LZM009 (432mg d1 Q28d) and one patients received Sintilimab (200mg d1 Q21d). There were 13 patients received anti-PD-1 in combination with anti-CTLA-4 treatment, including seven patients received Sintilimab + IBI310 (Sintilimab 200mg d1 Q21d, IBI310 68mg d1 Q42d) and six patients received Nivolumab + Ipilimumab (Nivolumab 1mg/kg d1, d22 Q42d, Ipilimumab 3mg/kg d1 d22 Q42d).

All patients conducted follow-up every two to three cycles of ICI treatment, including enhanced abdominal/pelvic CT scans until the resistance to ICI therapy. PFS was defined as the time from the start of ICI treatment to disease progression, death from any cause, or the cutoff date of November 12, 2021. Patients without any progression or death at the end of the follow-up period were censored.

CT examination

All patients underwent abdominal/pelvic contrast-enhanced CT examinations after fasting for more than eight hours. 10 mg anisodamine (654-2, Hangzhou Minsheng Pharma) was administered intramuscularly to reduce gastrointestinal motility before CT examination. Next, 6g gas-producing crystals with 10ml warm water were given orally shortly before the examination. All patients underwent a quick respiratory training session to prevent potential respiratory artifacts. The CT scanner was either the LightSpeed 64 VCT or the Discovery CT750 HD, with a peak tube voltage of 120 kVp, an automatic tube current-time product, a collimation thickness of 64 x 0.625 mm, a helical pitch of 0.984:1, 5-mm scanning thickness, and 0.625-mm reconstructed thickness. Patients were scanned in the supine position, and scan coverage started from the diaphragmatic dome until 2cm below the lower margin of symphysis ossium pubis. All patients were injected with nonionic contrast material through the antecubital vein at a rate of 3.5ml/s (1.5ml/kg of body weight, iohexol 300mg I/ml, Omnipaque, GE Healthcare). Arterial and venous phase scanning were performed at 40s and 70s, respectively, following contrast media injection.

Image analysis and segmentation

Baseline and first follow-up CT scans in arterial and venous phases were analyzed by two radiologists with 20 and 3 years of experience in gastrointestinal CT interpretation, respectively (TL and LJZ). Both radiologists were blinded to the clinical and histopathological information. However, they did know the anatomical location of gastric cancer. Two intratumoral regions of interest (ROI) were manually contoured–one ROI for the arterial phase and another ROI for the venous phase–on the largest area of the gastric lesions (axial plane) using the ITK-SNAP software (v.3.6.0, http://www.itksnap.org). To capture peritumoral information, the slice image was uniformly interpolated to 0.6 mm per pixel, and a peripheral ring was then created automatically by dilating the tumor boundaries by 7 pixels (4.2mm) on the outside and shrinking by 7 pixels (4.2mm) on the inside (18). Secondly, the modification was conducted manually on the pre-modified peripheral ring to exclude the gastric cavity and the area covering the surrounding organs and large vessels (Figure 2).

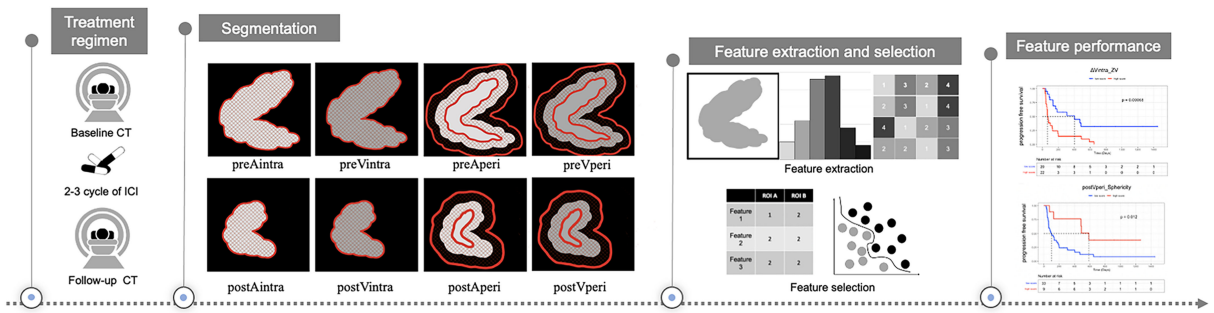

FIGURE 1
Study design for the evaluation of response prediction to immune checkpoint inhibitors in stage IV gastric cancer patients based on radiomics features. preAintra: intratumoral regions on baseline atrial phase; preVintra: intratumoral regions on baseline venous phase, preAperi: peritumoral regions on baseline atrial phase; preVperi: peritumoral regions on baseline venous phase; postAintra: intratumoral regions on follow-up atrial phase; postVintra: intratumoral regions on follow-up venous phase; postAperi: peritumoral regions on follow-up atrial phase; postVperi: peritumoral regions on follow-up venous phase.

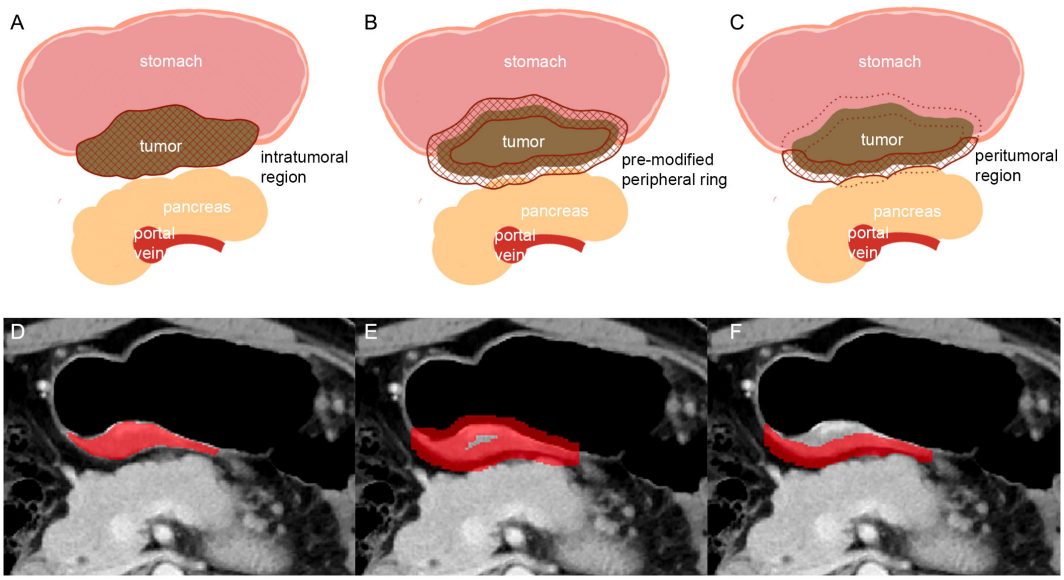

FIGURE 2
Schematic illustration of the steps followed to draw intratumoral and peritumoral ROIs. **(A, D)**: the largest axial sections of gastric lesions were manually contoured (intratumoral region of ROI). **(B, E)**: the pre-modified peripheral ring was automatically generated. **(C, F)**: modifying was conducted manually on the pre-modified peripheral ring to exclude the gastric cavity and the part covering the surrounding organs (pancreas) and large vessels (in C: solid line: peritumoral region of ROI; dotted line: the part of ROI been deleted).

Feature extraction and selection

First, we uniformly resampled the CT image and its ROI annotation so that the spacing parameters in the x-, y-, and z-axis were 0.6, 0.6, and 5.0, respectively. The texture features were extracted from each ROI of each patient's CT image using the open-source python platform Pyradiomics (version 2.1.2, https://pyradiomics.readthedocs.io/en/latest/#). We extracted a total of 192 features for each ROI, including eight shape features, 36 first-order statistics, 46 gray level co-occurrence matrices, 32 gray level run length matrices, 32 gray level size zone matrices, 28 gray level dependence matrices, and ten neighboring gray tone difference matrices. Eight sets of radiomics features were derived from intratumoral and peritumoral regions at baseline arterial and venous phases, and follow-up CT scans, including features from intratumoral regions at baseline atrial phase (preAintra), intratumoral regions at baseline venous phase (preVintra), peritumoral regions at baseline atrial phase (preAperi), peritumoral regions at baseline venous phase (preVperi), intratumoral regions at follow-up atrial phase (postAintra), intratumoral regions at follow-up venous phase (postVintra), peritumoral regions at follow-up atrial phase (postAperi), and peritumoral regions at follow-up venous phase (postVperi). Calculate the changes between baseline and follow-up features by subtracting the values of CT features of follow-up and baseline, which provided four corresponding sets of delta features (ΔAintra, ΔVintra, ΔAperi, and ΔVperi).

All radiomics features were standardized by subtracting the mean value and dividing by the standard deviation. Intraclass correlation coefficients (ICCs) based on a multiple-raters, two-way random-effects model were calculated to assess the stability and reproducibility of radiomic features within groups. To ensure reliability for all twelve sets of radiomics features, we only reserved radiomic features with ICC estimates > 0.80, and further selection was then conducted in the data obtained by TL. Furthermore, we used the Cox proportional hazards regression method with the least absolute shrinkage and the selection operator (LASSO) penalty with four-fold cross-validation to select the most useful predictive features from intratumoral and peritumoral regions, respectively (19). Since the total patient number was limited, the most significant nonzero feature in intratumoral and peritumoral regions was selected to avoid overfitting.

Statistical analysis

Continuous variables were presented as the mean with standard deviation (SD) or median with interquartile ranges (IQR) based on normal distribution or not. Categorical variables were shown as numbers with percentages. PFS was estimated using the Kaplan–Meier method, and the log-rank test was employed to compare differences in survival probability. The Cox proportional hazards model was used for univariate and

multivariate analyses. *P* values less than 0.10 in univariate analysis were subsequently included in the multivariate analyses where enter feature selection was used. Harrell's concordance index (C-index) was calculated to evaluate prognostic ability. Statistical analysis was conducted using R software (R 4.0.4, The R Foundation for Statistical Computing, Vienna, Austria). All statistical tests were two-sided, and a value of $P<0.05$ was considered significant.

Results

Patient characteristics

A total of 42 patients were included in this study. The median follow-up time and the median time for PFS were 736 (IQR: 656, 1266) and 133 (IQR: 61, 483) days, respectively. The patients' clinicopathological data are summarized in Table 1. Univariate analysis revealed that age and Lauren type were associated with PFS. In contrast, other clinicopathological characteristics were not found to have a prognostic impact. The K–M analysis showed that older patients (>62 years, median value) had more prolonged PFS compared to younger patients [median PFS time: younger patients, 92 (IQR: 45, 165) days; older patients, 483 (IQR: 73, not reached) days; P=0.001]. Patients with intestinal-type gastric cancer showed more prolonged PFS than patients with a different Lauren type [median PFS time: intestinal type, 195 (IQR: 100, 649) days, reference; diffuse type, 63 (IQR: 45, 92) days, *P* =0.003; mixed type, 127 (IQR: 54, 134) days, *P*=0.087].

Radiomics feature selection

A three-step radiomics feature selection procedure was applied. In the first step, 2304 radiomics features were extracted from twelve sets of features. Consequently, 99 features were further enrolled with ICC>0.80 as a reliability standard, including 70 intratumoral features (preAintra: 14; preVintra: 25; postAintra: 8; postVintra:13; ΔAintra: 2, ΔVintra: 8) and 29 peritumoral features (preAperi: 5; preVperi: 8; postAperi: 7; postVperi: 8; ΔAperi: 0, ΔVperi: 1). The third step involved the selection of features with the highest coefficient based on the Lasso COX method, which included ΔVintra_original_glszm_Zone Variance (ΔVintra_ZV) from the intratumoral regions and postVperi_original_shape_Sphericity (postVperi_Sphericity) from the peritumoral regions.

Radiomics feature analysis

The optimal cut-off values were -0.09 and 0.88 for ΔVintra_ZV and postVperi_Sphericity determined by X-tile (version 3.6.1), respectively. The K–M analysis suggested that the PFS of stage IV gastric cancer patients with a high ΔVintra_ZV value (> cutoff value) was worse than that of patients with a low value (≤ cutoff value), with a median PFS of 402 *vs*. 64 days (*P*=0.000, log-rank test). The PFS of stage IV gastric cancer patients with a low postVperi_Sphericity value was worse than that of patients with a high value, with a median PFS of 100 *vs*. 589 days (*P*=0.012, log-rank test) (Figure 3). We performed additional analyses within subgroups of gastric cancer patients who had either not been tested or had already tested negative for biomarkers, including PD-L1, MMR, and EBV. Our findings revealed that ΔVintra_ ZV and postVperi Sphericity could stratify patients in all three subgroups according to their PFS (Figures 4A–F).

ΔVintra_ZV and postVperi_Sphericity were both significant in univariate analysis (hazard ratio [HR], 2.320; 95% confidence interval [CI]: 1.478–3.641, *P*=0.000; HR, 0.601; 95% CI: 0.410–0.882, *P*=0.009). After controlling for age, Lauren type, peritoneal metastasis, and number of metastatic sites, ΔVintra_ZV were still independent predictor of survival (HR, 1.911; 95% CI: 1.163–3.142; *P*=0.011). However, postVperi_Sphericity had no association with PFS (HR, 0.690; 95% CI: 0.421–1.132; *P*=0.142). ΔVintra_ ZV and postVperi_Sphericity yielded a C-index of 0.705 (95% CI: 0.625–0.785) and 0.632 (95% CI: 0.528–0.736), respectively.

Discussion

This study initially explored the relationship between delta radiomics with the prognosis of patients with stage IV gastric cancer receiving ICI. Our findings revealed that ΔVintra_ZV and postVperi_Sphericity from the intratumoral and peritumoral regions, respectively, could classified patients with survival outcomes and ΔVintra_ZV was the independent predictor for PFS.

Previous studies have reported that on-treated tumor samples of patients with effective ICI response showed increased immune cell abundance and a low percentage of tumor cells (20, 21). A previous study explored the association between radiomics features in pan-cancer and CD8 cell abundance within the tumor. The relatively homogeneous tumors were associated with increased pre-existing CD8+ cell infiltration and better prognosis; in contrast, tumors composed of highly proliferating tumor cells exhibited a more heterogeneous radiomics texture (22). In our study, the low ΔVintra_ZV score indicated that the texture of gastric lesions changed from heterogeneous to homogenous and thus were more likely to be observed in patients with prolonged survival after ICI treatment. We hypothesized that this change may indicate immune cell infiltration and good tumor response to ICI therapy, whereas texture changes towards non-uniformity may indicate a high extent of tumor cell proliferation and

TABLE 1 The clinicopathological characteristics of the included patients.

Characteristics	Total (n=42)	Univariate analysis		Multivariate analysis	
		HR (95%CI)	*P* value	HR (95%CI)	*P* value
Age (years), (median [IQR])	62.00 (12.00)	0.943 (0.915–0.972)	0.000*	0.972 (0.936–1.008)	0.129
Gender, n (%)		0.534 (0.257–1.112)	0.094		
Male	31(73.814%)				
Female	11(26.19%)				
ECOG PS, n (%)		0.658 (0.353–1.223)	0.186		
0	20 (47.628%)				
1 +–2	22 (52.3852%)				
Treatment regimen, n (%)		0.797 (0.359–1.769)	0.576		
Anti-PD-1/PD-L1	29 (69.04%)				
Anti-PD-1 + anti-CTLA-4	13 (30.95%)				
Treatment cycle, n (%)		1.229 (0.820–1.844)	0.318		
Two cycles	33 (78.57%)				
Three cycles	9 (21.43%)				
Lauren type, n (%)					
Intestinal	19 (45.23%)	[reference]		[reference]	
Diffuse	11 (26.19%)	3.629 (1.553–8.478)	0.003*	3.155 (1.203–8.275)	0.020*
Mixed	7 (16.677%)	2.370 (0.883–6.362)	0.087	1.924 (0.668–5.540)	0.225
No testing	5 (11.9012%)	0.570 (0.161–2.026)	0.385	0.409 (0.087–1.933)	0.259
Differentiation, n (%)		1.157 (0.578–2.317)	0.680		
Moderate	17 (40.481%)				
Poor	25 (59.5260%)				
PD-L1, n (%)					
Negative	12 (28.579%)	[reference]			
Positive	17 (40.48%)	0.520 (0.228–1.185)	0.119		
No testing	13 (30.951%)	0.604 (0.256–1.427)	0.250		
MMR, n (%)					
pMMR	33 (78.579%)	[reference]			
dMMR	4 (9.5210%)	0.296 (0.069–1.279)	0.103		
No testing	5 (11.902%)	2.282 (0.836–6.227)	0.107		
EBV, n (%)					
Negative	23 (54.765%)	[reference]			
Positive	12 (28.579%)	0.875 (0.361–2.122)	0.768		
No testing	7 (16.677%)	2.103 (0.834–5.310)	0.115		
peritoneal metastasis, n (%)		0.513 (0.254–1.036)	0.063	1.187 (0.469–3.007)	0.717
Present	20 (47.62%)				
Absent	22 (52.38%)				
Hepatic metastasis, n (%)		1.263 (0.616–2.589)	0.524		
Present	15 (35.71%)				
Absent	27 (64.29%)				
Number of metastatic sites, n (%)					
1	7 (16.67%)	[reference]		[reference]	

(Continued)

TABLE 1 Continued

Characteristics	Total (n=42)	Univariate analysis		Multivariate analysis	
		HR (95%CI)	*P* value	HR (95%CI)	*P* value
2	29 (69.05%)	1.640 (0.566–4.755)	0.362	2.022 (0.546–7.481)	0.292
3+	6 (14.29%)	3.431 (0.955–12.321)	0.059	4.881 (0.884–26.939)	0.069
ΔVintra_ZV, (median [IQR])	-0.07 (0.54)	2.320 (1.478 – 3.641)	0.000*	1.911 (1.163–3.142)	0.011*
postVperi_Sphericity, mean (SD)	0.00 (1.00)	0.601 (0.410 – 0.882)	0.009*	0.690 (0.421–1.132)	0.142

IQR, interquartile ranges; HR, hazard ratio; CI, confidence interval; ECOG PS, Eastern Cooperative Oncology Group performance status score; PD-1, programmed cell death protein 1; PD-L1, programmed cell death ligand 1; MMR, mismatch repair; dMMR, mismatch repair deficiency; pMMR, mismatch repair proficiency; EBV, Epstein–Barr virus.

resistance to ICI. Similar to our results, Basler et al. also suggested that the changes in the CT texture of metastatic melanoma from heterogeneity to homogeneity during ICI treatment are more likely to represent pseudoprogression, whereas changes from homogeneity to heterogeneity may indicate true tumor progression (23). Accordingly, patients with pseudoprogression showed longer survival compared with patients with true progression (23).

Given the dynamic change of tumor-immune interactions, biomarkers capable of tracking tumor evolution during the treatment course may provide more information on patients' prognoses. A previous histological study showed that early on-treatment samples were more predictive of the response to ICI compared to the mere assessment of baseline samples (20). Although biopsies provide a method to capture the dynamic change of tumors, invasive re-biopsy may not be frequently conducted in real-world clinical practice. In our study, both predictors, ΔVintra_ ZV and postVperi_ Sphericity, incorporated post-treatment CT texture features and could predict the response of patients receiving ICI. Consistently, Khorrami et al. developed radiomics models to predict the ICI response and OS of patients with non–small cell lung cancer (NSCLC). The results showed that the performance of models combining baseline and follow-up features was better than the baseline radiomics model alone (21). Similar results also have been reported in patients treated with radiation therapy and chemotherapy (24, 25).

Khorrami et al. have shown that the ICI response prediction performance of combined radiomics from intra- and peritumoral regions in NSCLC was superior to radiomics from the intratumoral region alone (21). The authors also found that the density of immune infiltration in surgical specimens after ICI was correlated with peritumoral delta radiomics (21). In previous articles, the association between peritumoral radiomics and pathological characteristics of gastric cancer were also studied, but the prediction value of peritumoral radiomics were different (18, 26, 27). Some large-scale studies showed peritumoral radiomics

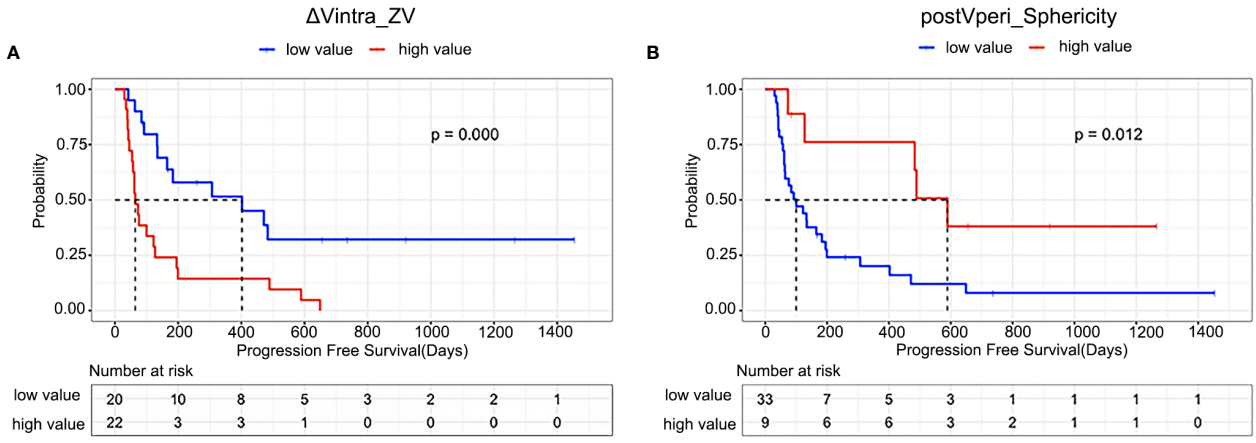

FIGURE 3
Kaplan–Meier estimates of progression-free survival in all patients according to **(A)** ΔVintra_ZV (ΔVintra_original_glszm_Zone Variance); **(B)** postVperi _Sphericity (postVperi_original_shape_Sphericity).

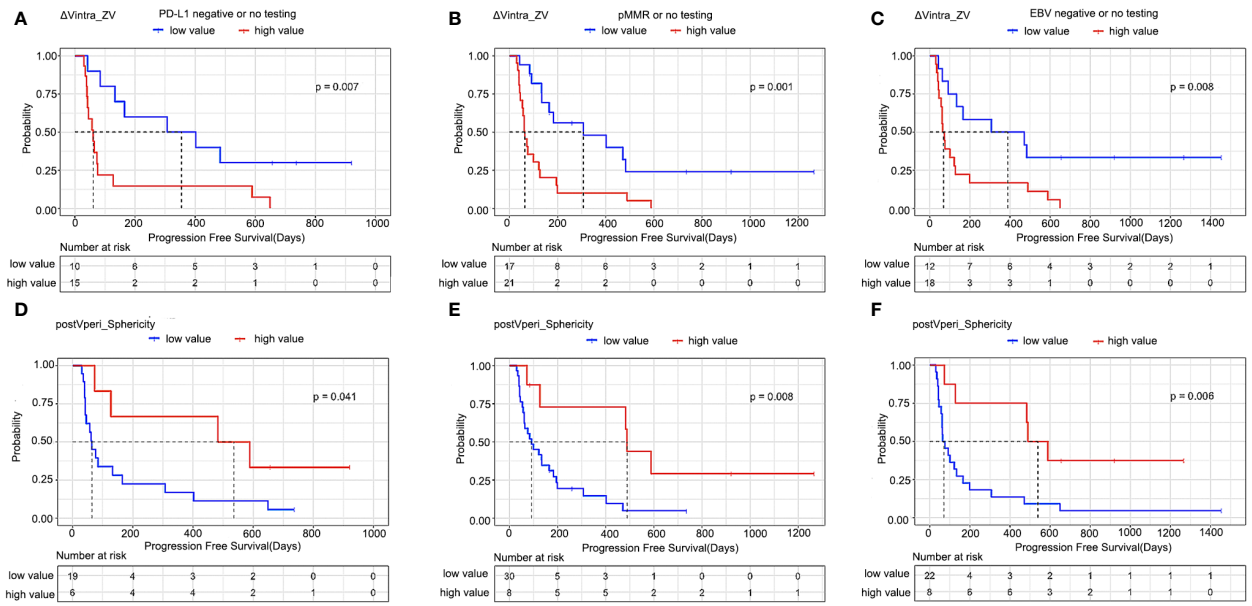

FIGURE 4
Kaplan–Meier estimates of progression-free survival in patients who had either not been tested or had already tested negative for biomarkers. **(A, D)** PD-L1, **(B, E)** MMR, and **(C, F)** EBV according to radiomics features. ΔVintra_ZV, ΔVintra_original_glszm_Zone Variance; postVperi_Sphericity, postVperi_original_shape_Sphericity.

features were one of the important factors to determine the tumor immune microenvironment of gastric cancer and had the prognosis predicting value, while another large-scale study showed peritumoral features may be inapplicable for predicting the Lauren classification of gastric cancer (18, 26, 27). We noticed that the peritumoral ROI in their studies were all a peripheral ring, the same with the peritumoral ROI used in lung cancer (18, 21, 26, 27). However, unlike lung cancer which is surrounded by consistent pulmonary tissue, gastric cancer is usually surrounded by air in the stomach cavity, fat tissue of peritoneum and adjacent organs. We suppose the peritumoral ROI covering air, fat, gastric cancer, and even other organs may influence the precision of information from radiomics features of the peritumoral region, although thickness of ROI around the tumor used in previous studies were smaller than ours. Therefore, in our research, we put effort into modifying the automatically generated peripheral ring, especially deleting the adjacent organs and air covered by the automatically generated ROI. However, unfortunately, such procedure increased the interobserver variability, and only 29 peritumoral features had ICC > 0.80 (70 intratumoral features had ICC > 0.80). Moreover, it was labor-intense to modify the peritumoral ROI of all patients. Taken together, we believe that further research is needed to explore the appropriate method for extracting information from the peritumoral region of gastric cancer.

In our study, patients with a high postVperi_Sphericity score demonstrated a trend towards a more promising survival outcome compared to patients with a low score. Sphericity measured the roundness of the shape and a larger value meant that the shape of ROI resembled a circle (28). Given that all ROIs of the peritumoral area appeared long and narrow, high score of postVperi_ Sphericity could be considered in two aspects, the larger the width and the shorter the length of the ROI. The width of the pre-modified peripheral ring was consistent among different patients (9.4mm in total) when first generated automatically. In patients with low visceral adipose tissue, the pre-modified peripheral ring may cover adjacent organs and thus should be manually modified, contributing to a smaller width. Poor nutritional status, including low visceral fat, has been associated with worse survival outcomes in patients treated with ICI therapy (29, 30). The length of ROI could be regarded as the maximum tumor extension on stomach. Maximum tumor diameter has been proved to be a negative factor for prognosis of patients with gastric cancer (31). Therefore, we considered that a low sphericity score may reflect poor nutritional status and high tumor burden and indicate worse survival after ICI treatment.

Our study has some limitations. First, the sample size of this retrospective study was relatively small. However, the data obtained from patients treated with ICI monotherapy were informative and of great value for assessing response after ICI treatment. In contrast, a combination regimen, such as ICI and chemotherapy, may cause confounding factors. Our study should be considered exploratory. Second, histological biomarker data were unavailable from all patients in this study. Since not all hospitals have accredited laboratories to carry out complex immunohistochemistry

protocols, it is worthwhile to investigate the predictive value of radiomics features in patients who have not been tested or have already tested negative for biomarkers to provide a method of selecting appropriate treatment. Third, pathology confirmation of immune cell infiltration from post-treatment samples was absent. Future studies should aim to evaluate the relationship between radiomics features and immune cell infiltration in post-treatment gastric cancer samples.

Conclusions

Given the complexity of the intrinsic biological pathway of the tumor microenvironment, current biomarkers alone, including PD-L1, dMMR, and EBV status, cannot predict patient prognosis completely. Radiomics features complement these widely accepted histological biomarkers and can be considered candidate biomarkers that can reflect tumor phenotype and provide longitudinal surveillance. Radiomics features have the potential to be used as cost-effective screening tools that can be applied in clinical practice when administering ICI treatment to patients with gastric cancer.

Data availability statement

The raw data supporting the conclusions of this article will be made available by the authors, without undue reservation.

Ethics statement

The studies involving human participants were reviewed and approved by Peking Cancer Hospital. The ethics committee waived the requirement of written informed consent for participation.

Author contributions

JL and ZC contributed equally to this work and share first authorship; BD, XZ, LT, and LS contributed equally to this work and share corresponding authorship. All authors contributed to the article and approved the submitted version.

Funding

This study was funded by Beijing Natural Science Foundation (No. Z180001; Z200015); National Natural Science Foundation of China (No. 81801778, 12090022, 11831002, 91959205); Science Foundation of Peking University Cancer Hospital (JC202301); PKU-Baidu Foundation (No. 2020BD027); Pilot Project of Public Welfare Development Reform of Beijing-based Medical Research Institutes under Grant 2019-1.

Conflict of interest

The authors declare that the research was conducted in the absence of any commercial or financial relationships that could be construed as a potential conflict of interest.

Publisher's note

References

1. Sung H, Ferlay J, Siegel RL, Laversanne M, Soerjomataram I, Jemal A, et al. Global cancer statistics 2020: GLOBOCAN estimates of incidence and mortality worldwide for 36 cancers in 185 countries. *CA Cancer J Clin* (2021) 71:209–49. doi: 10.3322/caac.21660

2. Shitara K, Özgüroğlu M, Bang YJ, Di Bartolomeo M, Mandalà M, Ryu MH, et al. Pembrolizumab versus paclitaxel for previously treated, advanced gastric or gastro-oesophageal junction cancer (KEYNOTE-061): a randomised, open-label, controlled, phase 3 trial. *Lancet* (2018) 392:123–33. doi: 10.1016/S0140-6736(18)31257-1

3. Kang YK, Boku N, Satoh T, Ryu MH, Chao Y, Kato K, et al. Nivolumab in patients with advanced gastric or gastro-oesophageal junction cancer refractory to, or intolerant of, at least two previous chemotherapy regimens (ONO-4538-12, ATTRACTION-2): A randomised, double-blind, placebo-controlled, phase 3 trial. *Lancet* (2017) 390:2461–71. doi: 10.1016/S0140-6736(17)31827-5

4. Fuchs CS, Doi T, Jang RW, Muro K, Satoh T, Machado M, et al. Safety and efficacy of pembrolizumab monotherapy in patients with previously treated advanced gastric and gastroesophageal junction cancer: Phase 2 clinical KEYNOTE-059 trial. *JAMA Oncol* (2018) 4:e180013. doi: 10.1001/jamaoncol.2018.0013

5. Sasaki A, Nakamura Y, Mishima S, Kawazoe A, Kuboki Y, Bando H, et al. Predictive factors for hyperprogressive disease during nivolumab as anti-PD1 treatment in patients with advanced gastric cancer. *Gastric Cancer* (2019) 22:793–802. doi: 10.1007/s10120-018-00922-8

6. Hagi T, Kurokawa Y, Kawabata R, Omori T, Matsuyama J, Fujitani K, et al. Multicentre biomarker cohort study on the efficacy of nivolumab treatment for gastric cancer. *Br J Cancer* (2020) 123:965–72. doi: 10.1038/s41416-020-0975-7

7. Kim ST, Cristescu R, Bass AJ, Kim KM, Odegaard JI, Kim K, et al. Comprehensive molecular characterization of clinical responses to PD-1 inhibition in metastatic gastric cancer. *Nat Med* (2018) 24:1449–58. doi: 10.1038/s41591-018-0101-z

8. Eso Y, Shimizu T, Takeda H, Takai A, Marusawa H. Microsatellite instability and immune checkpoint inhibitors: Toward precision medicine against gastrointestinal and hepatobiliary cancers. *J Gastroenterol* (2020) 55:15–26. doi: 10.1007/s00535-019-01620-7

9. Cancer Genome Atlas Research Network. Comprehensive molecular characterization of gastric adenocarcinoma. *Nature* (2014) 513:202–9. doi: 10.1038/nature13480

10. Munari E, Rossi G, Zamboni G, Lunardi G, Marconi M, Sommaggio M, et al. PD-L1 assays 22C3 and SP263 are not interchangeable in non-small cell lung cancer when considering clinically relevant cutoffs: An interclone evaluation by differently trained pathologists. *Am J Surg Pathol* (2018) 42:1384–9. doi: 10.1097/PAS.0000000000001105

11. Park Y, Koh J, Na HY, Kwak Y, Lee KW, Ahn SH, et al. PD-L1 testing in gastric cancer by the combined positive score of the 22C3 PharmDx and SP263 assay with clinically relevant cut-offs. *Cancer Res Treat* (2020) 52:661–70. doi: 10.4143/crt.2019.718

12. Seymour L, Bogaerts J, Perrone A, Ford R, Schwartz LH, Mandrekar S, et al. iRECIST: guidelines for response criteria for use in trials testing immunotherapeutics. *Lancet Oncol* (2017) 18:e143–52. doi: 10.1016/S1470-2045(17)30074-8

13. Gillies RJ, Kinahan PE, Hricak H. Radiomics: Images are more than pictures, they are data. *Radiology* (2016) 278:563–77. doi: 10.1148/radiol.2015151169

14. Xu Q, Sun Z, Li X, Ye C, Zhou C, Zhang L, et al. Advanced gastric cancer: CT radiomics prediction and early detection of downstaging with neoadjuvant chemotherapy. *Eur Radiol* (2021) 31:8765–74. doi: 10.1007/s00330-021-07962-2

15. Park KJ, Lee JL, Yoon SK, Heo C, Park BW, Kim JK. Radiomics-based prediction model for outcomes of PD-1/PD-L1 immunotherapy in metastatic urothelial carcinoma. *Eur Radiol* (2020) 30:5392–403. doi: 10.1007/s00330-020-06847-0

16. Yoon SH, Kim YH, Lee YJ, Park J, Kim JW, Lee HS, et al. Tumor heterogeneity in human epidermal growth factor receptor 2 (HER2)-positive advanced gastric cancer assessed by CT texture analysis: Association with survival after trastuzumab treatment. *PloS One* (2016) 11:e0161278. doi: 10.1371/journal.pone.0161278

17. Liang Z, Huang A, Wang L, Bi J, Kuang B, Xiao Y, et al. A radiomics model predicts the response of patients with advanced gastric cancer to PD-1 inhibitor treatment. *Aging (Albany NY)* (2022) 14:907–22. doi: 10.18632/aging.203850

18. Jiang Y, Wang H, Wu J, Chen C, Yuan Q, Huang W, et al. Noninvasive imaging evaluation of tumor immune microenvironment to predict outcomes in gastric cancer. *Ann Oncol* (2020) 31:760–8. doi: 10.1016/j.annonc.2020.03.295

19. Wada T, Yokota H, Horikoshi T, Starkey J, Hattori S, Hashiba J, et al. Diagnostic performance and inter-operator variability of apparent diffusion coefficient analysis for differentiating pleomorphic adenoma and carcinoma ex pleomorphic adenoma: Comparing one-point measurement and whole-tumor measurement including radiomics approach. *Jpn J Radiol* (2020) 38:207–14. doi: 10.1007/s11604-019-00908-1

20. Helmink BA, Reddy SM, Gao J, Zhang S, Basar R, Thakur R, et al. B cells and tertiary lymphoid structures promote immunotherapy response. *Nature* (2020) 577:549–55. doi: 10.1038/s41586-019-1922-8

21. Khorrami M, Prasanna P, Gupta A, Patil P, Velu PD, Thawani R, et al. Changes in CT radiomic features associated with lymphocyte distribution predict overall survival and response to immunotherapy in non-small cell lung cancer. *Cancer Immunol Res* (2020) 8:108–19. doi: 10.1158/2326-6066.CIR-19-0476

22. Sun R, Limkin EJ, Vakalopoulou M, Dercle L, Champiat S, Han SR, et al. A radiomics approach to assess tumour-infiltrating CD8 cells and response to anti-PD-1 or anti-PD-L1 immunotherapy: An imaging biomarker, retrospective multicohort study. *Lancet Oncol* (2018) 19:1180–91. doi: 10.1016/S1470-2045(18)30413-3

23. Basler L, Gabryś HS, Hogan SA, Pavic M, Bogowicz M, Vuong D, et al. Radiomics, tumor volume, and blood biomarkers for early prediction of pseudoprogression in patients with metastatic melanoma treated with immune checkpoint inhibition. *Clin Cancer Res* (2020) 26:4414–25. doi: 10.1158/1078-0432.CCR-20-0020

24. Lu L, Dercle L, Zhao B, Schwartz LH. Deep learning for the prediction of early on-treatment response in metastatic colorectal cancer from serial medical imaging. *Nat Commun* (2021) 12:6654. doi: 10.1038/s41467-021-26990-6

25. Xu Y, Hosny A, Zeleznik R, Parmar C, Coroller T, Franco I, et al. Deep learning predicts lung cancer treatment response from serial medical imaging. *Clin Cancer Res* (2019) 25:3266–75. doi: 10.1158/1078-0432.CCR-18-2495

26. Huang W, Jiang Y, Xiong W, Sun Z, Chen C, Yuan Q, et al. Noninvasive imaging of the tumor immune microenvironment correlates with response to immunotherapy in gastric cancer. *Nat Commun* (2022) 13:5095. doi: 10.1038/s41467-022-32816-w

27. Wang XX, Ding Y, Wang SW, Dong D, Li HL, Chen J, et al. Intratumoral and peritumoral radiomics analysis for preoperative Lauren classification in gastric cancer. *Cancer Imaging* (2020) 20:83. doi: 10.1186/s40644-020-00358-3

28. Lorensen WE, Cline HE. Marching cubes: A high resolution 3D surface construction algorithm. *ACM SIGGRAPH Comput Graph* (1987) 21:163–9. doi: 10.1145/37402.37422

29. Kim YY, Lee J, Jeong WK, Kim ST, Kim JH, Hong JY, et al. Prognostic significance of sarcopenia in microsatellite-stable gastric cancer patients treated with programmed death-1 inhibitors. *Gastric Cancer* (2021) 24:457–66. doi: 10.1007/s10120-020-01124-x

30. Martini DJ, Shabto JM, Goyal S, Liu Y, Olsen TA, Evans ST, et al. Body composition as an independent predictive and prognostic biomarker in advanced urothelial carcinoma patients treated with immune checkpoint inhibitors. *Oncologist* (2021) 26:1017–25. doi: 10.1002/onco.13922

31. Kunisaki C, Makino H, Takagawa R, Oshima T, Nagano Y, Kosaka T, et al. Tumor diameter as a prognostic factor in patients with gastric cancer. *Ann Surg Oncol* (2008) 15(7):1959–67. doi: 10.1245/s10434-008-9884-3

Glossary

ICI	Immune checkpoint inhibitors
ROI	Regions of interest
PFS	Progression free survival
PD-1	programmed cell death protein 1
PD-L1	programmed cell death ligand 1
CTLA-4	Cytotoxic T lymphocyteassociated antigen 4
dMMR	Mismatch repair deficiency
EBV	Epstein–Barr virus
CPS	Combined positive scores
pMMR	Mismatch repair proficiency
CT	Computed tomography
AUC	Area under the curve
ECOG PS	Eastern Cooperative Oncology Group performance status score
preAintra	Intratumoral regions at baseline atrial phase
preVintra	Intratumoral regions at baseline venous phase
preAperi	Peritumoral regions at baseline atrial phase
preVperi	Peritumoral regions at baseline venous phase
postAintra	Intratumoral regions at follow-up atrial phase
postVintra	Intratumoral regions at follow-up venous phase
postAperi	Peritumoral regions at follow-up atrial phase
postVperi	Peritumoral regions at follow-up venous phase
ΔAintra	Changes between baseline and follow-up features of intratumoral regions at atrial phase
ΔVintra	Changes between baseline and follow-up features of intratumoral regions at venous phase
ΔAperi	Changes between baseline and follow-up features of peritumoral regions at atrial phase
ΔVperi	Changes between baseline and follow-up features of peritumoral regions at venous phase
IQR	Interquartile ranges
ICCs	Intraclass correlation coefficients
LASSO	Least absolute shrinkage and the selection operator
C-index	Harrell's concordance index
CI	Confidence interval
HR	Hazard ratio
ΔVintra_ZV	ΔVintra_original_glszm_Zone Variance
postVperi_Sphericity	Postvperi_original_shape_Sphericity
NSCLC	Non–small cell lung cancer

frontiers | Frontiers in Oncology

TYPE Original Research
PUBLISHED 16 March 2023
DOI 10.3389/fonc.2023.1089365

OPEN ACCESS

EDITED BY
Chi Lin,
University of Nebraska Medical Center,
United States

REVIEWED BY
Liyun Chang,
I-Shou University, Taiwan
Yue Zheng,
Dana-Farber/Brigham and Women's Cancer Center, United States
Tong Wu,
Purdue University Indianapolis,
United States

*CORRESPONDENCE
Xiaobo Du
duxiaobo2005@126.com

†These authors have contributed equally to this work

SPECIALTY SECTION
This article was submitted to Gastrointestinal Cancers: Gastric and Esophageal Cancers, a section of the journal Frontiers in Oncology

RECEIVED 04 November 2022
ACCEPTED 24 February 2023
PUBLISHED 16 March 2023

CITATION
Liu J, Yang X, Mao X, Wang T, Zheng X, Feng G, Dai T and Du X (2023) Predicting the efficacy of radiotherapy for esophageal squamous cell carcinoma based on enhanced computed tomography radiomics and combined models. *Front. Oncol.* 13:1089365. doi: 10.3389/fonc.2023.1089365

Predicting the efficacy of radiotherapy for esophageal squamous cell carcinoma based on enhanced computed tomography radiomics and combined models

Jihui Liu†, Xiyue Yang†, Xin Mao, Tingting Wang, Xuhai Zheng, Gang Feng, Tangzhi Dai and Xiaobo Du*

Department of Oncology, National Health Commission (NHC) Key Laboratory of Nuclear Technology Medical Transformation (Mianyang Central Hospital), Mianyang Central Hospital, School of Medicine, University of Electronic Science and Technology, Mianyang, China

Purpose: This study aimed to investigate the ability of enhanced computed tomography (CT)-based radiomics and dosimetric parameters in predicting response to radiotherapy for esophageal cancer.

Methods: A retrospective analysis of 147 patients diagnosed with esophageal cancer was performed, and the patients were divided into a training group (104 patients) and a validation group (43 patients). In total, 851 radiomics features were extracted from the primary lesions for analysis. Maximum correlation minimum redundancy and minimum least absolute shrinkage and selection operator were utilized for feature screening of radiomics features, and logistic regression was applied to construct a radiotherapy radiomics model for esophageal cancer. Finally, univariate and multivariate parameters were used to identify significant clinical and dosimetric characteristics for constructing combination models. The area evaluated the predictive performance under the receiver operating characteristics (AUC) curve and the accuracy, sensitivity, and specificity of the training and validation cohorts.

Results: Univariate logistic regression analysis revealed statistically significant differences in clinical parameters of sex (p=0.031) and esophageal cancer thickness (p=0.028) on treatment response, whereas dosimetric parameters did not differ significantly in response to treatment. The combined model demonstrated improved discrimination between the training and validation groups, with AUCs of 0.78 (95% confidence interval [CI], 0.69–0.87) and 0.79 (95% CI, 0.65–0.93) in the training and validation groups, respectively.

Conclusion: The combined model has potential application value in predicting the treatment response of patients with esophageal cancer after radiotherapy.

KEYWORDS

radiotherapy, esophageal squamous cell carcinoma, computed tomography, radiomics, dosimetric

1 Introduction

Esophageal cancer is the eighth most prevalent and sixth most lethal cancer worldwide. In Asia and Eastern Europe, the most prevalent histological subtype of this malignancy is squamous cell carcinoma (1). More than 70% of patients with esophageal cancer are diagnosed at an intermediate to advanced stage, with unresectable or metastatic disease, and a combination of chemotherapy and radiation therapy is frequently provided to patients with esophageal cancer (2). Studies have indicated that the 5-year survival rate for patients with locally advanced esophageal cancer treated with radiation is only 36–47% (3, 4), and the 5-year overall survival of patients with complete remission (CR) is better than that of patients without CR (5). Therefore, early identification of patients who do not respond to radiotherapy and prompt monitoring of tumor response to treatment during radiotherapy are crucial for implementing individualized precision radiotherapy and enhancing overall patient survival.

Computed tomography (CT) is commonly used to assess the preoperative staging of esophageal cancer, including the extent of infiltration, lymph node extent, and metastasis, for clinical treatment decisions (6). However, CT only shows the external morphological features of esophageal cancer. It is challenging to fully assess the heterogeneity within the tumor. Radiomics extracts quantitative CT image features with a high throughput. This information extraction is based on the entire tumor and is not confined to a single tissue sample, allowing for a thorough description of tumor heterogeneity. Hou et al. investigated the baseline CT-enhanced image characteristics of 49 patients (33 with strong response and 16 with poor response) with esophageal cancer treated with radiation and found substantial differences in kurtosis and skewness in histogram characteristics between the two groups (7). Yang et al.'s analysis of patients receiving lower doses of neoadjuvant chemoradiotherapy (nCRT) did not reveal any clinical characteristics that predicted patients' arrival to pathological complete response (pCR). However, radiomics features enabled the construction of three highly accurate models for predicting pCR following nCRT in individuals with esophageal cancer (8). Some researchers have attempted to predict an outcome by combining intratumoral and peritumoral features. Radiomics examination is not restricted to the tumor body. Hu et al. included patients with esophageal cancer who underwent surgery after nCRT in two institutions and extracted radiomics features from baseline-enhanced CT intratumoral and peritumoral regions to construct models, demonstrating that models constructed with seven intratumoral and six peritumoral radiomics features had superior predictive performance, with receiver operating characteristic (ROC) curves of 0.906 and 0.85 in the training and validation groups, respectively (9).

With the progress of radiotherapy technology, esophageal cancer can be treated by three-dimensional conformal radiation therapy (3D-CRT), intensity-modulated radiotherapy (IMRT), and volumetric-modulated arc therapy (VMAT), but its 5-year survival rate remains inadequate. Local uncontrolled or recurrence remains the most common cause of radiotherapy failure. Due to individual variances, the radiation dose for each patient varies. Some studies have demonstrated the significant efficacy of radiotherapy up to a dose of 40 Gy in certain patients, whereas others are not sensitive to radiotherapy and fail to improve their local control rate even when administered 70 Gy (10). Incremental radiation therapy dosages may result in severe toxic side effects, the severity of which is mostly determined by clinical criteria and the quantity of healthy tissue surrounding the exposed tumor. In radiation therapy for cancer, metrics, such as prescribed dose, dose distribution, and dose-volume histogram, can also be utilized to evaluate treatment response and cancer prognostic analysis (11, 12).

To the best of our knowledge, the doses of radiotherapy received by patients in some current studies were also significantly lower than those of radical radiotherapy. Few studies have incorporated dosimetric data and several other variables into predictive models. To assist clinicians in deciding the best course of treatment for patients with esophageal cancer receiving radiation, this study aimed to examine the effects of enhanced CT-based radiomics in predicting the response to radiotherapy.

2 Materials and methods

2.1 Patients and treatment

The ethical committee allowed a retrospective collection of 147 patients with a histological diagnosis of esophageal squamous cell carcinoma at our hospital between January 2018 and December 2021 (approval number: S2022035-01). The inclusion criteria were as follows: (a) patients with a histopathology-confirmed squamous cell carcinoma of the esophagus, (b) patients who had completed radiotherapy, (c) patients without distant metastases or other neoplastic diseases, and (d) patients with trackable treatment results. The exclusion criteria were as follows: (a) patients with missing follow-up data; (b) patients who had previously undergone chest radiation, chemotherapy, or surgical tumor excision; (c) patients with multifocal primary disease; and (d) extreme respiratory motion artifacts; and (e) invisible tumor on CT image. Image quality is judged by the two radiologists independently, and the disagreement is resolved through negotiation. Patients underwent 3D-CRT, IMRT, or VMAT during the treatment period. In total, 100% of the prescribed dose encompassed 95% of the volume of the target area for all patients.

2.2 Response assessment

After 3 months of treatment, response to treatment was assessed by CT findings and determined according to the efficacy evaluation criteria for solid tumors (Response Evaluation Criteria in Solid Tumors) (13). CR, partial response (PR), stable disease (SD), and progressive disease (PD) were assessed. Patients with CR or PR were classified as responders, whereas patients with SD or PD were classified as nonresponders.

2.3 Image acquisition

All patients underwent chest CT examinations utilizing a Siemens large-aperture CT scanner. The scan parameters (tube voltage, 120 kVp; tube current, 200 mAs; matrix, 512×512; layer thickness, 5 mm; layer spacing, 5 mm) were in accordance with the clinical standard acquisition methodology. Iodine contrast agent was injected at 3 ml/s using a high-pressure syringe. A radiation oncologist drew the primary gross tumor volume (GTV) on Oncentra software, which was subsequently examined by an experienced radiation oncologist. Avoiding the esophagus lumen, blood arteries, periesophageal fat, and artifacts were outlined as the GTV.

2.4 Feature extraction

TPS exported Digital Imaging and Communications in Medicine files to 3D Slicer(version,4.11, https://www.slicer.org) for preprocessing (1×1×1 resampling) and feature extraction (Supplementary Figure 1) (14). In total, 851 features, comprising 107 original features and 744 wavelet features, were extracted from each GTV. The original features included 18 first-order statistical features, 14 shape size features, 14 gray-level dependence matrix, 16 gray-level size zone matrix, 24 gray-level co-occurrence matrix,16 gray-level run-length matrix, and 5 neighboring gray tone difference matrix. Image transformation features, such as wavelet transform features, were primarily utilized to divide original tumor images into distinct frequency domains. Except for 14 shape features that do not change with image transformation, each of the 93 features is extracted to different values in the image GTV after 8 wavelet transforms.

2.5 Feature screening and model construction

Random stratified sampling was used to divide 147 patients into two groups (104 and 43 patients in the training and validation groups, respectively). Data standardization and feature extraction were performed using R software (version 3.6.0, https://www.r-project.org).The extracted features were preprocessed with Z-score for normalization to reduce the effect of different magnitudes on the features, specifically by eliminating the mean of each feature to center the feature values and then dividing by the standard deviation of each feature. The minimum redundancy maximum relevance (mRMR) algorithm was then used to screen features. The mRMR algorithm is based on calculating a pair of correlation coefficient (A) and redundancy coefficient value (B) for each feature, where the correlation coefficient represents the relationship between the feature and treatment response and the redundancy coefficient represents the redundancy coefficient between features. The A-B values of all parameter values for features were then ordered in decreasing order (15). The least absolute shrinkage and selection operator (LASSO) method was then utilized for additional feature screening using tenfold cross-validation. A logistic regression model calculated a radiomics score (Rad-score) for each patient using model-weighted coefficients.

2.6 Model construction and evaluation

We established a combined model to predict the efficacy of radiotherapy for esophageal cancer by using multivariate logistic regression analysis. The variables included Rad-score, clinical and dosimetric parameters. The Combine model is finally demonstrated through a nomogram. The performance of the model was evaluated using area under the curve (AUC), precision, sensitivity, and specificity. Using a decision curve analysis, the quantification of net benefits under different threshold probabilities was confirmed.

2.7 Statistical analyses

All statistical analyses were performed using the R software. Continuous variables are expressed as median (Q1, Q3) using the Mann–Whitney U test. For the count data, the Fisher's exact probability approach was utilized. Univariate and multivariate logistic regression analyses were performed to identify the independent predictors of clinical and dosimetric indicators. The difference in AUC between models was examined using the Delong test. $P<0.05$ was considered statistically significant.

3 Results

In total, 236 patients with esophageal cancer were treated in our hospital, of whom 15 discontinued treatment, 23 were lost to follow-up, 22 had a history of radiotherapy, 10 had incomplete data and19 had poor image quality. These patients were excluded from the statistical analyses. The remaining 147 patients (113 males and 34 females; median age, 66 years) met the inclusion criteria. The number of patients who responded to treatment (CR+PR) was 89, whereas 58 patients (PD+SD) were nonresponders. The clinical and dosimetric characteristics of the patients are shown in Table 1.

LASSO regression was used to minimize the dimensionality of the recovered features, and 7 out of 851 possible radiomics features were selected to calculate their products with the regression coefficients using the following equations (Figures 1A, B). Each patient's Rad-score was obtained and calculated as follows: Rad-score=−0.236×Original_firstorder_90Percentile-0.026×Wavelet.Hll_firstorder_Skewness-0.128×Original_glszm_HighGrayLevelZoneEmphasis+0.19×Wavelet.Lhh_glcm_ClusterShade-0.046×Wavelet.Hll_glcm_ClusterShade-0.049×Wavelet.Hll_firstorder_Maximum+0.173×Wavelet.Hhl_glcm_ClusterShade

Figure 2 illustrates the results of using the AUC size of the area under the ROC curve to measure the prediction performance of the model. In the training group, the AUC value of radiomics for predicting esophageal cancer treatment response was 0.76 (95% confidence interval [CI], 0.67–0.85), with an accuracy of 0.692 (95% CI, 0.594–0.779), a sensitivity of 80.5%, and a specificity of 61.9%. In the validation group, the AUC, accuracy, sensitivity, and specificity

10.3389/fonc.2023.1089365

TABLE 1 The clinical and dosimetric characteristics of the patients.

Characteristic	Non-response (n=58)	Response (n=89)	*p*
Age	67.00 (59.00,73.00)	66.00 (60.00,73.00)	0.899
Gender			0.008*
Female	20 (34.48%)	14 (15.73%)	
Male	38 (65.52%)	75 (84.27%)	
Tumor location			0.176
Cervical	5 (8.62%)	2 (2.25%)	
Upper	12 (20.69%)	17 (19.10%)	
Middle	27 (46.55%)	54 (60.67%)	
Lower	14 (24.14%)	16 (17.98%)	
Histologic grade			0.141
Poor	24 (41.38%)	24 (26.97%)	
Moderate	31 (53.45%)	62 (69.66%)	
Well	3 (5.17%)	3 (3.37%)	
T stage			0.812
T1	2 (3.45%)	1 (1.12%)	
T2	11 (18.97%)	18 (20.22%)	
T3	30 (51.72%)	44 (49.44%)	
T4	15 (25.86%)	26 (29.21%)	
N stage			0.373
N0	14 (24.14%)	14 (15.73%)	
N1	30 (51.72%)	43 (48.31%)	
N2	13 (22.41%)	30 (33.71%)	
N3	1 (1.72%)	2 (2.25%)	
M stage			0.765
M0	54 (93.10%)	83 (93.26%)	
M1	4 (6.90%)	6 (6.74%)	
Group stage			0.309
I	2 (3.45%)	0 (0.00%)	
II	13 (22.41%)	19 (21.35%)	
III	26 (44.83%)	38 (42.70%)	
IV	17 (29.31%)	32 (35.96%)	
Hypertension			0.865
Yes	6 (10.34%)	10 (11.24%)	
No	52 (89.66%)	79 (88.76%)	
Smoking history			0.466
Yes	15 (25.86%)	28 (31.46%)	
No	43 (74.14%)	61 (68.54%)	
Drinking history			0.748
Yes	13 (22.41%)	22 (24.72%)	

(Continued)

TABLE 1 Continued

Characteristic	Non-response (n=58)	Response (n=89)	*p*
No	45 (77.59%)	67 (75.28%)	
Nutrition			0.154
1	18 (31.03%)	35 (39.33%)	
2	17 (29.31%)	27 (30.34%)	
3	6 (10.34%)	13 (14.61%)	
4	13 (22.41%)	7 (7.87%)	
5	4 (6.90%)	7 (7.87%)	
Thickness	1.35 (1.19,1.60)	1.50 (1.17,1.90)	0.048*
Length	5.50 (4.50,7.00)	5.90 (4.50,7.00)	0.959
BMI	22.00 (19.59,23.42)	21.50 (19.80,23.30)	0.834
Dose	60.00 (60.00,60.00)	60.00 (60.00,60.00)	0.650
Frequency	30.00 (28.00,30.00)	30.00 (28.70,30.00)	0.718
Divided dose	2.00 (2.00,2.13)	2.00 (2.00,2.00)	0.352
PTV			
Dmin (Gy)	5400.00 (4952.10,5601.20)	5306.00 (4786.50,5596.50)	0.660
Dmax (Gy)	6636.00 (6518.50,6722.50)	6599.00 (6478.90,6757.90)	0.641
Dmean (Gy)	6252.25 (6203.85,6293.10)	6228.00 (6167.00,6286.60)	0.374
V90 (%)	99.99 (99.86, 100.00)	99.99 (99.86, 100.00)	0.815
V93 (%)	99.78 (99.45, 99.99)	99.86 (99.44, 99.99)	0.837
V95 (%)	99.43 (99.14, 99.71)	99.57 (98.99, 99.87)	0.576
Lung			
Dmean (Gy)	1169.00 (1047.85,1366.30)	1200.00 (1007.10,1341.30)	0.984
V5 (%)	53.52 (48.52, 58.63)	51.72 (44.51, 58.68)	0.429
V10 (%)	37.41 (34.60, 41.99)	38.51 (33.31, 41.38)	0.967
V20 (%)	21.41 (18.81, 27.59)	23.04 (19.82, 26.05)	0.898
V30 (%)	11.49 (8.04, 14.55)	12.45 (8.22, 14.82)	0.756
V40 (%)	5.68 (3.88, 8.34)	5.94 (3.52, 8.37)	0.997
Heart			
Dmean (Gy)	2748.00 (1640.10,3255.50)	2598.00 (1108.20,3190.70)	0.234
V5 (%)	92.89 (57.94, 98.43)	87.07 (38.63, 97.13)	0.134
V10 (%)	79.00 (48.04, 91.82)	75.95 (32.61, 89.80)	0.242
V15 (%)	69.00 (41.20, 83.75)	62.35 (24.00, 80.68)	0.203
V20 (%)	61.52 (36.47, 74.22)	53.89 (19.91, 73.42)	0.241
V25 (%)	54.67 (27.72, 66.24)	46.25 (17.49, 64.02)	0.229
V30 (%)	43.34 (21.91, 55.79)	39.34 (14.13, 50.50)	0.161
V40 (%)	24.34 (12.63, 39.00)	20.31 (7.47, 32.04)	0.210
V50 (%)	10.34 (4.52, 14.97)	7.47 (2.51, 14.51)	0.189
V60 (%)	1.60 (0.00, 4.03)	1.29 (0.00, 3.99)	0.564

(Continued)

TABLE 1 Continued

Characteristic	Non-response (n=58)	Response (n=89)	*p*
Spinal Cord			
Dmax (Gy)	4421.00 (4338.85,4531.00)	4421.00 (4338.60,4521.50)	0.855
Dmean (Gy)	2418.5 (1910.75,2920.75)	2295 (1816.01,2725.60)	0.301

*p<0.05.

were 0.73 (95% CI, 0.58–0.88), 0.721 (95% CI, 0.563–0.846), 88.2%, and 61.5%, respectively. The Delong test revealed no statistically significant difference between the effectiveness of the two groups (p>0.05).

The clinical and dosimetric parameters related to treatment response in the training group were determined by univariate and multivariate logistic regression analyses. Sex and esophageal carcinoma thickness were substantially associated with treatment response among clinical characteristics, as shown by univariate logistic regression analysis. However, none of the dosimetric variables were related to treatment response (Table 2). Hence, sex, esophageal cancer thickness, and Rad-score were

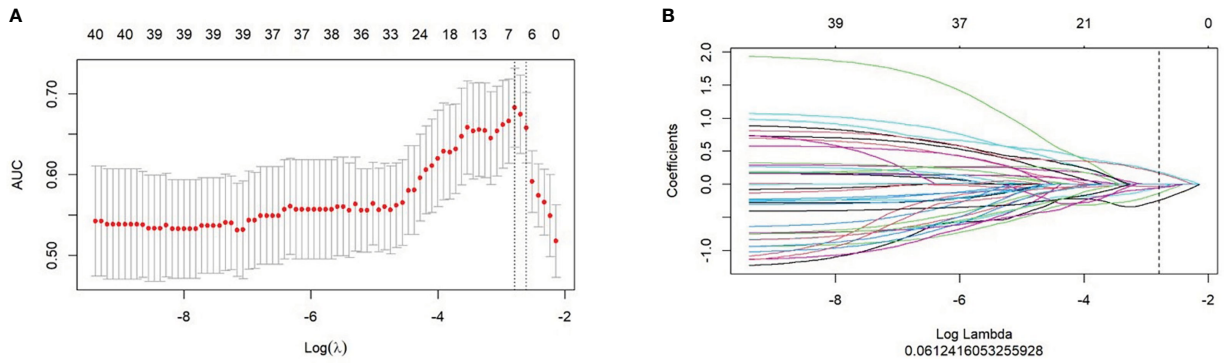

FIGURE 1
Selection of radiomics features for predicting response using the least absolute shrinkage and selection operator (LASSO) logistic regression model. **(A)** LASSO coefficient profiles of the radiomics features. **(B)** The cross-validation curve.

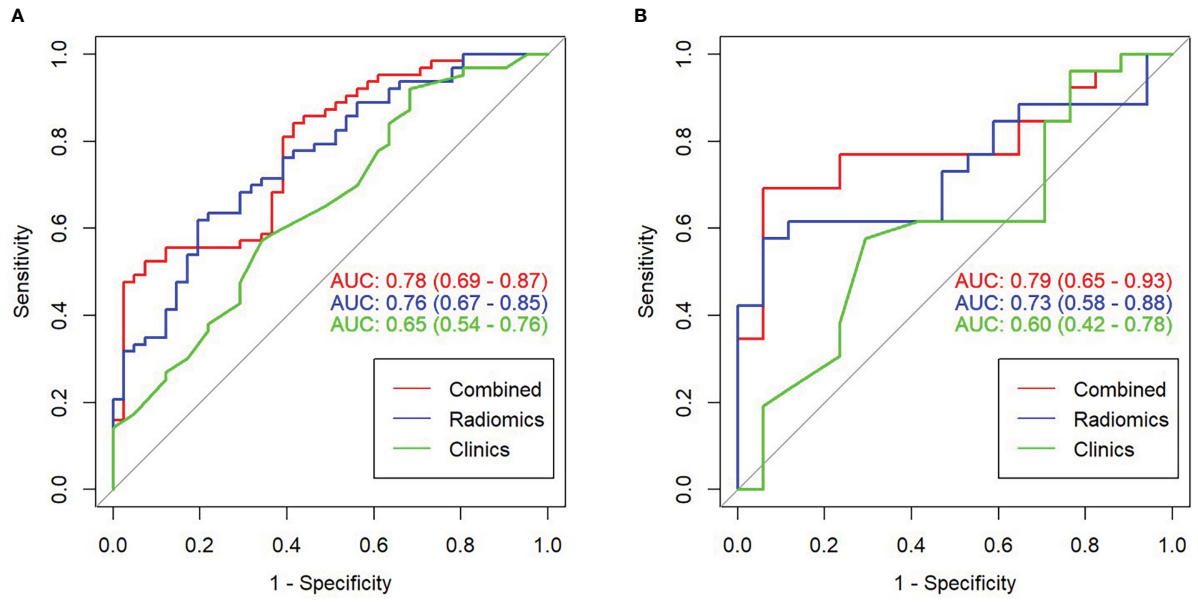

FIGURE 2
Receiver operating characteristic (ROC) curve comparison of combined and radiomics and clinical models. **(A)** ROC curve in the training set. **(B)** ROC curve in the validation set.

TABLE 2 Univariate and Multivariate logistic regression analysis in the training set.

Variable	Univariate analysis		Multivariate analysis	
	OR (95%CI)	*p*	OR (95%CI)	*p*
Age	0.985 (0.940, 1.032)	0.516		
Gender	2.727 (1.098, 6.771)	0.031*	2.028 (0.705,5.838)	0.189
Tumor location	1.392 (0.823, 2.354)	0.217		
Histologic grade	1.523 (0.707, 3.278)	0.282		
T stage	1.278 (0.726, 2.251)	0.395		
N stage	1.302 (0.759, 2.234)	0.338		
M stage	0.633 (0.121, 3.301)	0.588		
Group stage	1.291 (0.761, 2.189)	0.343		
Treatment	1.599 (0.522, 4.898)	0.411		
Hypertension	1.156 (0.316, 4.229)	0.826		
Smoking history	1.442 (0.593, 3.506)	0.420		
Drinking history	1.404 (0.539, 3.661)	0.487		
Nutrition	0.879 (0.648, 1.191)	0.405		
Medication	1.490 (0.831, 2.674)	0.181		
Thickness	2.419 (1.101, 5.317)	0.028*	2.033 (0.877,4.713)	0.098
Length	0.972 (0.804, 1.176)	0.772		
BMI	1.001 (0.880, 1.139)	0.985		
Dose	0.984 (0.885, 1.094)	0.768		
Frequency	1.027 (0.811, 1.301)	0.824		
Divided dose	0.150 (0.001,21.467)	0.454		
PTV_Dmin	1.000 (1.000, 1.000)	0.576		
PTV_Dmax	1.000 (0.999, 1.000)	0.530		
PTV_Dmean	1.000 (0.999, 1.000)	0.452		
PTV_V90	0.361 (0.039, 3.386)	0.373		
PTV_V93	0.826 (0.294, 2.317)	0.716		
PTV_V95	1.177 (0.553, 2.507)	0.672		
Lung_V5	0.981 (0.943, 1.020)	0.325		
Lung_V10	1.000 (0.946, 1.056)	0.991		
Lung_V20	0.999 (0.931, 1.072)	0.977		
Lung_V30	0.995 (0.975, 1.015)	0.617		
Lung_V40	1.005 (0.970, 1.041)	0.772		
Lung_Dmean	1.000 (0.999, 1.001)	0.979		
Heart_V5	0.992 (0.979, 1.005)	0.236		
Heart_V10	1.001 (0.998, 1.004)	0.572		
Heart_V15	0.993 (0.980, 1.007)	0.325		
Heart_V20	0.993 (0.979, 1.007)	0.334		
Heart_V25	0.993 (0.977, 1.009)	0.368		
Heart_V30	0.990 (0.973, 1.008)	0.265		

(Continued)

TABLE 2 Continued

Variable	Univariate analysis		Multivariate analysis	
	OR (95%CI)	*p*	OR (95%CI)	*p*
Heart_V40	0.992 (0.970, 1.014)	0.465		
Heart_V50	0.985 (0.944, 1.027)	0.469		
Heart_V60	1.023 (0.902, 1.162)	0.720		
Heart_Dmean	1.000 (0.999, 1.000)	0.318		
Spinal_Cord_Dmax	1.001 (0.999, 1.002)	0.292		
Spinal_Cord_Dmean	1.000 (0.999, 1.000)	0.538		
Rad-score	18.861 (4.718,75.403)	<0.01*	15.326 (3.687,63.693)	<0.01*

*p<0.05.

incorporated into the multivariate logistic analysis to construct a combined model.

Based on the results of the multivariate analysis, a combine model is finally demonstrated through a nomogram (Figure 3), The risk ratio and significance of each variable in the multivariate combined model are shown in Supplementary Table 1, and the outcomes are presented in Figure 2. In the training group, the AUC, accuracy, sensitivity, and specificity for the combined model were 0.78 (95% CI, 0.69–0.87), 0.673 (95% CI, 0.574–0.762), 96.7%, and 54.8%, respectively. In the validation group, the AUC, accuracy, sensitivity, and specificity were 0.79 (95% CI, 0.65–0.93), 0.651 (95% CI, 0.491–0.790), 92.3%, and 53.3%, respectively. The performance metrics of radiomics, clinics, and combined models are displayed in Table 3.The AUC of combined model was higher than that of the clinical model, indicating that the combined model achieved considerably better discrimination capability than clinical model(DeLong's test, $p < 0.001$).However, there was no significant difference between the combined and the radiomics model (p=0.772) and between the radiomics and the clinical model (p=0.133).

Using decision curves to analyze the influence of the model on clinical treatment decisions, the clinical model (without Rad-score) or the combined model (with Rad-score) outperformed "all treatment" or "no treatment" when the risk threshold was greater than 10%, and the combined model had greater predictive power than the clinical model when the threshold was more significant than 23% (Figure 4).

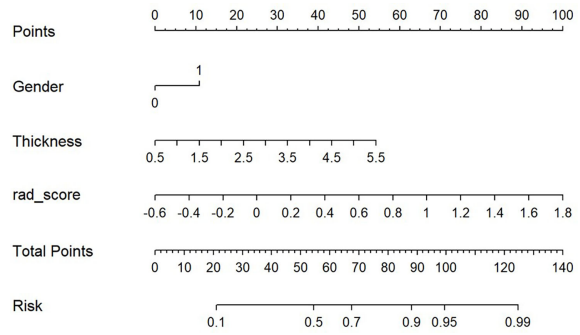

FIGURE 3
Predictive nomogram combined Rad-score, sex, and esophageal cancer thickness.

4 Discussion

In this study, radiomics features of localized CT images of patients before radiotherapy were extracted, and the optimal seven features were screened out, combined with clinical features to construct a model of the treatment response of patients receiving radiotherapy, which can provide a cost-effective and noninvasive method for predicting the efficacy of radiotherapy.

In the present study, two clinical factors, esophageal carcinoma thickness and sex, were substantially associated with treatment response. Previous studies have demonstrated the predictive usefulness of esophageal carcinoma thickness in determining preoperative treatment response (16, 17). According to Zhang et al., esophageal cancer thickness as a single predictor can evaluate survival and efficacy of preoperative chemotherapy (18). The limited value of thickness measurement on CT may be attributed to the swelling effect of necrotic and fibrotic tissues following radiation, resulting in persistent imaging abnormalities. Radiomics augments standard imaging parameters. It recognizes intra-tissue heterogeneity, hence increasing the predictive accuracy of the model for tumor response. According to a previous study on esophageal cancer, women are more likely to present with pCR and have higher survival rates than men (19, 20). In contrast, the results of the current study were different, possibly due to the small number of women with esophageal cancer in the study population, which led to unusual experimental results. Dosimetric measures were not altered significantly when the treatment response was reversed. Jin et al. obtained similar results using a dosimetric model to evaluate treatment response in esophageal cancer after radiotherapy (21). The obtained dosimetric parameters may be 3D dose distributions, which describe the volume of irradiation received by an organ at a provided dose. There is a loss of spatial link information between voxels.

Several studies have demonstrated the use of radiomics, an emerging image analysis technique, to predict the efficacy of radiation in patients with esophageal cancer. Murakami et al.

TABLE 3 Predictive performance of radiomics, clinics, and combined models.

Model	Training set (n=104)				Test set (n=43)			
	AUC (95%CI)	Accuracy	Sensitivity	Specificity	AUC (95%CI)	ACC	Sensitivity	Specificity
Radiomics	0.76 (0.67-0.85)	0.692 (0.594-0.779)	80.5%	61.9%	0.73 (0.58-0.88)	0.721 (0.563-0.846)	88.2%	61.5%
Clinics	0.65 (0.54-0.76)	0.683 (0.584-0.771)	67.4%	72.2%	0.60 (0.42-0.78)	0.628 (0.467-0.770)	63.9%	57.1%
Combine	0.78 (0.69-0.87)	0.673 (0.574-0.762)	96.7%	54.8%	0.79 (0.65-0.93)	0.651 (0.491-0.790)	92.3%	53.3%

retrieved 22 radiomics variables for LASSO regression analysis from positron emission tomography (PET)/CT images of 98 patients with esophageal cancer treated with nCRT. Using a neural network classifier, they developed a prediction model with accuracy, sensitivity, and specificity of 89.6%, 92.7%, and 89.5%, respectively (22). Hou et al. extracted 138 radiomics features from the pre-therapy T2-weighted (T2W)- and spectral attenuated inversion recovery (SPAIR) T2W-magnetic resonance imaging (MRI) sequences of 68 patients with esophageal squamous carcinoma, which could distinguish between CR and stable lesions, partial remission and stable lesions, and reactive and non-reactive lesions by 26, 17, and 33 features, respectively, and used artificial neural networks (ANNs) and support vector machine (SVM) to construct predictive models. The performance of the SPAIR T2W-MRI model was superior to that of the T2W sequence (SVM, 0.929; ANN, 0.883) (23). However, these earlier studies rarely incorporated several elements, such as dosimetric parameters, into model projections. In some of these studies, patients received nCRT, with significantly lower treatment doses than radical radiotherapy. In this study, dosimetric, clinical, and other multiple factors were considered, and the LASSO regression method was used to construct a model for predicting treatment response after radiotherapy in patients with esophageal cancer, with a maximum sensitivity of 96.7% and a maximum AUC of 0.79, indicating that the prediction model has a high level of confidence in identifying treatment response. Yip et al. predicted the treatment response of patients with esophageal cancer based on PET/CT utilizing a radiomics approach. They showed high sensitivity (81%) and specificity (82%) (24), which are comparable to the current study's findings. Luo et al. studied baseline CT images of 226 patients receiving nCRT for esophageal cancer, and LASSO was used to build Rad-score for seven radiomics features. Combining the radiomics labels with clinical staging, nomograms were created to predict CR, with AUCs of 0.844 and 0.807 for the training and validation groups, respectively. The prediction algorithm based on the nomogram outperformed clinical staging (25). The predictive performance of the combined model was similarly superior to that of the only radiomics model in this study.

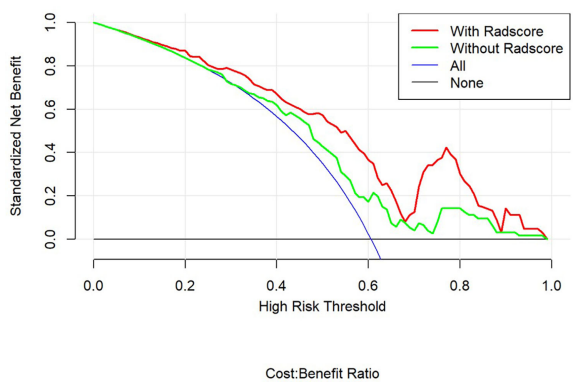

FIGURE 4
Decision curve analysis for the combined and clinical models.

Currently, CT-based radiomics characteristics consist primarily of geometric, morphological, textural, and intensity-based histogram characteristics. Textural characteristics are a standard way to assess tumor heterogeneity (26). Yip et al. studied PET/CT images of 31 patients with esophageal cancer before and after nCRT and reported that the grayscale histogram standard deviation (histogram SD) characteristics of tumors before and after therapy were related to tumor regression grade (27). In addition, another study conducted by Yip et al. extracted radiomics features that responded to patient heterogeneity in CT radiomics before and after radiotherapy, such as entropy, homogeneity, mean gray intensity, kurtosis, and standard deviation of the histogram. After comparing the changes in these texture features with patient survival, they discovered that entropy, homogeneity, and skewness predicted patient survival after treatment (28). Nakajo et al. extracted textural features from PET/CT scans of 52 patients with esophageal cancer receiving concurrent radiation. They concluded that texture-related characteristics could predict clinical response (29). The preceding study suggests that we can analyze the heterogeneous information of esophageal cancers based on the radiomics features of pretreatment CT and then develop a model to predict the efficacy of radiation in patients. In the present study, we discovered that the 90th percentile of the first-order statistical parameters may differentiate between responders and nonresponders.Texture features reflect the spatial distribution of pixels within the tumor (26), and the spatial distribution of pixels is more irregular in heterogeneous tumor pictures. The two-dimensional gray area size matrix's large area dominance feature (glszm HighGrayLevelZoneEmphasis) indicates more related areas in the image, indicating a coarser texture, and treatment responses can be classed accordingly. Additionally, the Gabor wavelet transform was employed to extract additional features. As a short-time Fourier

transform, Gabor wavelet transformations can deconstruct a picture into its component frequencies and directions (30). This study also demonstrates that Wavelet.Hll firstorder Skewness, Wavelet.Lhh glcm ClusterShade, Wavelet.Hll glcm ClusterShade, Wavelet.Hll firstorder Maximum, and Wavelet.Hhl glcm ClusterShade may discriminate the treatment response.

This study has some limitations. First, this study lacked multicenter validation and was conducted at a single institution. Nonetheless, the data in this study were obtained from a single CT scanner, which ensures equal scanning parameters and eliminates the influence of multiple devices and scanning parameters on picture characteristics. Second, a previous study showed that genes such as CXCR-2 and cyclin D1 are closely related with the prognosis of tumors (31). The incorporation of genetic characteristics into the radiomics model is vital.

5 Conclusion

In this study, a noninvasive, comprehensive, and individualized radiotherapy efficacy prediction model was developed by retrospectively analyzing the radiomics features of pre-radiotherapy CT images of patients with esophageal cancer. Validation and model evaluation were also performed. The model integrated radiomics features and clinical factors with good predictive accuracy, providing a cost-effective and simple evaluation technique for determining the effectiveness of radiation for esophageal cancer.

Data availability statement

The original contributions presented in the study are included in the article/Supplementary Material. Further inquiries can be directed to the corresponding author.

Ethics statement

The studies involving human participants were reviewed and approved by ethical committee of Mianyang Central Hospital. The patients/participants provided their written informed consent to participate in this study.

Author contributions

XD, guarantor of integrity of the entire study and manuscript editing. JL and XY, study concepts and design. JL and XY, literature research. JL, XY, XM, TW, XZ, GF, TD, and XD, data collection. JL, XY, and XD, data analysis. JL and XY, manuscript preparation. All authors contributed to the article and approved the submitted version.

Conflict of interest

The authors declare that the research was conducted in the absence of any commercial or financial relationships that could be construed as a potential conflict of interest.

Publisher's note

All claims expressed in this article are solely those of the authors and do not necessarily represent those of their affiliated organizations, or those of the publisher, the editors and the reviewers. Any product that may be evaluated in this article, or claim that may be made by its manufacturer, is not guaranteed or endorsed by the publisher.

Supplementary material

The Supplementary Material for this article can be found online at: https://www.frontiersin.org/articles/10.3389/fonc.2023.1089365/full#supplementary-material

SUPPLEMENTARY FIGURE 1
Analysis flowchart. The enhanced computed tomography (CT) images **(A, D)**. GTV of manual segmentation **(B, E)**. Generation of 3D ROI **(C, F)**.

References

1. Garg PK, Sharma J, Jakhetiya A, Goel A, Gaur MK. Preoperative therapy in locally advanced esophageal cancer. *World J Gastroenterol* (2016) 22(39):8750–9. doi: 10.3748/wjg. v22. i39.8750

2. Taylor A, Chadwick GA, Groene O, Greenaway K. The national oesophago-gastric cancer audit. In: *An audit of the care received by people with oesophago-gastric cancer in England and Wales*. 2014: The National Oesophago-Gastric Cancer Audit (2014).

3. Sjoquist KM, Burmeister BH, Smithers BM, Zalcberg JR, Simes RJ, Barbour A, et al. Survival after neoadjuvant chemotherapy or chemoradiotherapy for resectable oesophageal carcinoma: An updated meta-analysis. *Lancet Oncol* (2011) 12(7):681–92. doi: 10.1016/S1470-2045(11)70142-5

4. van Hagen P, Hulshof MC, van Lanschot JJ, Steyerberg EW, van Berge Henegouwen MI, Wijnhoven BP, et al. Preoperative chemoradiotherapy for esophageal or junctional cancer. *N Engl J Med* (2012) 366(22):2074–84. doi: 10.1056/NEJMoa1112088

5. Hammoud ZT, Kesler KA, Ferguson MK, Battafarrano RJ, Bhogaraju A, Hanna N, et al. Survival outcomes of resected patients who demonstrate a pathologic complete response after neoadjuvant chemoradiation therapy for locally advanced esophageal cancer. *Dis Esophagus* (2006) 19(2):69–72. doi: 10.1111/j.1442-2050.2006.00542.x

6. Umeoka S, Koyama T, Togashi K, Saga T, Watanabe G, Shimada Y, et al. Esophageal cancer: evaluation with triple-phase dynamic CT–initial experience. *Radiology* (2006) 239(3):777–83. doi: 10.1148/radiol.2393050222

7. Hou Z, Ren W, Li S, Liu J, Sun Y, Yan J, et al. Radiomic analysis in contrast-enhanced CT: predict treatment response to chemoradiotherapy in esophageal carcinoma. *Oncotarget* (2017) 8(61):104444–54. doi: 10.18632/oncotarget.22304

8. Yang Z, He B, Zhuang X, Gao X, Wang D, Li M, et al. CT-based radiomic signatures for prediction of pathologic complete response in esophageal squamous cell carcinoma after neoadjuvant chemoradiotherapy. *J Radiat Res* (2019) 60(4):538–45. doi: 10.1093/jrr/rrz027

9. Hu Y, Xie C, Yang H, Ho JWK, Wen J, Han L, et al. Assessment of intratumoral and peritumoral computed tomography radiomics for predicting pathological complete response to neoadjuvant chemoradiation in patients with esophageal squamous cell

carcinoma. *JAMA Netw Open* (2020) 3(9):e2015927. doi: 10.1001/jamanetworkopen.2020.15927

10. Minsky BD, Pajak TF, Ginsberg RJ, Pisansky TM, Martenson J, Komaki R, et al. INT 0123 (Radiation therapy oncology group 94-05) phase III trial of combined-modality therapy for esophageal cancer: High-dose versus standard-dose radiation therapy. *J Clin Oncol* (2002) 20(5):1167–74. doi: 10.1200/JCO.2002.20.5.1167

11. Garcia S, Tavares A, Peixoto P, Costa F, Pinto G. PO-1073: Dosimetric predictors of survival in esophageal cancers treated with preoperative chemoradiation. *Radiotherapy Oncol* (2020) 152(S1):S569–70. doi: 10.1016/S0167-8140(21)01090-2

12. Cho WK, Oh D, Kim HK, Ahn YC, Noh JM, Shim YM, et al. Dosimetric predictors for postoperative pulmonary complications in esophageal cancer following neoadjuvant chemoradiotherapy and surgery. *Radiotherapy Oncol* (2019) 133:87–92. doi: 10.1016/j.radonc.2019.01.005

13. Therasse P, Arbuck SG, Eisenhauer EA, Wanders J, Kaplan RS, Rubinstein L, et al. New guidelines to evaluate the response to treatment in solid tumors. European organization for research and treatment of cancer, national cancer institute of the united states, national cancer institute of Canada. *J Natl Cancer Institute* (2000) 92 (3):205–16. doi: 10.1093/jnci/92.3.205

14. van Griethuysen JJM, Fedorov A, Parmar C, Hosny A, Aucoin N, Narayan V, et al. Computational radiomics system to decode the radiographic phenotype. *Cancer Res* (2017) 77(21):e104–7. doi: 10.1158/0008-5472.CAN-17-0339

15. Quan Z, Jiancang Z, Liujuan C, Rongrong J. A novel features ranking metric with application to scalable visual and bioinformatics data classification. *Neurocomputing* (2016) 173(2):346–54. doi: 10.1016/j.neucom.2014.12.123

16. Swisher SG, Maish M, Erasmus JJ, Correa AM, Ajani JA, Bresalier R, et al. Utility of PET, CT, and EUS to identify pathologic responders in esophageal cancer. *Ann Thorac Surg* (2004) 78(4):1152–1160, 1152-1160. doi: 10.1016/j.athoracsur.2004.04.046

17. Eng CW, Fuqua JR, Grewal R, Ilson D, Messiah AC, Rizk N, et al. Evaluation of response to induction chemotherapy in esophageal cancer: is barium esophagography or PET-CT useful? *Clin Imag* (2013) 37(3):468–74. doi: 10.1016/j.clinimag.2012.08.003

18. Zhang XY, Yan WP, Sun Y, Li XT, Chen Y, Fan MY, et al. CT signs can predict treatment response and long-term survival: A study in locally advanced esophageal cancer with preoperative chemotherapy. *Ann Surg Oncol* (2015) (22 Suppl 3):S1380–7. doi: 10.1245/s10434-015-4531-2

19. Chen MF, Yang YH, Lai CH, Chen PC, Chen WC. Outcome of patients with esophageal cancer: a nationwide analysis. *Ann Surg Oncol* (2013) 20(9):3023–30. doi: 10.1245/s10434-013-2935-4

20. Lin J, Li X, Shi X, Zhang L, Liu H, Liu J, et al. Nomogram for predicting pathologic complete response after transarterial chemoembolization in patients with hepatocellular carcinoma. *Ann Transl Med* (2021) 9(14):1130. doi: 10.21037/atm-21-1120

21. Jin X, Zheng X, Chen D, Jin J, Zhu G, Deng X, et al. Prediction of response after chemoradiation for esophageal cancer using a combination of dosimetry and CT radiomics. *Eur Radiol* (2019) 29(11):6080–8. doi: 10.1007/s00330-019-06193-w

22. Murakami Y, Kawahara D, Tani S, Kubo K, Katsuta T, Imano N, et al. Predicting the local response of esophageal squamous cell carcinoma to neoadjuvant chemoradiotherapy by radiomics with a machine learning method using (18)F-FDG PET images. *Diagnostics (Basel)* (2021) 11(6):1049. doi: 10.3390/diagnostics11061049

23. Hou Z, Li S, Ren W, Liu J, Yan J, Wan S. Radiomic analysis in T2W and SPAIR T2W MRI: Predict treatment response to chemoradiotherapy in esophageal squamous cell carcinoma. *J Thorac Dis* (2018) 10(4):2256–67. doi: 10.21037/jtd.2018.03.123

24. Ypsilantis PP, Siddique M, Sohn HM, Davies A, Cook G, Goh V, et al. Predicting response to neoadjuvant chemotherapy with PET imaging using convolutional neural networks. *PloS One* (2015) 10(9):e137036. doi: 10.1371/journal.pone.0137036

25. Luo HS, Huang SF, Xu HY, Li XY, Wu SX, Wu DH. A nomogram based on pretreatment CT radiomics features for predicting complete response to chemoradiotherapy in patients with esophageal squamous cell cancer. *Radiat Oncol* (2020) 15(1):249. doi: 10.1186/s13014-020-01692-3

26. Castellano G, Bonilha L, Li LM, Cendes F. Texture analysis of medical images. *Clin Radiol* (2004) 59(12):1061–9. doi: 10.1016/j.crad.2004.07.008

27. Yip C, Davnall F, Kozarski R, Landau DB, Cook GJ, Ross P, et al. Assessment of changes in tumor heterogeneity following neoadjuvant chemotherapy in primary esophageal cancer. *Dis Esophagus* (2015) 28(2):172–9. doi: 10.1111/dote.12170

28. Yip C, Landau D, Kozarski R, Ganeshan B, Thomas R, Michaelidou A, et al. Primary esophageal cancer: Heterogeneity as potential prognostic biomarker in patients treated with definitive chemotherapy and radiation therapy. *Radiology* (2014) 270(1):141–8. doi: 10.1148/radiol.13122869

29. Nakajo M, Jinguji M, Nakabeppu Y, Nakajo M, Higashi R, Fukukura Y, et al. Texture analysis of (18)F-FDG PET/CT to predict tumour response and prognosis of patients with esophageal cancer treated by chemoradiotherapy. *Eur J Nucl Med Mol Imag* (2017) 44(2):206–14. doi: 10.1007/s00259-016-3506-2

30. Daugman JG. Complete discrete 2-d gabor transforms by neural networks for image analysis and compression. *IEEE Trans Acoustics Speech Signal Process* (1988) 36 (7):1169–79. doi: 10.1109/29.1644

31. Huo X, Liang RB, Wei JC, Xu Y, Fu JH, Luo RZ, et al. Cyclin D1 expression predicts postoperative distant metastasis and survival in resectable esophageal squamous cell carcinoma. *Oncotarget* (2016) 7(21):31088–96. doi: 10.18632/oncotarget.9078

frontiers | Frontiers in Oncology

TYPE Original Research
PUBLISHED 12 May 2023
DOI 10.3389/fonc.2023.1131883

OPEN ACCESS

EDITED BY
Bo Zhang,
Sichuan University, China

REVIEWED BY
Huan Zhang,
Shanghai Jiao Tong University, China
Zhiwei Li,
Harbin Medical University, China

*CORRESPONDENCE
Xiangnan Li
lxn-2000@163.com
Guoqing Zhang
drzhangguoqing@163.com

†These authors have contributed equally to this work and share first authorship

RECEIVED 26 December 2022
ACCEPTED 24 April 2023
PUBLISHED 12 May 2023

CITATION
Li K, Li Y, Wang Z, Huang C, Sun S, Liu X, Fan W, Zhang G and Li X (2023) Delta-radiomics based on CT predicts pathologic complete response in ESCC treated with neoadjuvant immunochemotherapy and surgery. *Front. Oncol.* 13:1131883. doi: 10.3389/fonc.2023.1131883

Delta-radiomics based on CT predicts pathologic complete response in ESCC treated with neoadjuvant immunochemotherapy and surgery

Kaiyuan Li[1†], Yuetong Li[2†], Zhulin Wang[1], Chunyao Huang[1], Shaowu Sun[1], Xu Liu[1], Wenbo Fan[1], Guoqing Zhang[1*] and Xiangnan Li[1*]

[1]Department of Thoracic Surgery, First Affiliated Hospital of Zhengzhou University, Zhengzhou, Henan, China, [2]Clinical Medical College, Henan University, Henan, Kaifeng, China

Background and purpose: Unnecessary surgery can be avoided, and more appropriate treatment plans can be developed for patients if the efficacy of neoadjuvant immunochemotherapy for esophageal cancer (EC) can be predicted before surgery. The purpose of this study was to evaluate the ability of machine learning models based on delta features of immunochemotherapy CT images to predict the efficacy of neoadjuvant immunochemotherapy in patients with esophageal squamous cell carcinoma (ESCC) compared with machine learning models based solely on postimmunochemotherapy CT images.

Materials and methods: A total of 95 patients were enrolled in our study and randomly divided into a training group (n = 66) and test group (n = 29). We extracted preimmunochemotherapy radiomics features from preimmunochemotherapy enhanced CT images in the preimmunochemotherapy group (pregroup) and postimmunochemotherapy radiomics features from postimmunochemotherapy enhanced CT images in the postimmunochemotherapy group (postgroup). We then subtracted the preimmunochemotherapy features from the postim munochemotherapy features and obtained a series of new radiomics features that were included in the delta group. The reduction and screening of radiomics features were carried out by using the Mann-Whitney U test and LASSO regression. Five pairwise machine learning models were established, the performance of which was evaluated by receiver operating characteristic (ROC) curve and decision curve analyses.

Results: The radiomics signature of the postgroup was composed of 6 radiomics features; that of the delta-group was composed of 8 radiomics features. The area under the ROC curve (AUC) of the machine learning model with the best efficacy was 0.824 (0.706-0.917) in the postgroup and 0.848 (0.765-0.917) in the delta group. The decision curve showed that our machine learning models had good

predictive performance. The delta group performed better than the postgroup for each corresponding machine learning model.

Conclusion: We established machine learning models that have good predictive efficacy and can provide certain reference values for clinical treatment decision-making. Our machine learning models based on delta imaging features performed better than those based on single time-stage postimmunochemotherapy imaging features.

KEYWORDS

esophageal cancer, delta radiomics, neoadjuvant immunochemotherapy, pathological complete response, machine learning

1 Introduction

Esophageal cancer (EC) is the most common malignant tumor of the upper digestive tract, ranking seventh in terms of incidence (604,000 new cases) and sixth in terms of overall mortality (544,000 deaths) among all cancers. The five-year relative survival rate for EC is lowest among cancers and comparable to that for liver cancer at 20% (1, 2). Most cases of EC are diagnosed at middle and advanced stages. Surgical resection after neoadjuvant chemoradiotherapy (NCRT) should be considered the standard of care for patients with resectable locally advanced EC. In patients with locally advanced ESCC, NCRT plus surgery improves survival compared with surgery alone, and the adverse events are acceptable and controllable. In patients with resectable EC, the combination of neoadjuvant chemoradiotherapy and surgery has an overall survival benefit (3, 4). Studies have reported a probability of pathologic complete response after neoadjuvant immunochemotherapy for EC of 26% to 49% (5–7). After many explorations in recent years, immunotherapy for EC has been expanded to neoadjuvant therapy and immunotherapy combined with neoadjuvant chemotherapy. There is much clinical experience accumulated to date. For example, the NICE-2, TD-NICE and Keep-G 03 studies, among others, have shown relatively ideal disease control rates and PCR rates (8–10). Therefore, it is very important to accurately predict the efficacy of neoadjuvant immunochemotherapy for EC. Radiomics is an emerging technology with the ability to capture intratumor heterogeneity in a noninvasive manner. Indeed, radiomics is a promising approach to comprehensively quantify tumor phenotypes through application of a large number of quantitative imaging features (11, 12).

Delta-radiomics is the change in radiomics features, a multitemporal comparison, and can fully reflect characteristic changes in tumors before and after treatment. Previously published studies have demonstrated the superiority of delta-radiomics in cancer from many aspects. The study of Jing Gong et al. showed that a delta-radiomics model can improve predictive performance and has prognostic value in predicting the progression-free survival and overall survival of non-small cell lung cancer (NSCLC) patients (13). According to Zhang, Z. et al., the delta-radiomics features extracted from MR images after surgical radiotherapy for brain metastases have the potential to distinguish radiation necrosis from tumor progression and have better predictive value than traditional radiomics features (14). The purpose of this study was to evaluate the ability of machine learning models based on delta features of immunochemotherapy CT images to predict the efficacy of neoadjuvant immunochemotherapy in patients with esophageal squamous cell carcinoma (ESCC) compared with machine learning models based solely on postimmunochemotherapy CT images.

2 Materials and methods

2.1 Study design

After patient selection, we manually outlined the region of interest (ROI) on the CT images of patients before and after neoadjuvant immunochemotherapy. Then, we extracted the radiomics features according to the radiomics classes and filters shown in Figure 1 for statistical analysis. The flowchart of the main steps is illustrated in Figure 1.

2.2 Patients

A total of 146 patients with EC who received neoadjuvant immunochemotherapy plus surgical resection at the First Affiliated Hospital of Zhengzhou University from June 2019 to May 2022 were included in this study. The inclusion criteria were (i) ESCC diagnosed by histopathology and (ii) complete available enhanced CT images before and after immunochemotherapy. The exclusion criteria were as follows: (i) adenocarcinoma of the esophagogastric junction (n=6); (ii) esophageal fistula after neoadjuvant immunochemotherapy (n=1); (iii) incomplete diagnosis and treatment process in our hospital (n=20); and (iv) nonenhanced CT or CT image artifacts (n=24). Ultimately, 95 patients were enrolled in this study.

10.3389/fonc.2023.1131883

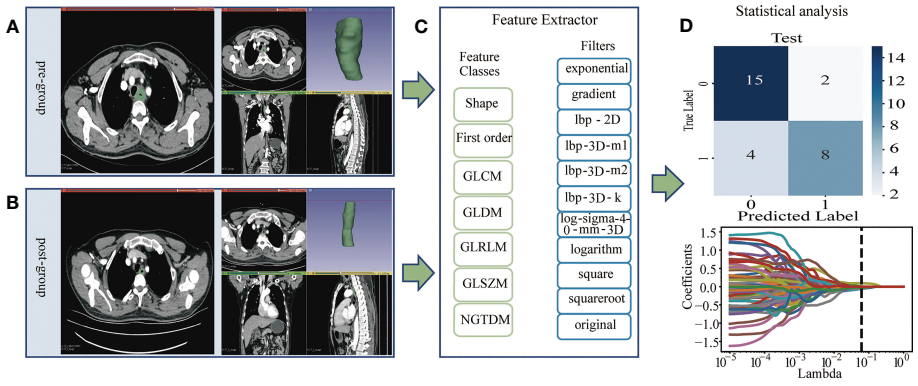

FIGURE 1
(A, B): Image Acquisition & Tumor Segmentation. **(A)** The region of interest (ROI) of the pregroup. **(B)** The region of interest (ROI) of the postgroup. **(C)** The PyRadiomics package was used to extract radiomics features, and the radiomics classes and filters used are listed. The pregroup features and postgroup features were extracted, and the delta features were obtained. Delta features = postgroup features - pregroup features. **(D)** The least absolute shrinkage and selection operator (LASSO) algorithm was applied to select features, and other statistical analyses were performed, such as predictive model construction and validation.

2.3 CT image acquisition and tumor segmentation

Enhanced CT images before and after neoadjuvant immunochemotherapy were obtained for all patients. CT scanners from multiple manufacturers were used for enhanced chest CT of all patients. Information about the scan parameters of CT (including manufacturer, tube voltage, tube current, etc.) is provided in Supplemental Material Table S2. The tumor ROI was manually delineated on 3Dslicer (version 4.1.1, http://www.slicer.org, USA) by two thoracic surgeons with more than 5 years of clinical experience; the ROI was delineated and analyzed in the arterial phase. First, the tumor contour was delineated on enhanced CT images before neoadjuvant immunochemotherapy by referring to gastroscopy, barium meal gastrointestinal examination and other examinations. Then, the head and tail lengths of the delineated ROI on the enhanced CT images before and after neoadjuvant immunochemotherapy were determined. The length was kept unchanged, and the tumor ROI after neoadjuvant immunochemotherapy continued to be delineated manually. CT images of the same patient before and after neoadjuvant immunochemotherapy ensured that the tumor was of the same length in the sagittal position. The preneoadjuvant target area served as a reference for the postneoadjuvant target area; that is, the target area was the same. The mapped tumor area was evaluated by another radiologist.

2.4 Radiomics feature extraction and selection

The PyRadiomics (version 3.0.1, http://github.com/Radiomics/pyradiomics#readme) package of Python software (version 3.9.7) was used to extract features from the postgroup and delta group. Delta radiomics features were defined as the radiomics features of the postgroup minus the radiomics features of the pregroup. The extracted radiomics features were screened by the Mann-Whitney U test, and features with a threshold of $P < 0.05$ were retained, after which data standardization (StandardScaler) was selected to nondimensionalize these retained radiomics features. Next, five cross-validations and iterations of 1e6 were performed on the standardized features to obtain the alpha parameter with the minimum mean square error. Based on the selected optimal alpha parameter, the least absolute contraction and selection operator (LASSO) feature selection algorithm was applied to select relevant features and calculate the coefficients of each. LASSO solves the multicollinearity problem by resetting insignificant feature weights to zero through penalty coefficients, thus reducing the feature dimension. Finally, radiomics features with nonzero coefficients were obtained. To increase the repeatability of radiomics features and the generalization and stability of the models, 10 patients in the pregroup and the postgroup were randomly selected, and the ROIs outlined by Reader1 and Reader2 were used for reliability analysis (ICC). Detailed information is available in Supplementary Materials Table S3 and Table S4.

2.5 Statistical analysis

We randomly divided patients into a training set and a test set (7:3); the former was used to develop the machine learning models and the latter to verify and evaluate the performance of the machine learning models. The predictive radiomics features selected by the Mann-Whitney U test and LASSO algorithm were entered into machine learning models. We built the machine learning models using the scikit-learn package (version 1.0.2, http://scikit-learn.org) in Python (version 3.9.7). Five machine learning models were constructed with both the postgroup and delta group, including support vector machine (SVM), regression decision tree (DT), random forest (RF), extreme gradient boosting (XGBoost), and logistic regression (LR). We also evaluated the predictive power of each machine learning classifier using a validation set, and the AUC value and the corresponding sensitivity, specificity, and overall accuracy were calculated. Decision curves of the machine learning

models with the best AUC performance were plotted for guiding clinical decisions.

3 Results

3.1 Patients

A total of 95 patients were enrolled in our study. Postoperative histopathologic specimens were evaluated by an experienced pathologist and reviewed by a thoracic surgeon. Pathological complete response (PCR) occurred in 39 patients and nonpathological complete response (nPCR) in 56 patients, with a ratio of approximately 2:3. Table 1 provided the patient details. The immunochemotherapy regimen was paclitaxel and platinum combined with PD-1 monoclonal antibody. Ninety-four patients underwent esophagectomy by the McKeown method, and 1 patient underwent esophagectomy by the Ivor-Lewis method.

3.2 Feature selection of radiomics

A total of 1,037 features were extracted from the postgroup and the delta group. The extracted radiomics features were screened by the Mann-Whitney U test, and those with a threshold of $P < 0.05$ were retained. In total, 335 features for the postgroup were retained and 154 for the delta group. Then, the least absolute shrinkage and selection operator (LASSO) algorithm was applied to select features. Details are provided in Table S1 in the Supplementary Material. Among them, 6 nonzero features were retained for the postgroup and 8 for the delta group, and their corresponding coefficients were determined. For the postgroup, the results were as follows: coefficient of feature A 'original_shape_Maximum2DDiameterSlice' -0.01413; of feature B 'lbp-2D_gldm_DependenceNonUniformityNormalized' -0.00953215; of feature C 'lbp-3D-m2_firstorder_Kurtosis' -0.0263521; of feature D 'lbp-3D-m2_gldm_DependenceNonUniformityNormalized' -0.00134778; of feature E 'lbp-3D-k_glszm_SmallAreaLowGrayLevelEmphasis' -0.05375544; and of feature F'square_glrlm_RunEntropy' -0.09855901. The results for the postgroup the delta group were as follows: coefficient of feature A 'original_shape_Elongation' -0.04356936; of feature B 'original_shape_MinorAxisLength' -0.1491607; feature C 'original_shape_SurfaceVolumeRatio' 0.09608021; of feature D 'lbp-3D-m2_firstorder_Kurtosis' -0.05886248; of feature E 'lbp-3D-k_glszm_SmallAreaHighGrayLevelEmphasis' -0.06292696; of feature F 'lbp-3D-k_ngtdm_Coarseness' 0.0091555; of feature G 'log-sigma-4-0-mm-3D_glcm_Autocorrelation' -0.05041306; and of feature H'square_glrlm_RunEntropy' of -0.02573776. These results are shown in Figure 2.

3.3 Diagnostic performance of radiomics models

The nonzero features of the two groups retained were modeled separately by machine learning, and all models showed good predictive efficacy of neoadjuvant immunochemotherapy in the validation set. The results for all models are given in Table 2.

Table 3 lists the specific parameters of each model. In the process of model fitting, we use grid searches, learning curves and other methods to obtain optimal parameters. The random forest classifier had the best effect in both groups. The AUC value of the validation set of the postgroup was 0.82 (95% CI, 0.706-0.917); the sensitivity was 0.83, the specificity 0.76, and the accuracy 0.79. The AUC value of the delta group was 0.85 (95% CI, 0.765-0.917), the sensitivity was 0.67, the specificity was 0.88, and the accuracy was 0.79. Figures 3, 4 depict all the ROC curves of the models. In this study, we plotted decision curves of the best-performing random forest classifiers to guide clinical decision-making, as indicated in Figure 5. Decision curve analysis (DCA) is a widely used method to measure clinical practicability. Figure 5 shows the net benefit of two random forest models in determining the efficacy of immunochemotherapy for ESCC. The net benefit was defined as the harm from a residual tumor by avoiding surgical resection of the esophagus (false positive) subtracted from the benefit from avoiding surgical resection of the esophagus (true positive) in patients predicted by the model to have PCR. It can be seen from the decision curve that the random forest model of the delta group indicated more net benefit than the random forest model of the postgroup.

4 Discussion

The purpose of this study was to evaluate the difference in the prediction of neoadjuvant immunochemotherapy for ESCC between postimmunohistotherapy CT modeling alone and delta imaging modeling. We used the variation in image group characteristics before and after immunochemotherapy (delta group) and the image of the individual postgroup to build 5 kinds of machine learning models, which were verified in the test set. Each machine learning model showed good predictive ability with regard to the effect of a neoadjuvant immunochemotherapy curative effect, and the prediction effect was best in the random forest models. Indeed, the two random forest models achieved high AUC values of 0.82 (postgroup) and 0.85 (delta-group) in the verification set. The predictive effect of the model established by delta radiomics was better than that of single imaging feature modeling after immunochemotherapy. The AUC value was similar to that reported by Hu, Y., et al. (15) Moreover, the results were verified by DCA, demonstrating good clinical practicability of the models.

Traditional imaging examination can show the size, morphology, enhancement mode and other characteristics of lesions but cannot reveal more in-depth information about EC. As an emerging technology to capture high-throughput imaging features, radiomics can capture the heterogeneity of tumors in a noninvasive way with great objectivity. Many previous studies have demonstrated the utility of radiomics in predicting response to neoadjuvant chemoradiotherapy at different levels. Most of these studies used FDG PET/CT to predict PCR with neoadjuvant chemotherapy and radiotherapy (NCRT) in patients with locally advanced EC (16–18). In addition, most previous studies modeled radiomics features based on a single time phase. In the study of Qiu Q et al., CT images of patients before nCRT were collected, 711

TABLE 1 Demographic statistics of patients in the training cohort and test cohort.

Variable	Training cohort (n=66)	Test cohort(n=29)		
			χ2/Z	P
Sex			0.4107	0.5216
Female	25	9		
Male	41	20		
Age			-0.931	0.352
Mean	65.3	64.1		
Median	66	64		
Range	49~77	54~75		
SD	6.39	6.12		
Smoking history			0.028	0.8671
Yes	17	7		
No	49	22		
Alcohol history			2.0285	0.1544
Yes	10	8		
No	56	21		
BMI			0.3177	0.573
≥ 18.5 and <24	36	14		
≥ 24	30	15		
Clinical T stage			0.325	0.9553
T1	17	7		
T2	14	5		
T3	26	13		
T4	9	4		
Clinical N stage			5.9933	0.05
N0	46	13		
N1	14	13		
N2	6	3		
Tumor location			2.7979	0.2469
Upper thoracic	10	1		
Middle thoracic	32	17		
Lower thoracic	24	11		
Pathological Differentiation			2.9638	0.3972
Low	7	7		
Middle	31	12		
High	3	1		
unknown	25	9		

radiomics features were extracted, and radiomics nomograms were constructed. The optimal value of the C index was 0.746 (95% CI, 0.680 – 0.812) in the training cohort and 0.724 (95% CI, 0.696 – 0.752) in the validation cohort (19). Mao, Y. et al. also extracted a total of 340 radiological features from CT images of patients with locally advanced rectal cancer (LARC) prior to neoadjuvant chemotherapy. The best performing model used both radiomics and clinical variables, with areas under the curve of 0.926 and 0.872,

10.3389/fonc.2023.1131883

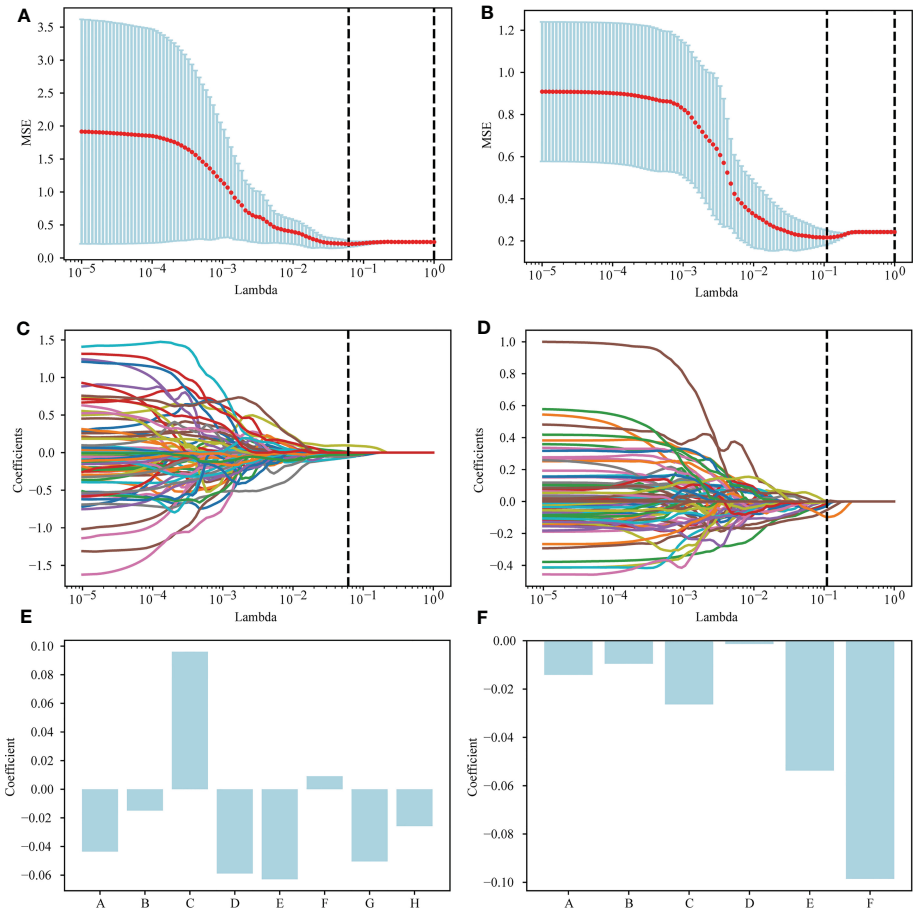

FIGURE 2
Selection of radiomics features *via* the LASSO method. **(A)** A 5-fold cross-validation curve for the radiomics features of the delta group, with vertical dashed lines drawn at the point where the optimal lambda value is 0.0613591 and the number of radiomics features is 8. **(B)** A 5-fold cross-validation curve for the radiomics features of the postgroup was drawn with vertical dashed lines at the optimal lambda value of 0.1097498 and the number of radiomic features of 6. **(C)** LASSO coefficient profiles of the 154 features retained for the delta group. The coefficient profile is drawn for the lambda sequence. Vertical lines are drawn at values selected using 5-fold cross-validation, where the optimum lambda yields 8 features with nonzero coefficients. **(D)** LASSO coefficient profiles of the 335 features retained for the postgroup. The coefficient profile is drawn for the lambda sequence. Vertical lines are drawn at values selected using 5-fold cross-validation, where the best lambda yields 6 features with nonzero coefficients. **(E, F)** The nonzero coefficients screened by post group and their corresponding coefficients.

respectively, in the training and validation cohorts (20). Similarly, Yang Z et al. extracted radiomic features from CT images before neoadjuvant therapy and constructed three models. The AUC values of the model with the best performance in the training set and the test set were 0.85 and 0.79, respectively (21). However, studies based on a single phase did not contain information about response to treatment. Delta radiomics covers a large amount of time-dependent information, allows dynamic assessment of complete tumor changes over the treatment period, provides a large amount of data on treatment-induced changes and is more consistent with assessment of immunotherapy effects in clinical practice. Thus far, few previous studies have used delta imaging

TABLE 2 The results of all models.

Models	post						delta					
	SEN	SPE	PPV	NPV	ACC	AUC	SEN	SPE	PPV	NPV	ACC	AUC
SVM	0.58	0.71	0.58	0.71	0.66	0.686(0.667-0.706)	0.58	0.88	0.78	0.75	0.76	0.770(0.667-0.882)
DT	0.58	0.76	0.64	0.72	0.69	0.711(0.706-0.750)	0.67	0.82	0.73	0.78	0.76	0.745(0.667-0.824)
RF	0.83	0.76	0.71	0.87	0.79	0.824(0.706-0.917)	0.67	0.88	0.8	0.79	0.79	0.848(0.765-0.917)
XGBoost	0.33	0.82	0.57	0.64	0.62	0.760(0.647-0.833)	0.58	0.88	0.78	0.75	0.76	0.789(0.647-0.833)
LR	0.58	0.71	0.58	0.71	0.66	0.676(0.647-0.750)	0.67	0.71	0.62	0.75	0.69	0.799(0.667-0.824)

TABLE 3 Parameters of all machine learning models in this study.

groups	Model	parameters
delta	SVM	C = 25, gamma = 0.09, kernel = "poly", probability = True
	DT	criterion = 'entropy', random_state = 23, max_depth = 1, min_samples_leaf = 1, min_samples_split = 5
	RF	random_state = 11, n_estimators = 3, criterion = "gini", max_depth = 2, max_features = "sqrt", min_samples_leaf = 1, min_samples_split = 5
	XGBoost	random_state = 10, booster = 'gbtree',learning_rate=0.23,colsample_bylevel=0.8,gamma =0,max_depth=3,min_child_weight=3,n_estimators = 3, objective='binary:logistic',use_label_encoder=False
	LR	penalty="l1", solver="liblinear",C = 0.1125,class_weight="balanced"
post	SVM	C = 0.0625, gamma = 0.01, kernel = "linear", probability = True
	DT	criterion = 'entropy', random_state = 21, max_depth = 6, min_samples_leaf = 2, min_samples_split = 7
	RF	random_state = 26, n_estimators = 2, criterion = "gini", max_depth = 2, max_features = "auto", min_samples_leaf = 1, min_samples_split = 5
	XGBoost	random_state = 10, booster = 'gbtree',learning_rate=0.55,colsample_bytree = 0.1, colsample_bylevel=0.6,gamma =0,max_depth=3, min_child_weight=3,n_estimators = 5, objective='binary:logistic',use_label_encoder=False
	LR	penalty="l1", solver="liblinear",C = 0.3,class_weight="balanced",tol=0.0001, multi_class='ovr'

features to model and predict the efficacy of neoadjuvant chemotherapy for EC. Xie CY et al. used a delta radiomics approach combined with a genomics approach that utilized differentially expressed genes to reduce the number of radiomics features, allowing the creation of a CT-based radiomics model using a genomic-based feature selection approach. This resulted in better performance and versatility (AUC: 0.912 in the training set, 0.825 in the internal test set, and 0.749 in the external test set) (22). In recent years, the unique value of delta radiomics has been demonstrated in many areas of cancer and shown to improve the performance of predictive models in many ways (23–28). This is the same as the conclusion obtained in this study, which is encouraging. In this study, comparison between radiomics models was conducted based on CT images for the same patients, and the results showed that delta radiomic features were superior to single time-phase image omics features, which may provide certain reference value for similar radiomics modeling in the future.

This study built a decision curve based on the best machine learning model, with potential clinical application for some problems based on machine learning model and decision curve analyses. EC patients have a high incidence of surgical complications, significantly reduced postoperative quality of life and risk of death, which is not a good choice for patients who achieve PCR after neoadjuvant chemotherapy (29–32). The results of this study can be used as a potential auxiliary method independent to evaluate surgical specimens to identify complete responders who may avoid surgery and as an important reference factor to evaluate whether patients can undergo neoadjuvant chemotherapy as an alternative therapy to surgery. This approach provides significant clinical benefit for identifying patients eligible for individualized organ preservation therapy programs (33).

There are some limitations in this study. The main limitation is that the sample size was small. The main reason for this is that complete patient information was involved, complete and

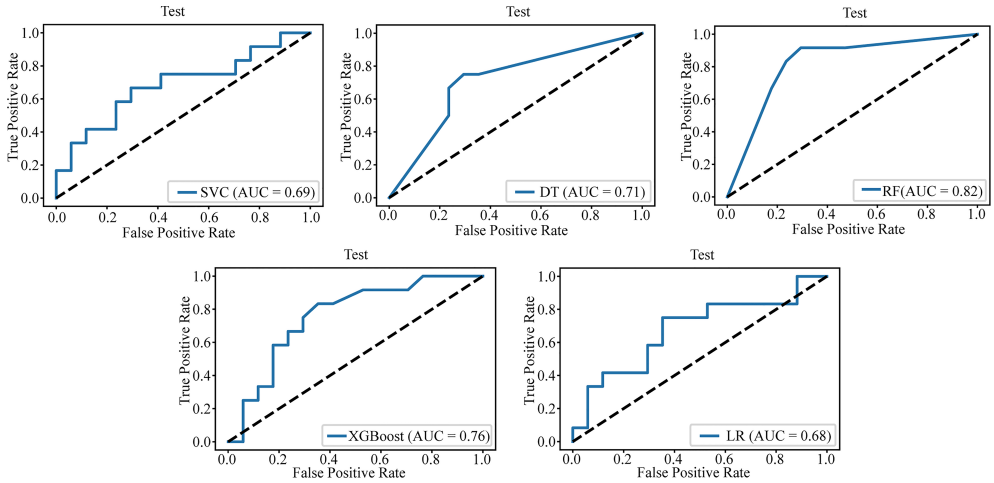

FIGURE 3
The AUC value for the post group test set.

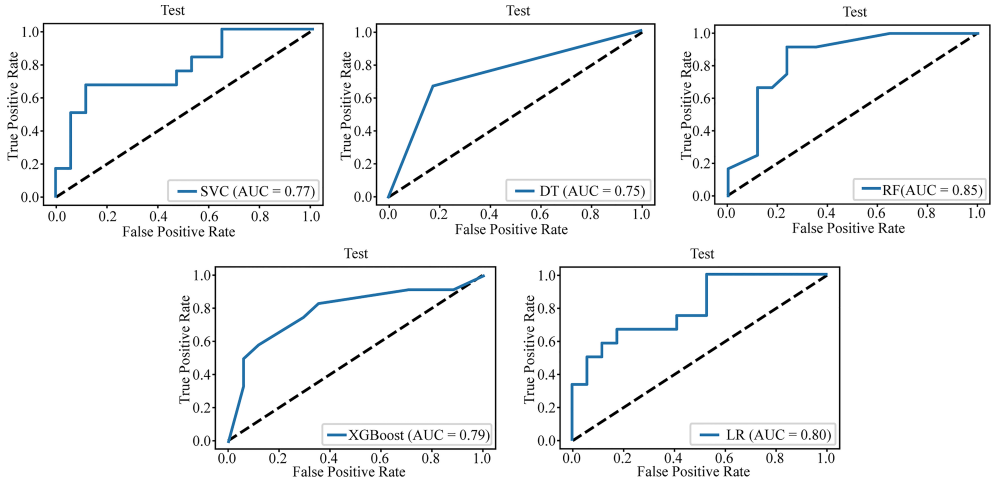

FIGURE 4
The AUC value for the delta group test set.

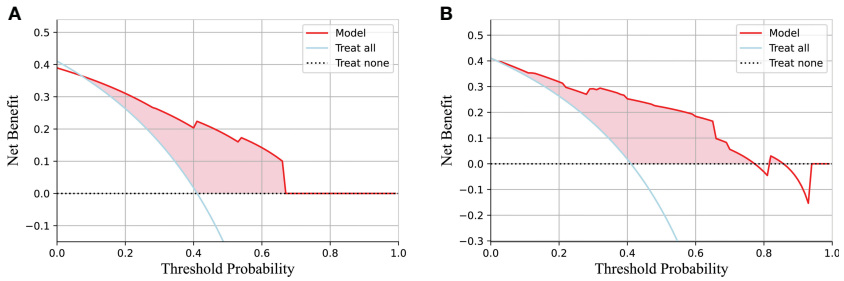

FIGURE 5
The decision curve of the random forest model based on the test group and two extreme curves are drawn. The decision curve depicts the net benefit of the model within a certain probability threshold (Y-axis). The treat-all curve indicates that the intervention was performed regardless of the predicted outcome; thus, esophagectomy was avoided in this study. The treat-none curve indicates that no intervention was performed regardless of the outcome; thus, esophagectomy was performed in this study. The part of the model that is better than the two extreme curves is indicated by the pink fill. **(A)** The decision curve for the postgroup. **(B)** The decision curve for the delta group.

available enhanced CT images before and after neoadjuvant chemotherapy had to be available, and postoperative pathological confirmation and accuracy of follow-up information had to be completed. In addition, to ensure the learning effect of machine learning, we conducted data balancing (PCR: none-PCR = 1:1), as the aforementioned findings suggested that the probability of pathologic complete response after neoadjuvant chemotherapy for esophageal cancer is 26% to 49% (5–7). Therefore, the clinical PCR rate also limited the sample size. This may have resulted in a model that was weak in generalizability and does not represent the characteristics of all populations. Second, more medical centers were needed, and it would be worthwhile to conduct research involving more centers. Multicenter research may be helpful to improve and externally verify our machine learning model, increase its ability to assist in therapy, and increase its ability to contribute to clinical decision-making and effective prediction.

5 Conclusion

We used CT to extract radiomics features to establish a sample machine learning model for effectively predicting PCR after neoadjuvant immunochemotherapy. The machine learning model we established has a good predictive effect and can provide some value for clinical treatment decision-making. Overall, our machine learning model based on delta imaging features performed better than the model based on single time-phase postimmunochemotherapy imaging features.

Data availability statement

The original contributions presented in the study are not publicly available, but are available from the corresponding author on reasonable request.

Ethics statement

Written informed consent was obtained from the individual(s) for the publication of any potentially identifiable images or data included in this article.

Author contributions

KL and YL designed the experiments, performed the study, completed the data analysis and wrote the first draft of the paper. CH, ZW, SS, XuL, and WF participated in the experimental design and analysis of the experimental results. GZ and XiL conceived of the idea for the project and is the author and person in charge guided the experimental design, data analysis, and manuscript writing and revision. All authors contributed to the article and approved the submitted version.

Funding

This work was supported by the National Natural Science Foundation of China (32070623) and the First Affiliated Hospital of Zhengzhou University.

Conflict of interest

The authors declare that the research was conducted in the absence of any commercial or financial relationships that could be construed as a potential conflict of interest.

Publisher's note

Supplementary material

The Supplementary Material for this article can be found online at: https://www.frontiersin.org/articles/10.3389/fonc.2023.1131883/full#supplementary-material

References

1. Siegel RL, Miller KD, Fuchs HE, Jemal A. Cancer statistics, 2022. *CA Cancer J Clin* (2022) 72(1):7–33. doi: 10.3322/caac.21708

2. Sung H, Ferlay J, Siegel RL, Laversanne M, Soerjomataram I, Jemal A, et al. Global cancer statistics 2020: GLOBOCAN estimates of incidence and mortality worldwide for 36 cancers in 185 countries. *CA Cancer J Clin* (2021) 71(3):209–49. doi: 10.3322/caac.21660

3. Shapiro J, van Lanschot JJB, Hulshof MCCM, van Hagen P, van Henegouwen Berge MI, Wijnhoven BPL, et al. Neoadjuvant chemoradiotherapy plus surgery versus surgery alone for oesophageal or junctional cancer (CROSS): long-term results of a randomised controlled trial. *Lancet Oncol* (2015) 16(9):1090–8. doi: 10.1016/S1470-2045(15)00040-6

4. Yang H, Liu H, Chen Y, Zhu C, Fang W, Yu Z, et al. Neoadjuvant chemoradiotherapy followed by surgery versus surgery alone for locally advanced squamous cell carcinoma of the esophagus (NEOCRTEC5010): a phase III multicenter, randomized, open-label clinical trial. *J Clin Oncol* (2018) 36(27):2796–803. doi: 10.1200/JCO.2018.79.1483

5. van Hagen P, Hulshof MC, van Lanschot JJ, Steyerberg EW, van Henegouwen Berge MI, Wijnhoven BP, et al. Preoperative chemoradiotherapy for esophageal or junctional cancer. *N Engl J Med* (2012) 366(22):2074–84. doi: 10.1056/NEJMoa1112088

6. Mariette C, Dahan L, Mornex F, Maillard E, Thomas PA, Meunier B, et al. Surgery alone versus chemoradiotherapy followed by surgery for stage I and II esophageal cancer: final analysis of randomized controlled phase III trial FFCD 9901. *J Clin Oncol* (2014) 32(23):2416–22. doi: 10.1200/JCO.2013.53.6532

7. Donahue JM, Nichols FC, Li Z, Schomas DA, Allen MS, Cassivi SD, et al. Complete pathologic response after neoadjuvant chemoradiotherapy for esophageal cancer is associated with enhanced survival. *Ann Thorac Surg* (2009) 87(2):392–8. doi: 10.1016/j.athoracsur.2008.11.001

8. Yan X, Duan H, Ni Y, Zhou Y, Wang X, Qi H, et al. Tislelizumab combined with chemotherapy as neoadjuvant therapy for surgically resectable esophageal cancer: a prospective, single-arm, phase II study (TD-NICE). *Int J Surg* (2022) 103:106680. doi: 10.1016/j.ijsu.2022.106680

9. Chen X, Xu X, Wang D, Liu J, Sun J, Lu M, et al. Neoadjuvant sintilimab and chemotherapy in patients with potentially resectable esophageal squamous cell carcinoma (KEEP-G 03): an open-label, single-arm, phase 2 trial. *J ImmunoTher Cancer* (2023) 11(2):e005830. doi: 10.1136/jitc-2022-005830

10. Yang Y, Zhu L, Cheng Y, Liu Z, Cai X, Shao J, et al. Three-arm phase II trial comparing camrelizumab plus chemotherapy versus camrelizumab plus chemoradiation versus chemoradiation as preoperative treatment for locally advanced esophageal squamous cell carcinoma (NICE-2 study). *BMC Cancer* (2022) 22(1):506. doi: 10.1186/s12885-022-09573-6

11. Aerts HJ, Velazquez ER, Leijenaar RT, Parmar C, Grossmann P, Carvalho S, et al. Decoding tumour phenotype by noninvasive imaging using a quantitative radiomics approach. *Nat Commun* (2014) 5:4006. doi: 10.1038/ncomms5006

12. Lambin P, Rios-Velazquez E, Leijenaar R, Carvalho S, van Stiphout RG, Granton P, et al. Radiomics: extracting more information from medical images using advanced feature analysis. *Eur J Cancer* (2012) 48(4):441–6. doi: 10.1016/j.ejca.2011.11.036

13. Gong J, Bao X, Wang T, Liu J, Peng W, Shi J, et al. A short-term follow-up CT based radiomics approach to predict response to immunotherapy in advanced non-small-cell lung cancer. *Oncoimmunology* (2022) 11(1):2028962. doi: 10.1080/2162402X.2022.2028962

14. Zhang Z, Yang J, Ho A, Jiang W, Logan J, Wang X, et al. A predictive model for distinguishing radiation necrosis from tumour progression after gamma knife radiosurgery based on radiomic features from MR images. *Eur Radiol* (2018) 28(6):2255–63. doi: 10.1007/s00330-017-5154-8

15. Hu Y, Xie C, Yang H, Ho JWK, Wen J, Han L, et al. Computed tomography-based deep-learning prediction of neoadjuvant chemoradiotherapy treatment response in esophageal squamous cell carcinoma. *Radiother Oncol* (2021) 154:6–13. doi: 10.1016/j.radonc.2020.09.014

16. Beukinga RJ, Hulshoff JB, Mul VEM, Noordzij W, Kats-Ugurlu G, Slart R, et al. Prediction of response to neoadjuvant chemotherapy and radiation therapy with baseline and restaging (18)F-FDG PET imaging biomarkers in patients with esophageal cancer. *Radiology* (2018) 287(3):983–92. doi: 10.1148/radiol.2018172229

17. Beukinga RJ, Hulshoff JB, van Dijk LV, Muijs CT, Burgerhof JGM, Kats-Ugurlu G, et al. Predicting response to neoadjuvant chemoradiotherapy in esophageal cancer with textural features derived from pretreatment (18)F-FDG PET/CT imaging. *J Nucl Med* (2017) 58(5):723–9. doi: 10.2967/jnumed.116.180299

18. Murakami Y, Kawahara D, Tani S, Kubo K, Katsuta T, Imano N, et al. Predicting the local response of esophageal squamous cell carcinoma to neoadjuvant chemoradiotherapy by radiomics with a machine learning method using (18)F-FDG PET images. *Diagn (Basel)* (2021) 11(6):1049. doi: 10.3390/diagnostics11061049

19. Qiu Q, Duan J, Deng H, Han Z, Gu J, Yue NJ, et al. Development and validation of a radiomics nomogram model for predicting postoperative recurrence in patients with esophageal squamous cell cancer who achieved pCR after neoadjuvant chemoradiotherapy followed by surgery. *Front Oncol* (2020) 10:1398. doi: 10.3389/fonc.2020.01398

20. Mao Y, Pei Q, Fu Y, Liu H, Chen C, Li H, et al. Pre-treatment computed tomography radiomics for predicting the response to neoadjuvant chemoradiation in locally advanced rectal cancer: a retrospective study. *Front Oncol* (2022) 12:850774. doi: 10.3389/fonc.2022.850774

21. Yang Z, He B, Zhuang X, Gao X, Wang D, Li M, et al. CT-based radiomic signatures for prediction of pathologic complete response in esophageal squamous cell carcinoma after neoadjuvant chemoradiotherapy. *J Radiat Res* (2019) 60(4):538–45. doi: 10.1093/jrr/rrz027

22. Xie CY, Hu YH, Ho JW, Han LJ, Yang H, Wen J, et al. Using genomics feature selection method in radiomics pipeline improves prognostication performance in locally advanced esophageal squamous cell carcinoma-a pilot study. *Cancers (Basel)* (2021) 13(9):2145. doi: 10.3390/cancers13092145

23. Fave X, Zhang L, Yang J, Mackin D, Balter P, Gomez D, et al. Delta-radiomics features for the prediction of patient outcomes in non-small cell lung cancer. *Sci Rep* (2017) 7(1):588. doi: 10.1038/s41598-017-00665-z

24. Lin P, Yang PF, Chen S, Shao YY, Xu L, Wu Y, et al. A delta-radiomics model for preoperative evaluation of neoadjuvant chemotherapy response in high-grade osteosarcoma. *Cancer Imaging* (2020) 20(1):7. doi: 10.1186/s40644-019-0283-8

25. Mokrane FZ, Lu L, Vavasseur A, Otal P, Peron JM, Luk L, et al. Radiomics machine-learning signature for diagnosis of hepatocellular carcinoma in cirrhotic patients with indeterminate liver nodules. *Eur Radiol* (2020) 30(1):558–70. doi: 10.1007/s00330-019-06347-w

26. Nasief H, Hall W, Zheng C, Tsai S, Wang L, Erickson B, et al. Improving treatment response prediction for chemoradiation therapy of pancreatic cancer using a combination of delta-radiomics and the clinical biomarker CA19-9. *Front Oncol* (2019) 9:1464. doi: 10.3389/fonc.2019.01464

27. Rao SX, Lambregts DM, Schnerr RS, Beckers RC, Maas M, Albarello F, et al. CT texture analysis in colorectal liver metastases: a better way than size and volume measurements to assess response to chemotherapy? *United Eur Gastroenterol J* (2016) 4 (2):257–63. doi: 10.1177/2050640615601603

28. Liu Y, Wu M, Zhang Y, Luo Y, He S, Wang Y, et al. Imaging biomarkers to predict and evaluate the effectiveness of immunotherapy in advanced non-Small-Cell lung cancer. *Front Oncol* (2021) 11:657615. doi: 10.3389/fonc.2021.657615

29. Bedenne L, Michel P, Bouche O, Milan C, Mariette C, Conroy T, et al. Chemoradiation followed by surgery compared with chemoradiation alone in squamous cancer of the esophagus: FFCD 9102. *J Clin Oncol* (2007) 25(10):1160–8. doi: 10.1200/JCO.2005.04.7118

30. Goense L, Meziani J, Ruurda JP, van Hillegersberg R. Impact of postoperative complications on outcomes after oesophagectomy for cancer. *Br J Surg* (2019) 106 (1):111–9. doi: 101002/bjs11000

31. Noordman BJ, Wijnhoven BPL, Lagarde SM, Boonstra JJ, Coene P, Dekker JWT, et al. Neoadjuvant chemoradiotherapy plus surgery versus active surveillance for oesophageal cancer: a stepped-wedge cluster randomised trial. *BMC Cancer* (2018) 18(1):142. doi: 10.1186/s12885-018-4034-1

32. van der Werf LR, Busweiler LAD, van Sandick JW, van Henegouwen Berge MI, Wijnhoven B. P. L., G.I.C.A.g. Dutch Upper. Reporting national outcomes after esophagectomy and gastrectomy according to the esophageal complications consensus group (ECCG). *Ann Surg* (2020) 271(6):1095–101. doi: 10.1097/SLA.0000000000003210

33. Li Y, Liu J, Li HX, Cai XW, Li ZG, Ye XD, et al. Radiomics signature facilitates organ-saving strategy in patients with esophageal squamous cell cancer receiving neoadjuvant chemoradiotherapy. *Front Oncol* (2020) 10:615167. doi: 10.3389/fonc.2020.615167

Frontiers in Oncology

Advances knowledge of carcinogenesis and tumor progression for better treatment and management

The third most-cited oncology journal, which highlights research in carcinogenesis and tumor progression, bridging the gap between basic research and applications to imrpove diagnosis, therapeutics and management strategies.

Discover the latest Research Topics

See more →

Frontiers

Avenue du Tribunal-Fédéral 34
1005 Lausanne, Switzerland
frontiersin.org

Contact us

+41 (0)21 510 17 00
frontiersin.org/about/contact